

Performance Evaluation of iPVC Pipe under Earthquake-Induced Ground Deformation

by

D. Price

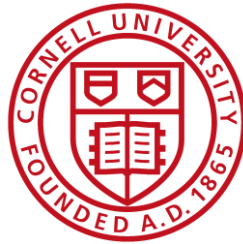
B. Berger

T. D. O'Rourke

H. E. Stewart

B. P. Wham

C. Pariya-Ekkasut



Cornell University

School of Civil and Environmental Engineering

Cornell University

Hollister Hall

Ithaca, NY 14853

December, 2018

Acknowledgements

The authors wish to recognize the excellent effort of Cornell graduate and undergraduate students who made these experiments successful. In particular, the contributions of Mia Stewart, Sarah Weinberg, Corbin Atkins, Quinton Hubbell, George Howell III, Andrew Greubel, Daniel Kusky, and Dara Karac are acknowledged.

Table of Contents

Acknowledgements	i
Table of Contents	ii
List of Figures	iv
List of Tables	vi
Section 1 Introduction	1
1.1. Pipe Specimen and Joint Restraints	1
1.2. Report Organization	2
Section 2 Material Characterization	4
2.1. Introduction	4
2.2. Tensile Coupon Testing and Procedure	4
2.3. Stress vs. Strain Data	5
Section 3 Axial Tension Tests	8
3.1. Introduction	8
3.2. Instrumentation	8
3.3. Test Sequence	10
3.4. Experimental Results	11
3.4.1. TT1 Results	11
3.4.2. TT2 Results	15
3.5. Tension Test Comparison	17
3.6. Tension Test Summary	19
Section 4 Axial Compression Test	20
4.1. Introduction	20
4.2. Instrumentation	20
4.3. Test Sequence	22
4.4. Experimental Results	22
4.4.1. CT1 Results	22
4.4.2. CT2 Results	24
4.4.3. CT3 Results	26
4.5. Compression Test Comparison	30
4.6. Compression Test Summary	30
Section 5 Four-Point Bending Test	32
5.1. Introduction	32
5.2. Setup and Instrumentation	32
5.3. Test Sequence	34
5.4. Experimental Results	36
5.4.1. Applied Vertical Displacement and Actuator Load	36
5.4.2. Bending Test Strains	37

5.4.3.	Restrained Joint Moment-Rotation	38
5.4.4.	Specimen Deflection	40
5.5.	Four-Point Bending Test Summary	41
Section 6	Axial Pull Tests	44
6.1.	Introduction	44
6.2.	Test Layout and Instrumentation	44
6.3.	Soil Placement and Compaction	46
6.3.1.	Axial Pull Test 1 (PT30): 30 in. Burial	47
6.3.2.	Axial Pull Test 2 (PT45): 45 in. Burial	48
6.3.3.	Axial Pull Test 3 (PT45b): 45 in. Burial	48
6.3.4.	Axial Pull Test 4 (PT60): 60 in. Burial	49
6.4.	Axial Pull Forces and Displacements	50
6.4.1.	Interpretation of Measurements	50
6.4.2.	Axial Pull Test 1 (PT30): 30 in. Burial Results	50
6.4.3.	Axial Pull Test 2 (PT45): 45 in. Burial Results	51
6.4.4.	Axial Pull Test 3 (PT45b): 45 in. Burial Results	54
6.4.5.	Axial Pull Test 4 (PT60): 60 in. Burial Results	55
6.5.	Comparison of Axial Load vs Displacement Performance	56
6.6.	Axial Pull Tests Summary	58
Section 7	Fault Rupture Simulation	60
7.1.	Introduction	60
7.2.	Experimental Setup	60
7.2.1.	Test Procedure	61
7.2.2.	Instrumentation	61
7.2.3.	Soil Preparation and Compaction Data	62
7.3.	Split Basin Test Results	67
7.3.1.	Test Basin Movements	69
7.3.2.	Internal Water Pressure	69
7.3.3.	End Loads	70
7.3.4.	Joint Opening	71
7.3.5.	Axial Strain and Force Distribution	72
7.3.6.	Bending Strain and Moment Distribution	74
7.4.	Post-Test Observations	76
7.5.	Summary of Split Basin Test	77
Section 8	Summary	80
8.1.	Tension Test Summary	80
8.2.	Compression Test Summary	80
8.3.	Four-point Bending Test Summary	81
8.4.	Axial Pull Tests Summary	82
8.5.	Summary of Large-Scale Fault Rupture Effects	82
8.6.	Significance of Test Results	83

List of Figures

<u>Title</u>	<u>Page</u>
Figure 1.1. Split Backup Ring and Wedge Action Restraint	2
Figure 1.2. Typical Installation of Restraining Joint on iPVC	2
Figure 2.1. Schematic of iPVC Tensile Coupon Specimen	4
Figure 2.2. Tensile Coupon Test Setup with iPVC Material	5
Figure 2.3. Stress vs. Strain Curve to Failure Using Clip-on Extensometer	6
Figure 2.4. Average Young's Modulus and Yield Stress from Strain Gage	6
Figure 2.5. Transverse vs. Axial Strain for Tensile Stress Below Proportional Limit	7
Figure 3.1. Plan View of Axial Tension Test	9
Figure 3.2. Test Apparatus and TT1 Specimen in the Direct Tension Frame	9
Figure 3.3. Cross-section of Restrained Pipe Joint	9
Figure 3.4. TT1 at Several Levels of Axial Displacement	12
Figure 3.5. Actuator and Joint Displacement vs. Time for TT1 Specimen	14
Figure 3.6. Tensile Load vs. Displacement for TT1 Specimen	14
Figure 3.7. Fracture of Wedge Action Restraint	14
Figure 3.8. Fracture of Restraining Collar Clamping Tooth Housing	15
Figure 3.9. TT1 Pipe Strains at North and South Gage Planes	16
Figure 3.10. Photo of TT2 Specimen at Failure	16
Figure 3.11. Actuator and Joint Displacement vs. Time for TT2 Specimen	17
Figure 3.12. Tensile Load vs. Displacement for TT2 Specimen	17
Figure 3.13. TT2 Joint Mechanism – Rotation of Clamping Teeth	18
Figure 3.14. TT2 Pipe Strains at North and South Gage Plane	18
Figure 3.15. Tensile Load vs. Joint Opening Comparison	18
Figure 4.1. Plan View of Compression Test Specimen	21
Figure 4.2. Compression Test Setup	24
Figure 4.3. Internal Pressure vs. Actuator Displacement for CT1	24
Figure 4.4. Axial Compressive Load vs. Joint Displacement for CT1	25
Figure 4.5. Pipe Strains on Bell and Spigot Planes for CT1	25
Figure 4.6. Post Test Images of Compression Test	25
Figure 4.7. Internal Pressure vs. Actuator Displacement for CT2	27
Figure 4.8. Axial Compressive Load vs. Joint Displacement for CT2	27
Figure 4.9. Pipe Strains on Bell and Spigot Planes for CT2	27
Figure 4.10. Internal Pressure vs. Actuator Displacement for CT3	29
Figure 4.11. Axial Compressive Load vs. Joint Displacement for CT3	29

Figure 4.12. Pipe Strains on Bell and Spigot Planes for CT3	29
Figure 4.13. Compression Test Load vs. Displacement Comparison	29
Figure 5.1. Profile View of Bending Test Including Instrumentation Location	33
Figure 5.2. Photo of Bending Test Setup	33
Figure 5.3. South Loading Support with End Cap, Roller and Saddle	34
Figure 5.4. Vertical Displacement vs. Time	37
Figure 5.5. Actuator Load vs. Time	37
Figure 5.6. Vertical Displacements Along the Pipe Specimen	37
Figure 5.7. Strains Measured at the Crown and Invert of Plane SG+65	39
Figure 5.8. Strains Measured at the Crown and Invert of Plane SG-65	39
Figure 5.9. Strains Measured at the Crown, Invert, East and West of Plane SG+22	39
Figure 5.10. Strains Measured at the Crown, Invert, East and West of Plane SG-22	39
Figure 5.11. Crown Strains at Various Levels of Loading	40
Figure 5.12. Invert Strains at Various Levels of Loading	40
Figure 5.13. Moment vs. Specimen Rotation	41
Figure 5.14. Testing Specimen at Four Levels of Displacement	42
Figure 5.15. Restraining Joint at Four Levels of Displacement	43
Figure 6.1 Plan View of Axial Pull Test Setup	45
Figure 6.2. RMS Graded Sand Particle Size Distribution	47
Figure 6.3. PT30 Axial Load vs. Displacement for Actuator, Load Cell, and Strain Gage Loads	52
Figure 6.4. Soil Surface Cracking after PT30	52
Figure 6.5. Photo of Sand Lodged Between Nuts and Collar of the Joint Restraint	52
Figure 6.6. PT45 Axial Load vs. Displacement for Actuator, Load Cell, and Strain Gage Loads	53
Figure 6.7. Soil Surface Cracking After PT45	53
Figure 6.8. PT45b Axial Load vs. Displacement for Actuator, Load Cell, and Strain Gage Loads	54
Figure 6.9. PT60 Axial Load vs. Displacement for Actuator, Load Cell, and Strain Gage Loads	55
Figure 6.10. Comparison Plots for Axial Pull Tests	57
Figure 6.11. Axial Load vs. Depth to Centerline of Pipe	58
Figure 7.1. Plan View of Split Basin Testing Setup	61
Figure 7.2. Instrumentation at (a) Restrained Joint and (b) Protective Enclosure	67
Figure 7.3 Plan View of Compaction Measurement Locations	67
Figure 7.4. Actuator Displacement vs. Time	69
Figure 7.5. Internal Water Pressure vs. Fault Displacement	70
Figure 7.6. North and South Pipe End Loads vs. Fault Displacement	70
Figure 7.7. Plan View of Restrained Joint	71

Figure 7.8. Joint Opening vs. Imposed Displacement	71
Figure 7.9. Distribution of Average Axial Strain Along the Specimen at Various Amounts of Fault Displacement	73
Figure 7.10. Distribution of Average Axial Force Along the Specimen at Various Amounts of Fault Displacement	73
Figure 7.11. Distribution of Bending Strain Along the Specimen at Various Amounts of Fault Displacement	75
Figure 7.12. Distribution of Bending Moment Along the Specimen at Various Amounts of Fault Displacement	75
Figure 7.13. Joint Opening Comparison of Fault Rupture and Direct Tension Tests	76
Figure 7.14. Overhead View of the (a) Pipeline and (b) Failed Joint After Excavation Following the Fault Rupture Test	78
Figure 7.15. View Looking North of (a) Failed Pipeline and (b) Close-Up of Ruptured Spigot	79

List of Tables

<u>Title</u>	<u>Page</u>
Table 2.1. Summary of Material Properties from Tensile Coupons	7
Table 3.1. Instrumentation List for PPI Tension Tests	11
Table 4.1. Instrumentation for Compression Test	21
Table 5.1. Instrumentation PPI Four-Point Bending Test	35
Table 6.1. Instrumentation List for iPVC Axial Pull Tests	46
Table 6.2. PT30 Compaction Data	48
Table 6.3. PT45 Compaction Data	48
Table 6.4. PT45b Compaction Data	49
Table 6.5. PT60 Compaction Data	49
Table 7.1. PPI Split Basin Strain Gage List	63
Table 7.2. PPI Split Basin Load Cell and Pressure Sensor List	66
Table 7.3. PPI Split Basin Displacement Instrumentation List	66
Table 7.4. PPI Split Basin Test Soil Dry Unit Weights	68
Table 7.5. PPI Split Basin Test Soil Water Content Data from Moisture Tins	68

Section 1

Introduction

This report is submitted to the Pyungwha Pipe Industry Co., Ltd. (herein referred to as PPI). It presents the results of a full-scale testing program to investigate the performance of 6-in. (150-mm)-diameter polyvinyl chloride pipe with a minimum wall thickness of 0.383 in. (9.73 mm), commercially available as iPVC pipe, with restrained joints. Testing was performed to evaluate how pipelines composed of iPVC pipe accommodate large ground deformation. In particular, the testing program was focused on pipeline response to fault rupture. Fault rupture is not only a major ground deformation hazard associated with earthquakes, but is representative of the most severe seismic ground deformation that occurs along the margins of liquefaction-induced lateral spreads and landslides.

1.1. Pipe Specimen and Joint Restraints

The full-scale experiments were performed at the Cornell University Large-Scale Lifelines Testing Facility of the Bovay Laboratory Complex on 6-in. (150-mm)-diameter, DR 18, AWWA C900 iPVC pipe with restrained joints. A description of iPVC pipe, including key material properties and mechanical performance characteristics, is provided by Hughes, et al. (2016).

The mechanical joint restraint system, which was used in the full-scale testing, involved Stargrip® Gen2 joint restraints manufactured by Star Pipe Products of Houston, TX, (Star Pipe Products, 2018). The joint restraint is composed of a wedge action restraint and a split backup ring, as shown in Figure 1.1. The wedge action restraint is clamped to the spigot, while the split backup ring relies on its geometry to rest on and make contact with the back of the pipe bell. A photo of a typical installation of the restraint on an iPVC pipe joint is shown in Figure 1.2.

The testing program addresses how iPVC pipelines with joint restraints accommodate large ground movements through pipe barrel axial deformation and flexure, as well as through axial slip and rotation of the joints. Although the main goal of the testing program is to characterize iPVC pipeline performance under earthquake-induced ground deformation, the test results also are applicable for pipeline performance in response to erosion and undermining by floods and hurricanes, landslides, tunneling, deep excavations, and subsidence related to mining, dewatering, and the underground extraction of petroleum-related fluids.

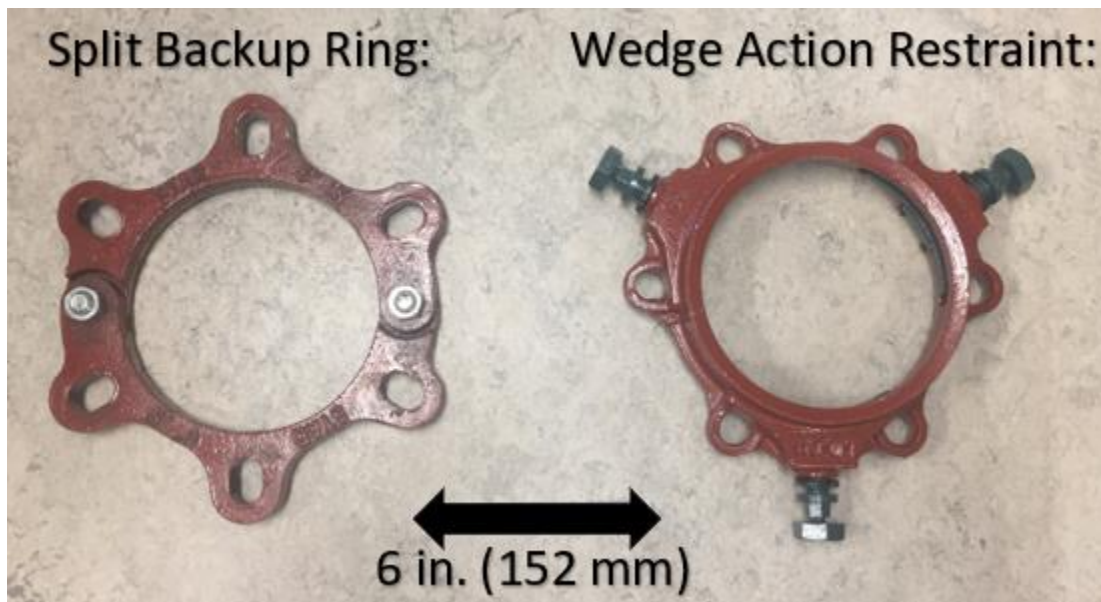


Figure 1.1. Split Backup Ring and Wedge Action Restraint

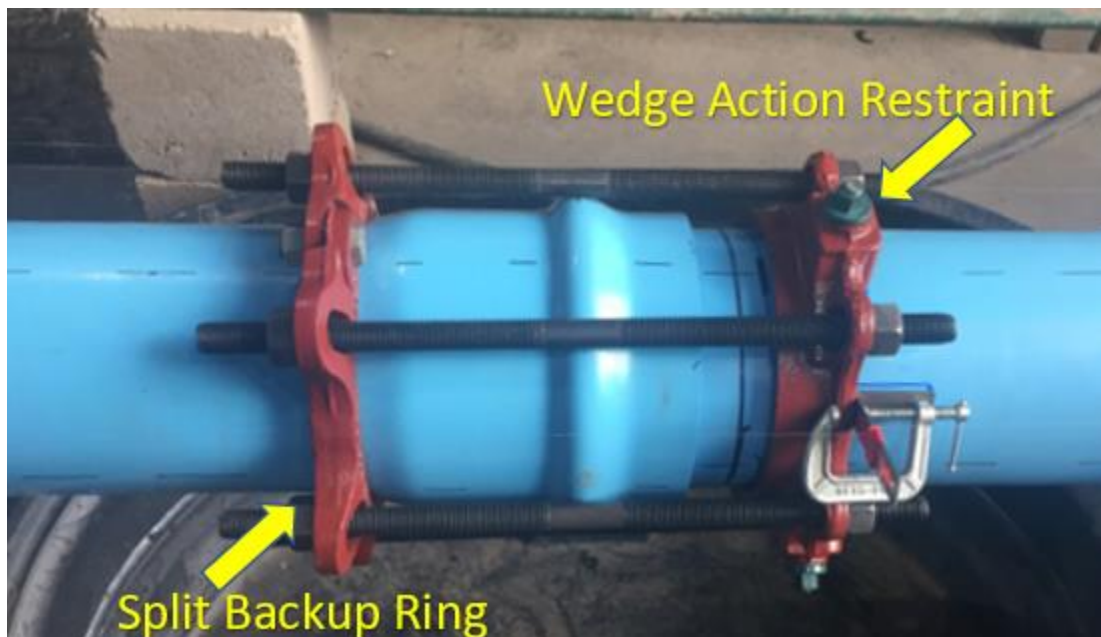


Figure 1.2. Typical Installation of Restraining Joint on iPVC

1.2. Report Organization

The report is organized into eight sections. Section 1 provides report organization and introductory information. Section 2 provides stress vs. strain properties of the iPVC material. Sections 3 and 4

cover the results of the direct axial tension and compression tests, respectively. Section 5 summarizes the four-point bending test, and Section 6 reports on the results of four axial pull-through tests on a restrained joint in dense sand. Testing concluded with a large-scale split basin fault rupture test. The experimental setup and results of this test are presented in Section 7. Section 8 summarizes the test results and discusses key findings.

Section 2

Material Characterization

2.1. Introduction

This section of the report describes the uniaxial tensile coupon testing and results for the iPVC pipe material. Tensile coupon specimens were cut and machined from 6-in. (150-mm)-diameter pipe sections and tested in accordance with the ASTM–D638 2014 Standard (ASTM, 2014).

2.2. Tensile Coupon Testing and Procedure

The nominal dimensions of the tensile coupon specimens are provided in Figure 2.1. Each specimen had a thickness of 0.25 in. (6.35 mm). A Baldwin Hamilton 60 BTE Universal Testing Machine was used to apply the tensile loads. The load frame was fitted with a pressure sensor to measure axial force. Figure 2.2 is a photograph of an iPVC specimen in the testing apparatus. The photograph shows axial and transverse gages on the test specimen as well a laser extensometer.

Three tensile coupon specimens were tested. All three specimens were instrumented with axial and transverse strain gages. The gages were mounted in the center of the reduced area of the specimen. Such gages frequently de-bond at tensile strains of 2 to 4%. To provide supplemental measurements of strain beyond the 2-4% range, a clip-on extensometer and laser extensometer were used to measure axial strain to failure. These devices are not as accurate as the strain gages at smaller strains but provide for a reliable assessment of strain at larger values, specifically those beyond the initiation of plastic deformation.

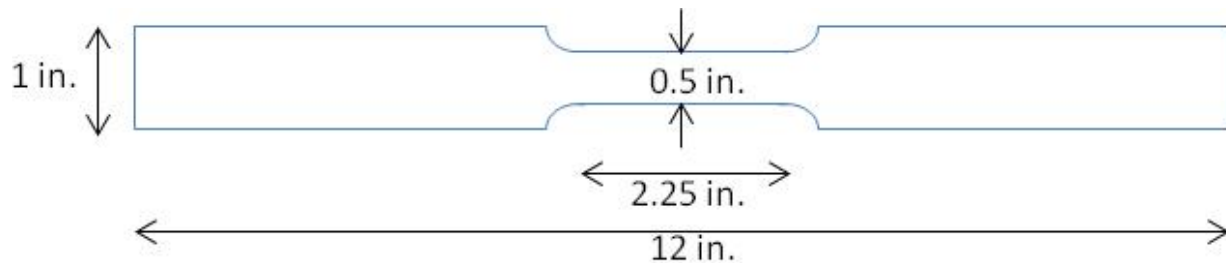


Figure 2.1. Schematic of iPVC Tensile Coupon Specimen

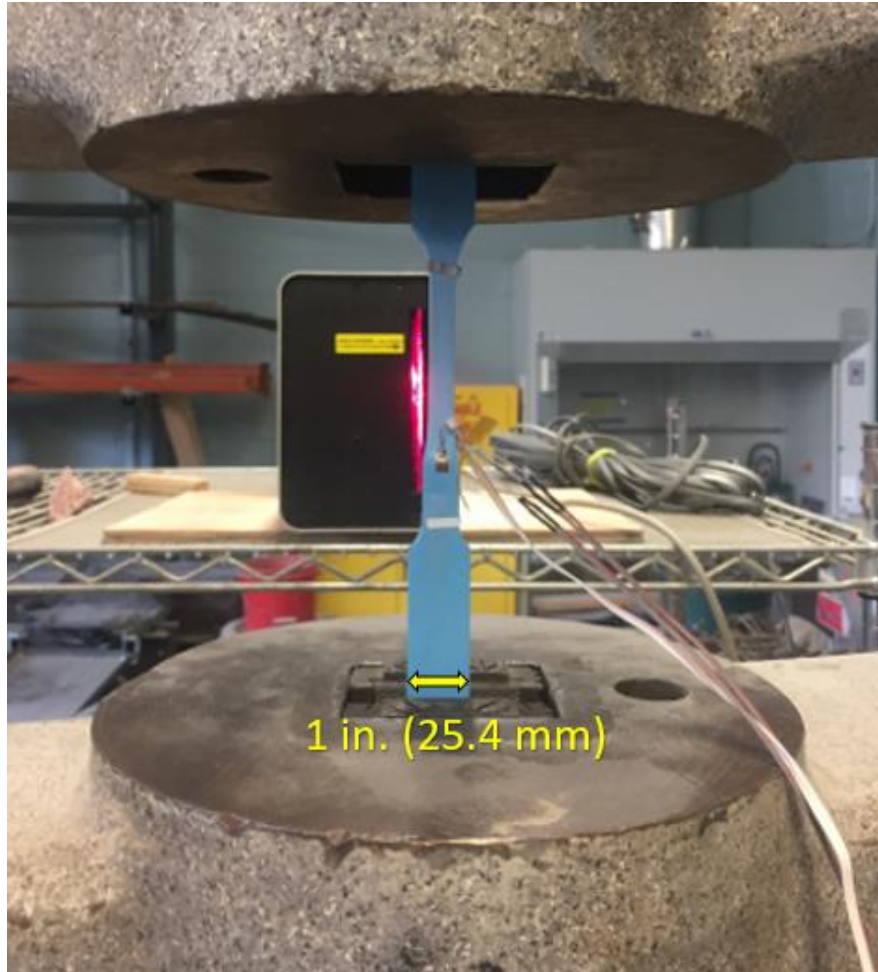


Figure 2.2. Tensile Coupon Test Setup with iPVC Material

2.3. Stress vs. Strain Data

The stress applied throughout the uniaxial tension test was computed by dividing the measured force by the original cross-sectional area of the tensile coupon. This strain generally is referred to as engineering strain. The uniaxial stresses vs. axial strains measured from clip-on extensometers for all three specimens are shown in Figure 2.3.

An expanded view of the stress vs. strain data is shown in Figure 2.4, in which the axial strain gage measurements were used to plot stress vs. strain to a level just beyond the elastic range. The results of all three tensile coupon tests show excellent agreement. Table 2.1 provides a summary of the Young's modulus, yield stress, peak tensile stress and strain, proportional limit and strain, ultimate tensile stress and strain, and Poisson's ratio determined from the tensile coupon specimens.

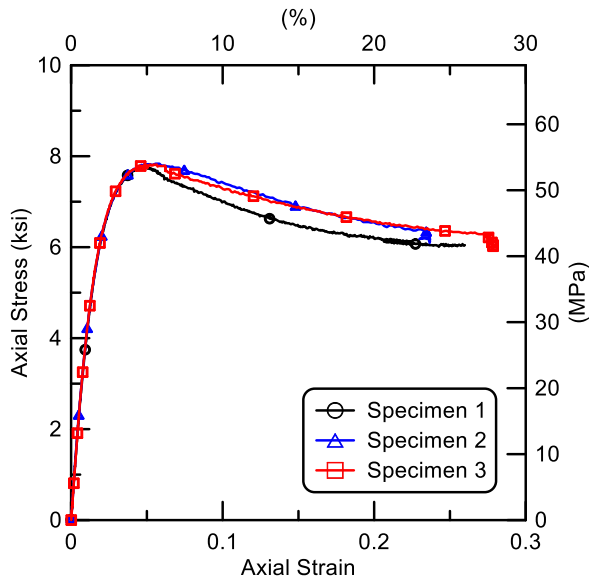


Figure 2.3. Stress vs. Strain Curve to Failure Using Clip-on Extensometer

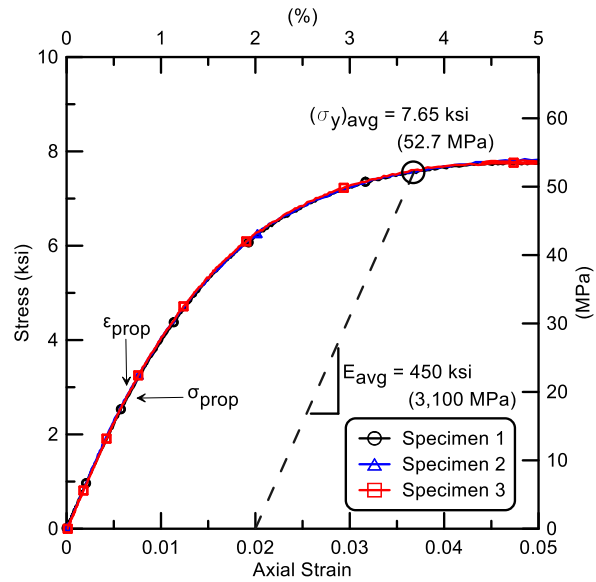


Figure 2.4. Average Young's Modulus and Yield Stress from Strain Gage

Young's modulus was computed using the linear range of the stress vs. strain plot. These data are shown to a strain of 0.05 in Figure 2.4. Young's modulus was determined by performing a linear regression for stress vs. strain from 0 to 2.8 ksi (0 to 19.3 MPa), for which 2.8 ksi (19.3 MPa) is the approximate proportional limit of the PVC. The yield strength, σ_y , was computed using the offset method, in which a line parallel to the linear part of the stress vs. strain plot is projected from 0.2% strain. The intersection of this line and the stress vs. strain curve provides an estimate of the yield stress for each specimen. Axial stress vs. strain data from the clip-on extensometers were used to determine the ultimate strength and strain, as shown in Figure 2.3.

Poisson's ratio, ν , is the negative ratio of transverse strain to axial strain for uniaxial loading. Poisson's ratio was derived from the transverse and axial strain gage data for strain to the proportional limit strain (0.0065), as shown in Figure 2.5. Poisson's ratio data for the specimens fitted with a transverse strain gage are presented in Table 2.1. The average Poisson's ratio for Specimens 2 and 3 was 0.38 with a standard deviation of 0.007.

Table 2.1. Summary of Material Properties from Tensile Coupons

		Specimen			Average	Standard Deviation
		1	2	3		
Young's Modulus, E	ksi (GPa)	446 (3.08)	457 (3.15)	448 (3.09)	450.3 (3.1)	5.9 (0.04)
Poisson's Ratio, ν		<i>N/A</i> ¹	0.37	0.38	0.38	0.007
Proportional Limit	ksi (MPa)	2.85 (19.6)	2.83 (19.5)	2.85 (19.6)	2.84 (19.6)	0.01 (0.06)
Proportional Limit Strain		0.0067	0.0065	0.0065	0.0065	0.0001
Offset Yield, σ_y	ksi (MPa)	7.6 (52.3)	7.6 (52.4)	7.6 (52.1)	7.6 (52.3)	0.02 (0.1)
Peak Tensile Strength	ksi (MPa)	7.8 (53.5)	7.8 (54.1)	7.8 (53.9)	7.8 (53.8)	0.042 (0.29)
Peak Tensile Strain	%	4.9	4.9	5.2	5.0	0.21
Ultimate Tensile Strength	ksi (MPa)	6.0 (41.6)	6.1 (42)	6.0 (41.5)	6.0 (41.7)	0.036 (0.25)
Ultimate Tensile Strain	%	26	24	28	26	2

¹*N/A* – Not available

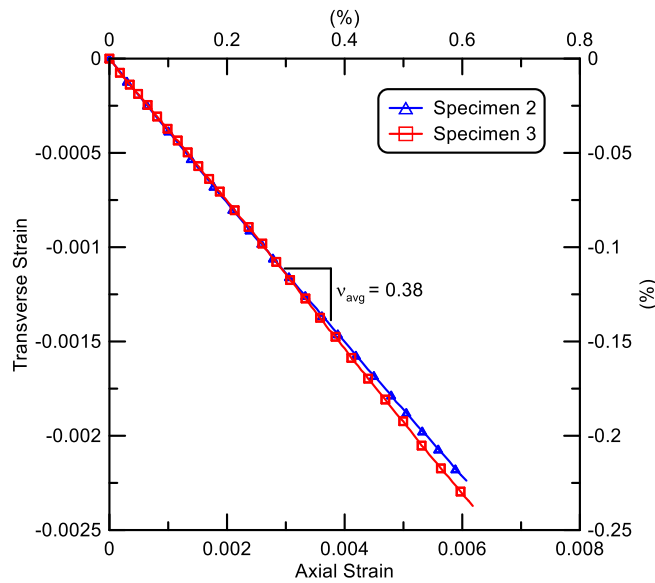


Figure 2.5. Transverse vs. Axial Strain for Tensile Stress Below Proportional Limit

Section 3

Axial Tension Tests

3.1. Introduction

This section summarizes the results of two direct tension tests on pipe specimens with a restrained iPVC joint. The tension test was performed with an internal water pressure. The tests are used to evaluate the axial pull-out capacity of the joint as well as the load vs. displacement characteristics of iPVC pipelines under axial elongation.

Figure 3.1 shows a plan view of the axial tension test setup and equipment. A 55 kip MTS actuator, load cell, and load frame were used to apply tensile load to the test specimen. The test specimens consisted of nominal 6 in (150 mm) diameter DR 18, AWWA C 900 iPVC pipe provided by PPI. The specimen was fitted at each end with end caps to allow for internal pressurization during loading. A photo of the test setup is shown in Figure 3.2.

Each specimen consisted of two sections of pipe joined by a bell and spigot joint. The joints were restrained axially by Stargrip® Gen2 joint restraints, manufactured by Star Pipe Products of Houston, TX. The restraints were assembled in accordance with directions from PPI to represent the configuration of restraint components in the field.

Figure 3.3 shows a cross-section of the restraint as assembled for testing with the positions and dimensions of all components. Six 0.75 in. (19 mm) threaded rods span the restraining collars at either side of the joint. Nuts on the threaded rods were loosened before the start of the test to allow approximately 1 in. (25 mm) of pullout before contact between the nuts on the threaded rods and the collars of the restraint.

3.2. Instrumentation

Figure 3.1 shows a plan view of the tension test setup and key instrumentation. The instrumentation listed in Table 3.1 was identical for each tension test. An actuator and load cell were installed at the south end of the load frame to apply and measure tensile force, respectively. The actuator had a tensile load capacity of 55 kips (245 kN) and stroke of 6 in. (150 mm). A series of three wedge

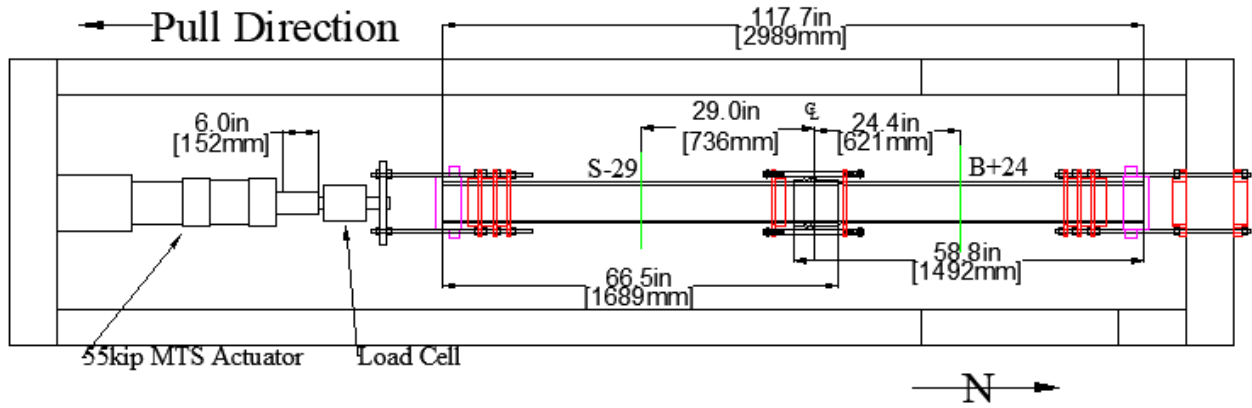


Figure 3.1. Plan View of Axial Tension Test

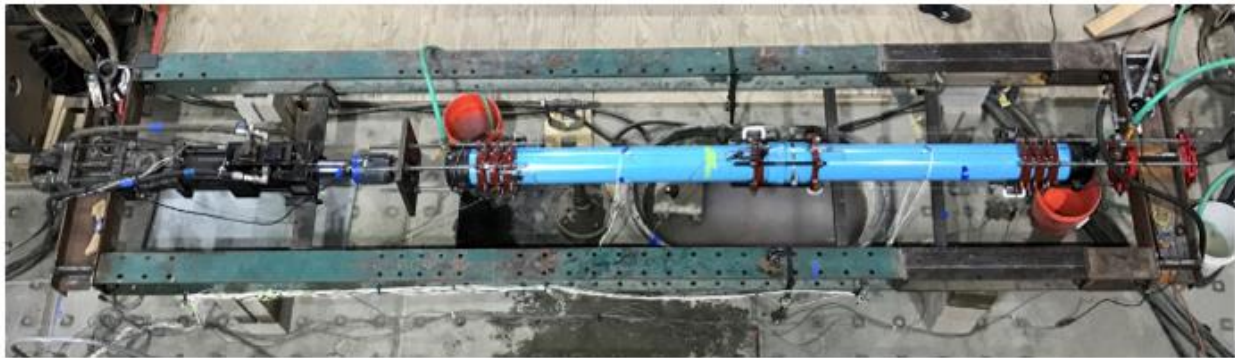


Figure 3.2. Test Apparatus and TT1 Specimen in the Direct Tension Frame

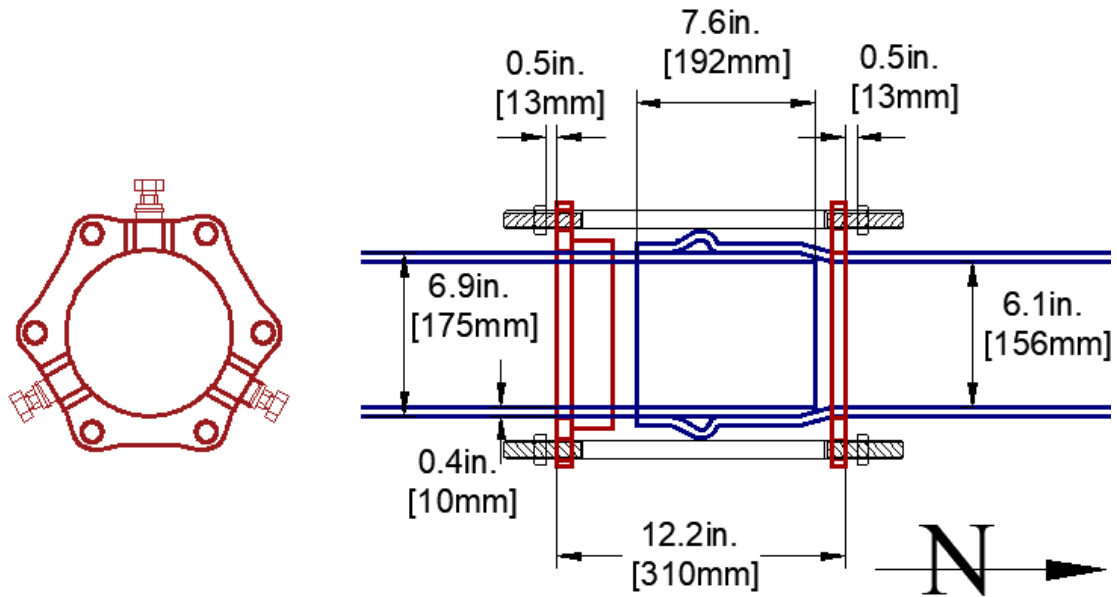


Figure 3.3. Cross-section of Restrained Pipe Joint

action restraints were used at either end of the specimen to transfer load from the actuator and loading frame to the specimen. The three restraining collars acted as a grip for the pipes during axial load application.

Two electronic pressure transducers, located at the north end cap, measured internal water pressure during the test sequence. Seven string potentiometers (string pots) were attached to the specimen and restraints at various locations to measure axial displacements along the specimen.

A total of ten strain gages were fixed to the exterior of the specimen at two planes, designated as S-29 and B+24, as shown in Figure 3.1. The plane locations were positioned approximately halfway between the joint restraint and gripping collars on the spigot (S-29) and bell (B+24) sides of the joint. At each plane the gages were located at the 12, 3, 6, and 9 o'clock positions (crown, east springline, invert, and west springline, respectively). Gage plane S-29 was positioned 29 in. (740 mm) south of the specimen centerline and included four gages oriented in the axial direction and two circumferential gages at the crown and invert. Plane B+24 with four gages was positioned 24 in. (620 mm) south of the specimen centerline and was equipped with axial and circumferential gages at both the crown and invert.

3.3. Test Sequence

After the specimen was instrumented and centered in the test frame the test sequence was initiated by starting the data acquisition system and laboratory hydraulic systems. The loading restraints at either end of the specimen were tightened to avoid any end movement due to pressurization. Approximately 80 psi (550 kPa) of internal water pressure was applied. The test was performed under displacement control using the servo-hydraulic actuator at the south end of the test frame. The actuator had a range of 6 in. (152 mm). The measuring systems were checked, and displacement to a maximum of 6 in. (152 mm) was applied. Displacement was applied until the specimen was no longer capable of holding internal water pressure.

Table 3.1. Instrumentation List for PPI Tension Tests

Location	Instrument Description	Local Instrument Name
24 in. (610 mm) North of Centerline	East, Axial Strain	SG+24EA
	Crown, Axial Strain	SG+24CA
	West, Axial Strain	SG+24WA
	Invert, Axial Strain	SG+24IA
29 in. (737 mm) South of Centerline	East, Axial Strain	SG-29EA
	Crown, Axial Strain	SG-29CA
	West, Axial Strain	SG-29WA
	Invert, Axial Strain	SG-29IA
	East, Circumferential	SG-29EC
	Crown, Circumferential	SG-29CC
	West, Circumferential	SG-29WC
	Invert, Circumferential	SG-29IC
S End to Bell	Horizontal String Pot	HSP_S_BELL
S End to S Restraint	Horizontal String Pot	HSP_S_S-REST
S Restraint to N Restraint	Horizontal String Pot	HSP_S-REST_N-REST
N Restraint to N End	Horizontal String Pot	HSP_N-REST_N
South of Load Frame	Actuator Displacement	55Kip_Displacement
South of Load Frame	Actuator Load	55Kip_Load
North End Cap	Pressure Sensor	Pressure

3.4. Experimental Results

The following subsections provide results from the two axial tension tests. Displacement vs. time relationships, load vs. joint opening, and strain measurements are discussed and compared in these sections.

3.4.1. TT1 Results

Figure 3.4(a) – (f) show photographs of the first tension test from the start of testing through leakage of the joint. The actuator axial displacement and joint opening vs. experimental time are shown in Figure 3.5. Actuator displacement is a direct measurement of the hydraulic piston movement. Joint opening represents the relative movement between the spigot and bell in the immediate vicinity of the restrained joint. The small joint opening at the beginning of the test ($t =$



a) Start of Test



(b) Allowable Axial Displacement



(c) Maximum Load



(d) First Slip



(e) Progression of Grip Slip



(f) Leakage After Depressurization

Figure 3.4. TT1 at Several Levels of Axial Displacement

25 to 100 seconds) was caused by Poisson's effect, which involves shortening of the specimen due to circumferential stresses induced by internal pressurization.

The applied displacement and joint opening are equal until about 175 seconds when approximately 1 in. (25 mm) of axial displacement had occurred. At this point the nuts on the rods contact the restraining collars generating axial tension in the system. The difference between the actuator displacement and joint opening after the initiation of tensile force in the restraint represents the axial elongation of the bell and spigot under tensile load.

Figure 3.6 shows the axial tension load vs. joint opening. Low force was required to open the joint until the joint restraint was engaged at approximately 1 in. (75 mm). At approximately 300 seconds and a joint opening of about 2.65 in. (67 mm) the specimen reached a peak tensile load of 26 kips (116 kN). At 3 in. (76 mm) of joint opening [3.71 in. (94 mm) of actuator displacement] a significant reduction in tensile load occurred, accompanied by an additional 0.50 in. (12.7 mm) of joint opening as the spigot slid relative to the bell and south joint collar. This event was concurrent with the fracture of two of the three clamping teeth housings of the wedge action restraint. This fracture allowed two of the clamping teeth to disengage contact with the pipe. Figure 3.7 shows an image of this type of fracture in the clamping teeth housing. No joint leakage was observed due to this event and loading was continued. The third clamping tooth remained in contact with the spigot throughout the test.

Further application of axial displacement was accompanied by a ratcheting movement of the spigot through the south restraining collar. Six additional abrupt displacement events occurred. The axial force during slip peaked at about 11 kips (48.9 kN) with a subsequent reduction to about 7 kips (31.1 kN) during each slipping event. The joint opening associated with each progressive movement was about 0.25 in. (6.4 mm).

It was known from a previous unrestrained pullout test on this specimen that the total axial pullout capacity of the joint was about 5.8 in. (147 mm). In that test no leakage was observed until axial displacement just below 5.8 in. (147 mm) was applied. It was decided to reduce pressure and readjust the actuator to apply additional displacement. When the pressure was reduced, the joint began to leak significantly. Upon repressurization the joint was unable to hold 80 psi (552 kPa). After the test the specimen was inspected for damage. Figure 3.8 shows the deep gouges below the east springline that were made by penetration into the pipe of the clamping tooth as the spigot slipped through the south restraining collar. The depth of these gouges was about ½ of the specimen wall thickness.

Strain gage results are presented for the axial and circumferential strain gages at the north and south midpoints of the pipe (planes S-29 and B+24). The gage measurements were used to provide a redundant measuring system for applied axial forces, assess the influence of internal pressure on circumferential strains, and to obtain a more comprehensive understanding of the pipe deformation.

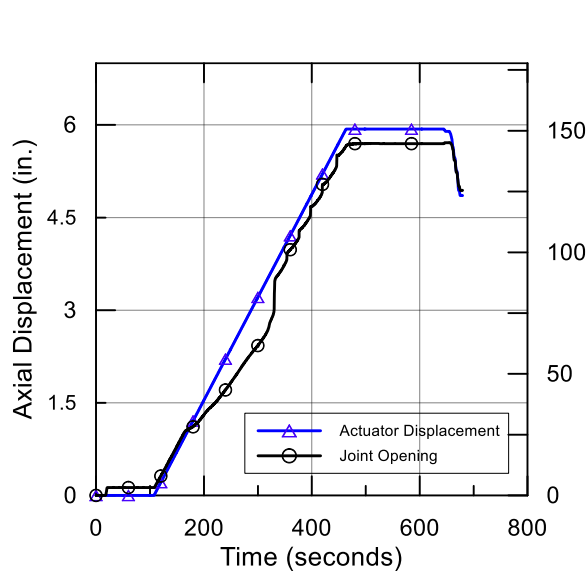


Figure 3.5. Actuator and Joint Displacement vs. Time for TT1 Specimen

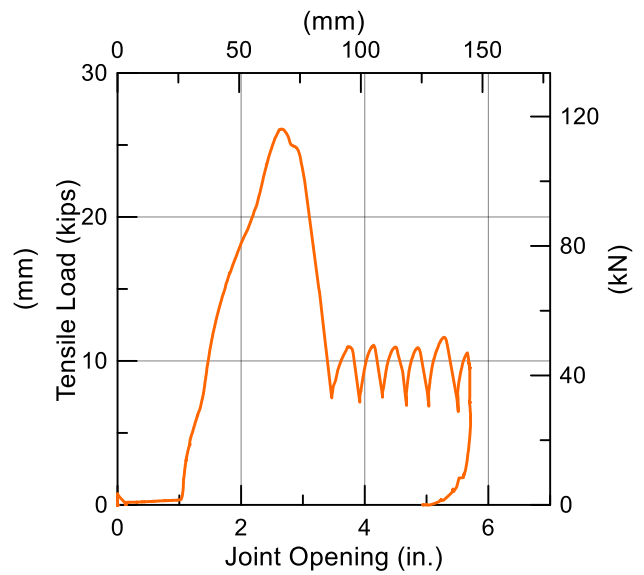


Figure 3.6. Tensile Load vs. Displacement for TT1 Specimen

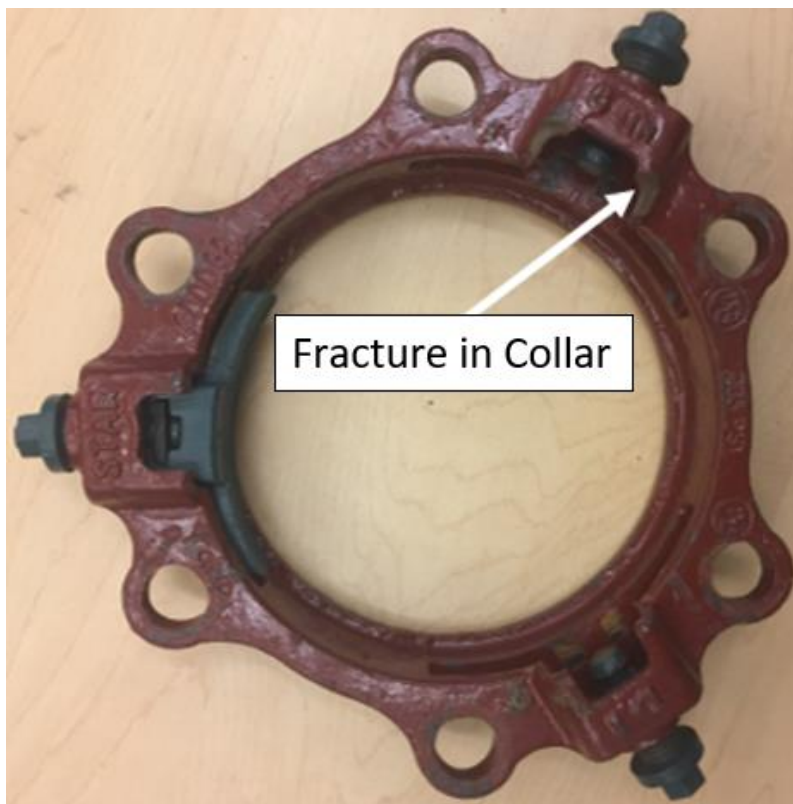


Figure 3.7. Fracture of Wedge Action Restraint

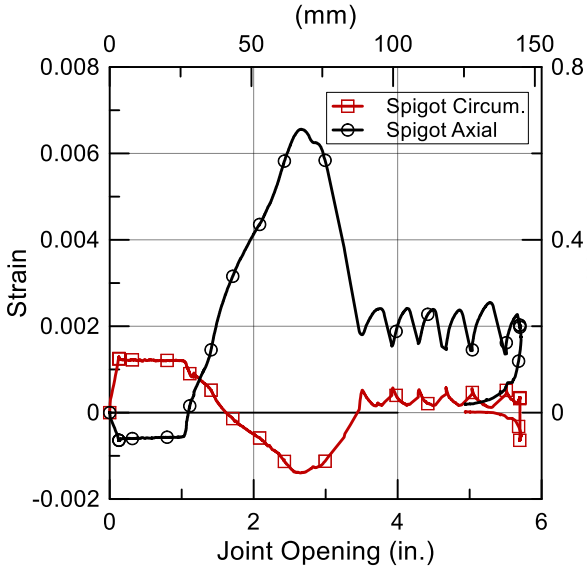


Figure 3.8. Fracture of Restraining Collar Clamping Tooth Housing

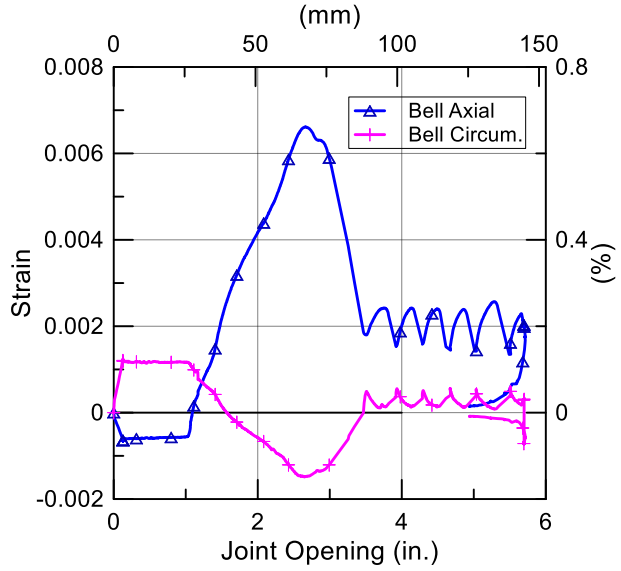
Figure 3.9 (a) and (b) show the average axial and circumferential strains at the north (bell) and south (spigot) gage planes. The north and south axial strains are virtually identical. Both the axial and circumferential strains show response to internal pressurization at the beginning of the test. The initial pressurization strains are $\epsilon_{axial} \approx -500 \mu\epsilon$ and $\epsilon_{hoop} \approx 1250 \mu\epsilon$. They are accompanied by a 0.13 in. (3.3 mm) joint opening. The average peak axial strain of 0.0066 (6560 $\mu\epsilon$) was slightly larger than the proportional limit strain determined from the tensile coupon specimen tests (peak strain ≈ 0.0065).

3.4.2. TT2 Results

The same testing setup and procedure for TT1 was followed for TT2. Figure 3.10 shows a photo of the test at failure. Figure 3.11 shows the actuator displacement and joint opening vs. experimental time for the second tension test. Similar to TT1, the small joint opening that occurs at the beginning of the test ($t = 90$ to 110 seconds) can be attributed to the Poisson's effect induced by internal pressurization. The applied displacement and joint opening are approximately equal up to an axial displacement of about 1.5 in. (38.1 mm). At this point, the test was paused ($t = 200$ to 400 seconds) to reset the actuator to its full capacity and check all instrumentation. Figure 3.12 is a plot of the axial tension force vs. joint opening for TT2. The peak tensile load of about 28 kips (125 kN) occurred at 2.79 in. (71 mm) of joint opening. After reaching the peak load, the axial



(a) Average Spigot Strains



(b) Average Bell Strains

Figure 3.9. TT1 Pipe Strains at North and South Gage Planes



Figure 3.10. Photo of TT2 Specimen at Failure

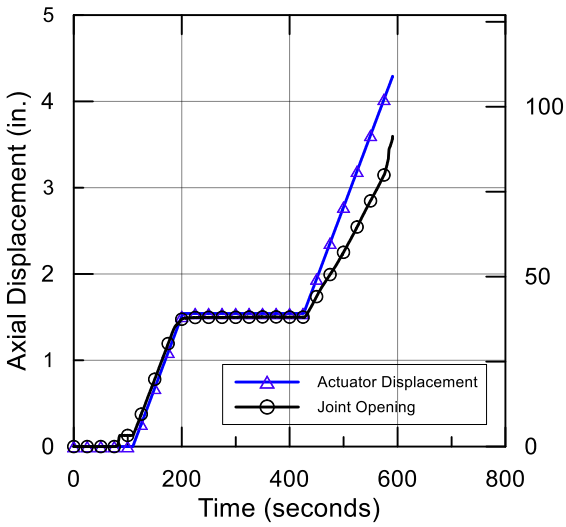


Figure 3.11. Actuator and Joint Displacement vs. Time for TT2 Specimen

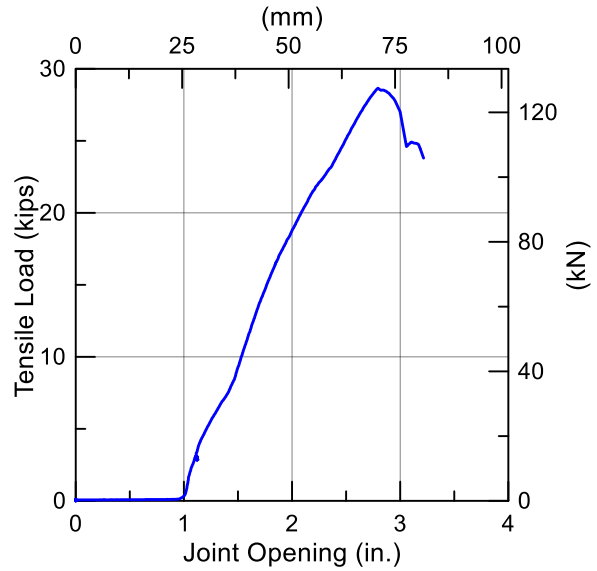


Figure 3.12. Tensile Load vs. Displacement for TT2 Specimen

force dropped sharply to less than 25 kips (111 kN) over 0.27 in. (6.9 mm) of joint opening. This drop in load can be attributed to the fracture of one of the three clamping teeth housings of the wedge action restraint as displayed in Figure 3.7. As shown in Figure 3.13(a)-(d), the remaining two clamping teeth rotated in the direction of the applied force, pinching into the pipe and causing failure. As Figure 3.10 shows, brittle failure of the specimen occurred at a joint opening of 3.2 in. (81.3 mm).

Strain gage planes were located at the same locations as used for TT1. The strains for the second tension test are shown in Figure 3.14. The initial pressurization strains are about $\epsilon_{axial} \approx -600 \mu\epsilon$ and $\epsilon_{hoop} \approx 1300 \mu\epsilon$ and are accompanied by a 0.13 in. (3.3 mm) joint opening. The average peak axial strain of 0.0071 (7093 $\mu\epsilon$) was slightly larger than the proportional strain established from tensile coupon specimens (peak strain ≈ 0.0065).

3.5. Tension Test Comparison

A comparison of the overall tensile load in relation to joint opening is shown in Figure 3.15 for the two separate tension tests. In both tests, fracture at the south restraining collar at the housings



(a) Start of Test



(d) Clamping Teeth Beginning to Rotate



(c) Clamping Teeth Induce Pinching Effect



(d) Failure

Figure 3.13. TT2 Joint Mechanism – Rotation of Clamping Teeth

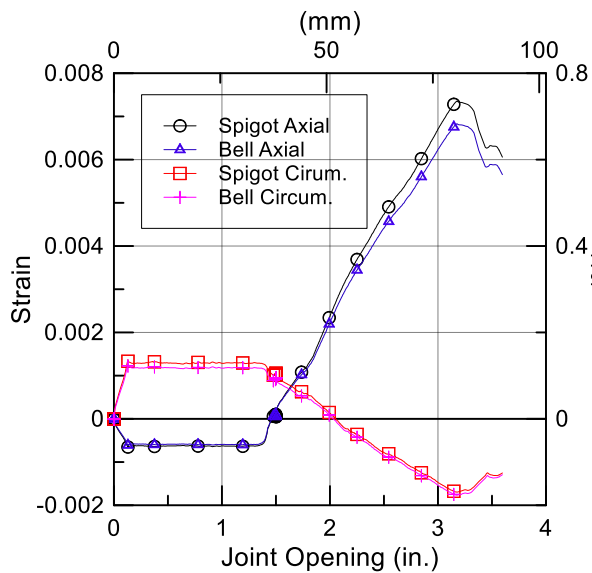


Figure 3.14. TT2 Pipe Strains at North and South Gage Plane

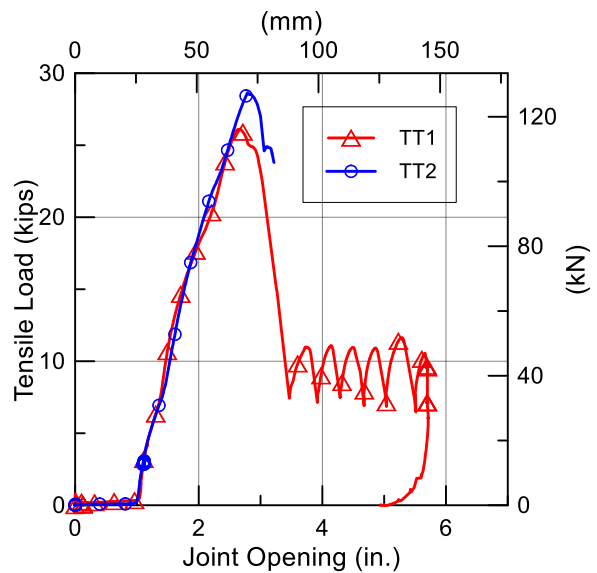


Figure 3.15. Tensile Load vs. Joint Opening Comparison

of the clamping teeth directly contributed to failure. In TT1, the collar fractured at two of these locations, allowing the pipe joint to open as the collar slipped relative to the pipe. In TT2, the collar fractured at one of these locations, leading to a brittle failure attributed to the concentrated strain created by the remaining two clamping teeth. TT1 reached a maximum tensile load of about 26 kips (116 kN) at a joint opening of 2.65 in. (67 mm), while TT2 reached a maximum tensile load of about 28 kips (125 kN) at a joint opening of 2.79 in. (71 mm). For TT1, no leakage was observed until after the actuator reached its full 6 in. (150 mm) displacement capacity. For TT2, the forces conveyed by the clamping teeth of the wedge action restraint led to a brittle failure of the specimen at 3.2 in. (81 mm) of joint opening. The average peak axial strain was slightly larger in TT2 at 0.0071 (7093 $\mu\epsilon$) compared with 0.0066 (6560 $\mu\epsilon$) mobilized in TT1. Both values were marginally larger than the strain at the proportional limit that was determined from tensile coupon specimens (peak strain \approx 0.0065).

3.6. Tension Test Summary

Two direct tension tests, TT1 and TT2, were performed in which the spigot was completely inserted into the bell for each test. Six 0.75 in. (19 mm) threaded rods spanned the restraints at either side of the joint. Nuts on the threaded rods were loosened prior to the start of the test to allow approximately 1 in. (50 mm) of pullout before engagement. The pipe was pressurized with water to approximately 80 psi (550 kPa) during the tests.

The TT1 pipe attained a maximum tensile load of 26 kips (116 kN) at a joint opening of 2.65 in. (67 mm). Once this maximum load was achieved, further axial displacement was accompanied by six episodes of abrupt ratcheting movement when pullout of the spigot occurred at approximately 6 in. (150 mm). The TT2 pipe attained a maximum load of 28 kips (125 kN) at 2.79 in. (71 mm) of joint opening, after which the load dropped steeply to 25 kips (111 kN) followed immediately by brittle rupture of the spigot at the joint restraint.

In both tests there was an abrupt increase in load after 1 in. (25 mm) of axial movement when the nuts on the threaded rods made contact with the restraining collars. This contact was followed by 1.65 in. (42 mm) and 1.79 in. (45 mm) of additional movement to a peak load of 26 kips (116 kN) and 28 kips (125 kN), respectively. The sudden drop in load after peak capacity was accompanied either by ratcheting until pullout (TT1) or pipe failure (TT2).

Section 4

Axial Compression Test

4.1. Introduction

Three axial compression tests were performed on pipe specimens with restrained iPVC joints. The purpose of the tests is to demonstrate and characterize the joints performance under axial compressive load, compressive displacement, and internal pressure.

The test specimens consisted of nominal 6 in. (150 mm) diameter DR 18, AWWA C 900 iPVC pipe provided by PPI combined with a joint restraint (Figure 1.1). As shown in Figure 4.1, the total specimen lengths were 126 in. (3.2 m). End caps were used at the ends of the specimen to apply internal water pressure and transfer load from the actuator and loading frame to the specimen. All three tests were run under substantially different axial loading rates to investigate rate of loading effects.

4.2. Instrumentation

The instrumentation and setup of the compression tests, as shown in Figure 4.1, were similar to those used in the tension test (Figure 3.1), with the only exception being that the overall specimen length was increased to 126 in. (3.2 m) to accommodate the retracted position of the actuator. The actuator had a load capacity of 55 kips (245 kN) and a stroke of 6 in. (150 mm). A list of the instrumentation is provided in Table 4.1. The instrumentation for the three compression tests was identical. String potentiometers (string pots) were set at various locations to record relative displacements. A load cell was used to record the applied axial load and a pressure transducer was used on the north end of the setup to record internal water pressure at the end cap during testing.

Strain gages were applied at the midpoints of the bell (north) and spigot (south) pipe specimens for each compression test. The two planes were designated SG+31 and SG-32, as shown in Figure 4.1. Gage plane SG+31 was located on the pipe at 31 in. (787 mm) north of the specimen centerline. Gage Plane SG-32 was located on the pipe at 32 in. (813 mm) south of the specimen centerline. Each plane had gages located at the crown, invert, and west and east springlines in both the axial and circumferential directions.

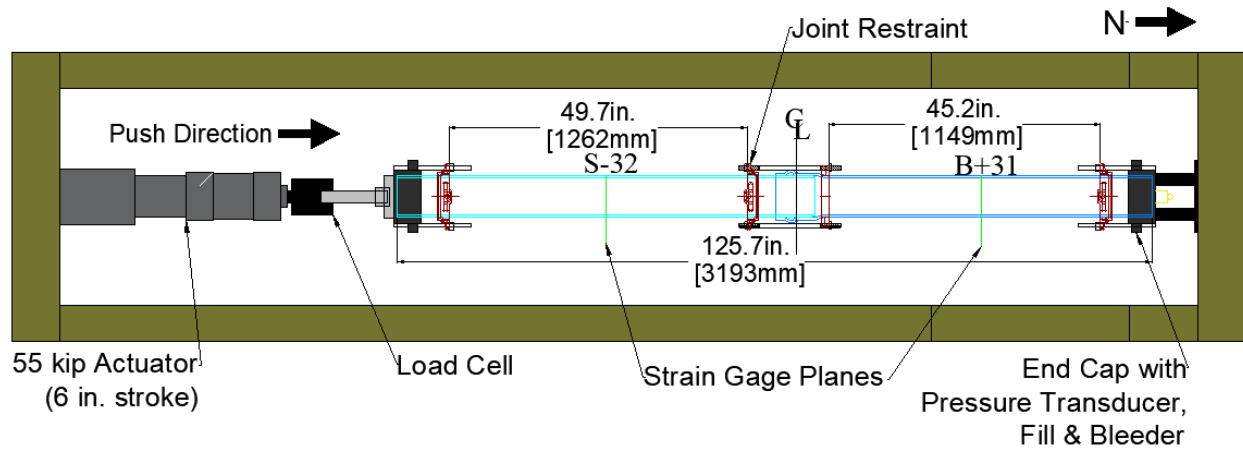


Figure 4.1. Plan View of Compression Test Specimen

Table 4.1. Instrumentation for Compression Test

Location	Instrument Description	Local Instrument Name
31-in. (787-mm) North of CL	East, Axial Strain	SG+31EA
	Crown, Axial Strain	SG+31CA
	West, Axial Strain	SG+31WA
	Invert, Axial Strain	SG+31IA
	East, Circumferential	SG+31EC
	Crown, Circumferential	SG+31CC
	West, Circumferential	SG+31WC
	Invert, Circumferential	SG+31IC
32-in. (813-mm) South of CL	East, Axial Strain	SG-32EA
	Crown, Axial Strain	SG-32CA
	West, Axial Strain	SG-32WA
	Invert, Axial Strain	SG-32IA
	East, Circumferential	SG-32EC
	Crown, Circumferential	SG-32CC
	West, Circumferential	SG-32WC
	Invert, Circumferential	SG-32IC
Spigot to Bell	Horizontal String Pot	HSP_SPIG-BELL
North End	Horizontal String Pot	HSP_N-SLIP
South End	Horizontal String Pot	HSP_S-SLIP
N-Rest. to S-Rest.	Horizontal String Pot	HSP_N-REST_S-REST
South of Load Frame	Horizontal String Pot	HSP_ACTUATOR
South of Load Frame	55 Kip Displacement	55Kip_Dis
South of Load Frame	55 Kip Load	55Kip_Load
North End Cap	Pressure Sensor	Pressure

4.3. Test Sequence

After each test specimen was instrumented and centered in the testing frame, the test sequence was initiated. The data acquisition system was started, followed by starting the laboratory hydraulic system. A loading plate attached to the actuator was tightened until it contacted the south end cap. An initial internal water pressure of 80 psi (550 kPa) was applied. Increased pressure was measured during the axial compression tests, as explained below. Each test was performed under displacement control using the servo-hydraulic actuator at the south end of the test frame. The 55 kip (245 kN) actuator had a 6 in. (152 mm) stroke. Once the measuring systems were checked, an initial 1 in. (25.4 mm) of displacement was applied, instrumentation response was verified, and the remaining displacement of 5 in. (127 mm) was applied.

4.4. Experimental Results

Three axial compression tests were run under three different rates of displacement. The tests were run at 1, 10, and 100 in./min. (25, 254, and 2540 mm/min.), and are herein referred to as CT1, CT2 and CT3, respectively. Different rates of loading were used to determine if compressive force and displacement response is rate of loading dependent.

Figure 4.2 shows how the bell and spigot were set at the beginning of each axial compression test. The spigot was set 1 in. (25 mm) from the back of the bell. This initial position allowed for the compressive load to be measured before the spigot came in contact with the back of the bell and was used to ensure response of the measuring systems before larger compressive loads developed.

4.4.1. CT1 Results

The first compression test was run at a rate of 1 in. (25 mm) per minute. The internal water pressure vs. actuator displacement for CT1 is plotted in Figure 4.3. After being set to approximately 80 psi (550 kPa) to begin the test, the pressure rises to a maximum of 106 psi (731 kPa) over the first 1 in. (25.4 mm) of displacement before a relief valve allowed the pressure to decrease and remain near 85 psi (586 kPa) for the remainder of the test. The specimen did not leak or rupture at any time during the testing sequence. All compressive movement occurred without compromising the internal seal provided by the gasket at the joint of the specimen.

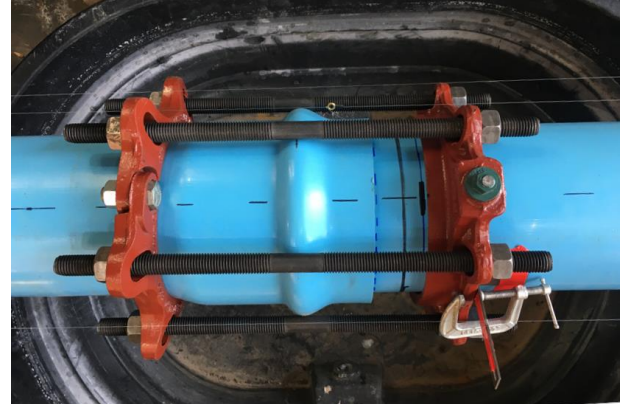
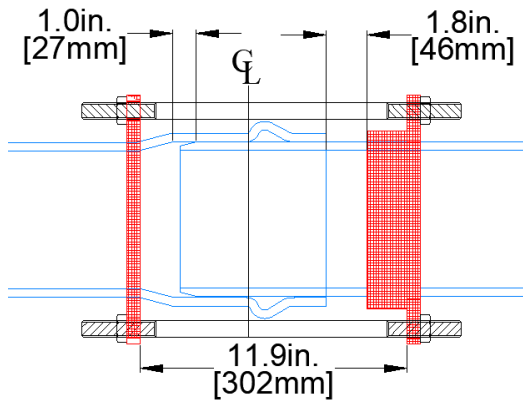
Figure 4.4 displays the compressive force vs. displacement response of the restrained joint. Several stages of loading are shown in the axial response, identified by letters A through D. At

approximately 1 in. (25 mm) of displacement (point A) the spigot contacts the back of the bell. After this point, force increases steeply until 2 in. (50 mm) (point B) of compressive displacement. An issue with the loading frame then arose requiring the test to be paused, and the actuator was retracted 1 in. (25 mm). Once the loading frame was reset, loading continued. At 2.3 in. (58 mm) of displacement, the spigot penetrated through the back of the bell and the split backup ring on the back side of the bell (point C). Movement of the wedge action restraint is mobilized at this point as the front face of the restraint contacts the bell face. The clamping teeth gouge into the spigot as the compressive displacement continues to increase. Once the spigot is penetrates past the bell and split backup ring, a decrease in load occurs (point D) followed by a steady increase in load. A total of 7 in. (178 mm) of actuator displacement resulted in 6.2 in. (157 mm) of maximum joint displacement and a maximum compressive load of 27.8 kips (123.7 kN).

The strain gage measurements were utilized to 1) assess the joint response to the applied load, 2) understand pipe barrel response to large deformation and 3) discern how this deformation response relates to the geometry of the adjacent pipe barrel. Axial and circumferential strain gage measurements taken during CT1 are shown in Figure 4.5. Average axial bell (north), axial spigot (south), and circumferential strain measurements were collected. The bell and spigot axial strains are nearly identical throughout the test. Both the axial and circumferential strains show some strain at zero displacement. These initial strains of about $\epsilon_{axial} \approx -0.075\%$ and $\epsilon_{hoop} \approx 0.15\%$ are due to initial internal pressurization. The maximum applied load resulted in maximum axial and circumferential strains of -0.80% and 0.45%, respectively.

Photos taken after the test are provided in Figure 4.6. The split backup ring position on the bell remained relatively stationary during the test as shown by Figure 4.6(a). The split back-up ring that was once resting on the back of the bell was now fixed in its place due to the expansion of the back of the bell that occurred when the spigot was forced through it.

After the test, the specimen was cut to reveal the circumferential deformation of the spigot. The deformed shape of the spigot is displayed in Figure 4.6(b). The reduction in spigot diameter is generated by circumferential wrinkling of its tapered end when thrust through the bell and split backup ring.



(a) Plan View of Joint Profile

(b) Initial Joint Condition

Figure 4.2. Compression Test Setup

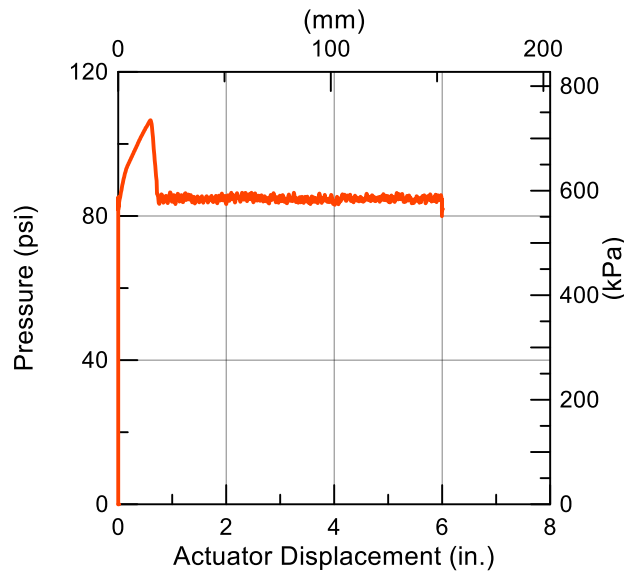


Figure 4.3. Internal Pressure vs. Actuator Displacement for CT1

4.4.2. CT2 Results

This section presents experimental results from the second (CT2) of three compression tests. CT2 was run at a rate of 10 in./min. (254 mm/min.). The internal water pressure vs. actuator displacement for CT2 is plotted in Figure 4.7. After being set to approximately 80 psi (550 kPa) to begin the test, the pressure rises to a maximum of 109 psi (751 kPa) over the first 1 in. (25.4 mm) of displacement before a relief valve allowed the pressure to decrease when the test was paused to verify instrumentation response. Pressure increased again and remained relatively constant at 108 psi (744 kPa) for the final 5 in. (127 mm) of actuator displacement. The specimen

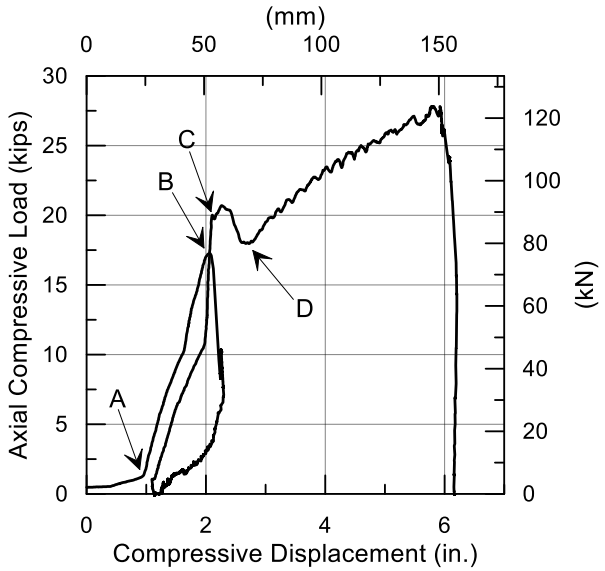


Figure 4.4. Axial Compressive Load vs. Joint Displacement for CT1

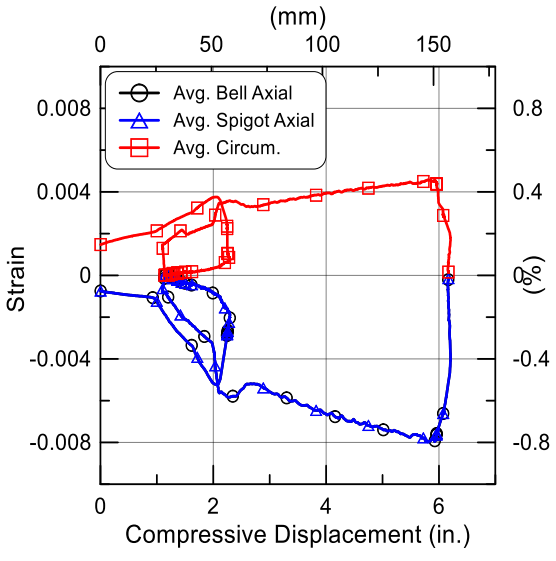
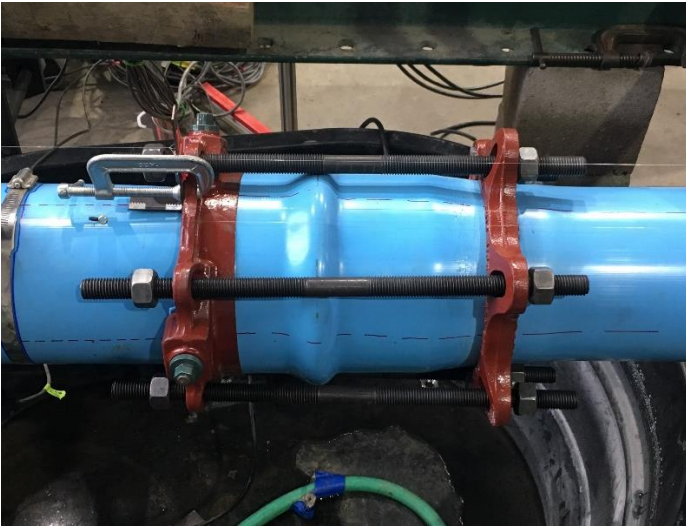


Figure 4.5. Pipe Strains on Bell and Spigot Planes for CT1



(a) Joint After Testing



(b) Internal Spigot Wrinkling

Figure 4.6. Post Test Images of Compression Test

did not leak or rupture at any time during the testing sequence. All compressive movement occurred without compromising the internal seal provided by the gasket at the joint of the specimen.

Figure 4.8 provides a plot of the compressive force vs. axial displacement of the restrained joint. The response of CT2 was similar to that of CT1. Several stages of the loading are shown in the axial response, identified by letters A through C (Figure 4.8). At approximately 1 in. (25 mm) of displacement (point A) the spigot contacts the back of the bell and the force steeply increases until 1.9 in. (48 mm) (point B) of compressive displacement. Movement of the wedge action restraint is also mobilized at this point as the front face of the restraint contacts the bell face. The clamping teeth gouge into the spigot as the compressive displacement continues to increase. At 2.6 in. (66 mm) of displacement, the spigot penetrates past the bell and split backup ring (point C). Once the spigot is submerged into the bell, a decrease in load occurs before the load steadily increases. The total of 6 in. (152 mm) of imposed actuator displacement resulted in 5.2 in. (132 mm) of maximum joint displacement and a maximum compressive load of 25.3 kips (112.5 kN).

The same strain gage measurements were utilized as CT1 to assess how the joint responds under the applied load. Axial and circumferential strain gage measurements that were taken during CT2 are displayed in Figure 4.9. Average axial bell (north), axial spigot (south) and average circumferential measurements are displayed. The bell and spigot axial strains are nearly identical. Both the axial and circumferential strains show some strain at zero displacement. These initial strains of about $\epsilon_{axial} \approx -0.075\%$ and $\epsilon_{hoop} \approx 0.15\%$ are due to initial internal pressurization. The maximum applied load resulted in maximum axial and circumferential strains of -0.71% and 0.44% , respectively.

Much like CT1, the split backup ring position on the bell remained relatively stationary during the test. Pictures taken after CT2 are identical to the images shown in Figure 4.6. The spigot was forced under the compressive load through the bell and split backup ring. Circumferential wrinkling of the spigot diameter occurred and resulted in a reduction of spigot diameter. This reduction of the spigot allowed it to insert itself through the back of the adjacent bell.

4.4.3. CT3 Results

This section presents experimental results from the third (CT3) of three compression tests. CT3 was run at a rate of 100 in./min. (2540 mm/min.). The displacement rates for CT1 and CT2 were 1 and 10 in./min. (25 and 254 mm/min.), respectively. The internal water pressure vs. actuator displacement for CT3 is displayed in Figure 4.10. After being set to approximately 80 psi (550 kPa) to begin the test, the pressure rises to a maximum of 110 psi (758 kPa) over the first 1 in.

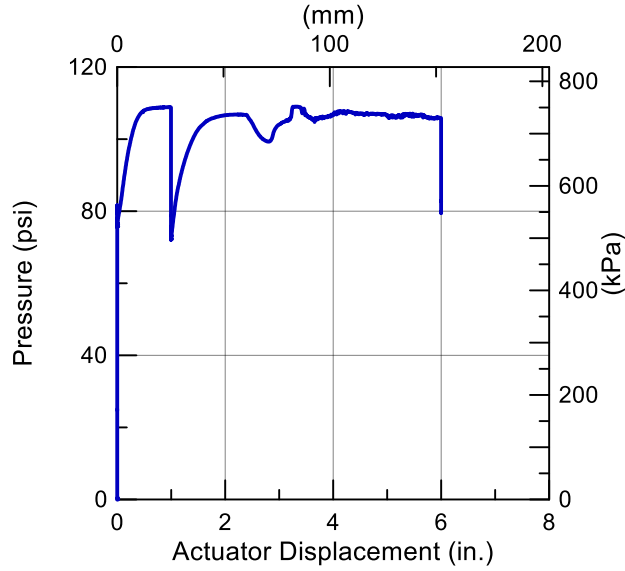


Figure 4.7. Internal Pressure vs. Actuator Displacement for CT2

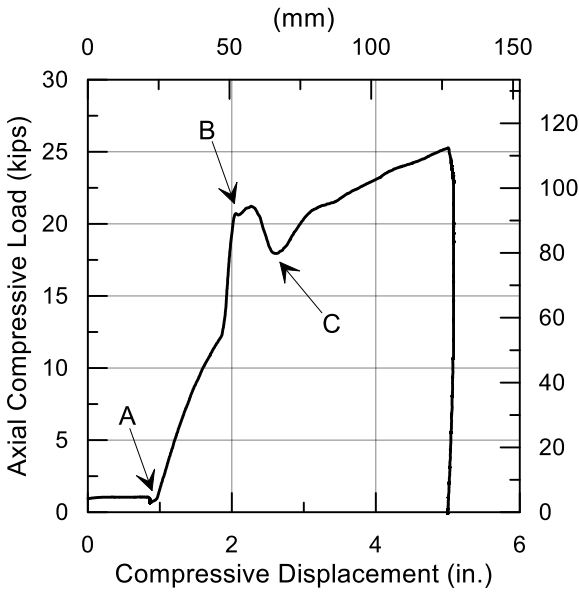


Figure 4.8. Axial Compressive Load vs. Joint Displacement for CT2

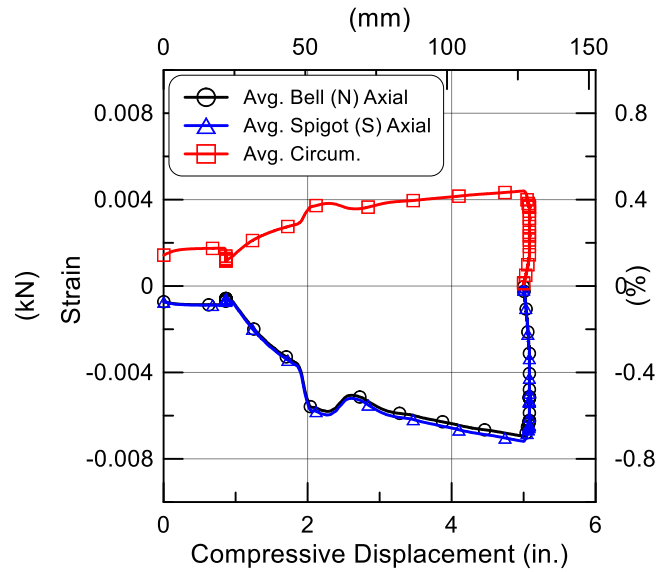


Figure 4.9. Pipe Strains on Bell and Spigot Planes for CT2

(25.4 mm) of displacement before a relief valve allowed the pressure to decrease when the test was paused to verify instrumentation response. Pressure increased again and remained relatively constant at 110 psi (758 kPa) for the final 5 in. (127 mm) of actuator displacement. The specimen did not leak or rupture at any time during the testing sequence. All compressive movement

occurred without compromising the internal seal provided by the gasket at the joint of the specimen.

Figure 4.11 displays the compressive force versus displacement response of the restrained joint in CT3. The setup of CT3 was the same as the first two compression tests. Several stages of loading in the axial response of CT3 are identified (letters A through C on Figure 4.11). At approximately 1 in. (25 mm) of displacement (point A) the spigot contacts the back of the bell and the force steeply increases until 2.3 in. (58 mm) (point B) of compressive displacement. At this point, the load drops, then increases, then subsequently drops again before finally increasing at a constant rate. The abrupt changes in load can be attributed to the wedge action restraint contacting the bell face in addition to the circumferential wrinkling of the spigot as it penetrates into the back of the bell. The back of the bell expands as the spigot is forced inside it.

During CT3, the split backup ring was forced down the barrel of the bell as the spigot inserted itself inside the bell. At 4 in. (102 mm) of displacement, the compressive force peaks at 25.2 kips (112.1 kN) (point C) as the spigot forces itself through and past the ring once the nuts on the restraint become engaged. The total of 6 in. (152 mm) of imposed actuator displacement resulted in 5 in. (127 mm) of maximum joint displacement and a corresponding max compressive load of 25.2 kips (112.1 kN).

The same strain gage measurements were used in all three compression tests to assess the joint response to the applied load. Axial and circumferential strain gage measurements that were taken during CT3 are shown in Figure 4.12. Average axial bell (north), axial spigot (south) and average circumferential measurements are displayed. The bell and spigot axial strains are nearly identical. Both the axial and circumferential strains show some strain at zero displacement. These initial strains of about $\epsilon_{\text{axial}} \approx -0.075\%$ and $\epsilon_{\text{hoop}} \approx 0.15\%$ are due to initial internal pressurization. The maximum applied load resulted in maximum axial and circumferential strains of -0.7% and 0.5%, respectively.

Unlike the first two compression tests, the split backup ring in CT3 did not stay stationary during the test. It moved down the barrel of the bell until a total compressive displacement of 4 in. (102 mm) before the spigot ultimately passed through the ring once the nuts on the restraint engaged. Post-test pictures of CT3 are similar to the images shown in Figure 4.6. A reduction in spigot

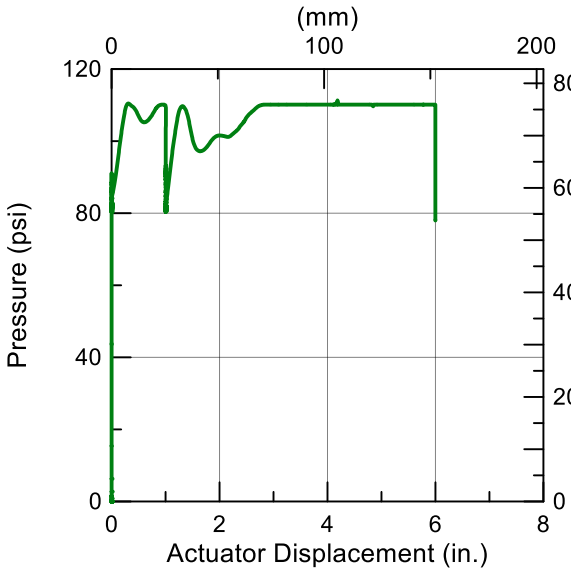


Figure 4.10. Internal Pressure vs. Actuator Displacement for CT3

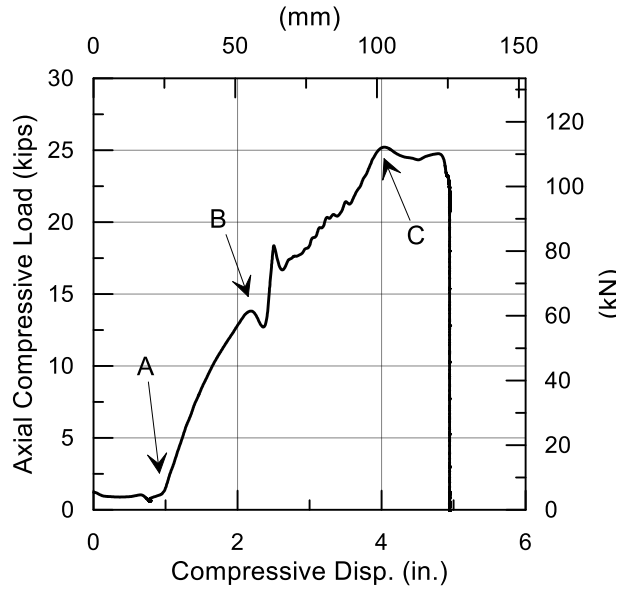


Figure 4.11. Axial Compressive Load vs. Joint Displacement for CT3

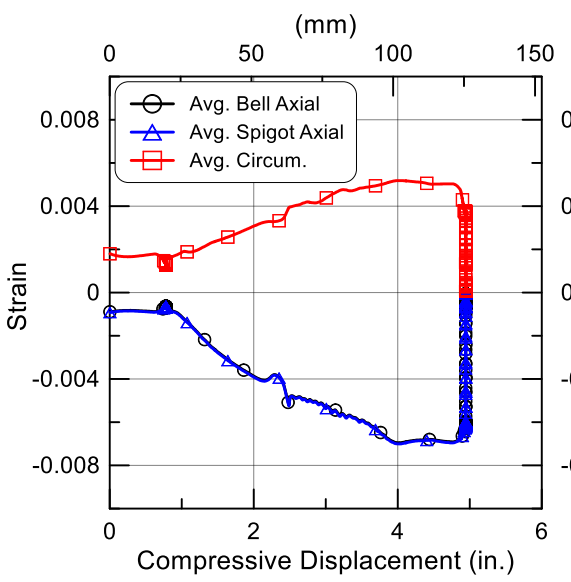


Figure 4.12. Pipe Strains on Bell and Spigot Planes for CT3

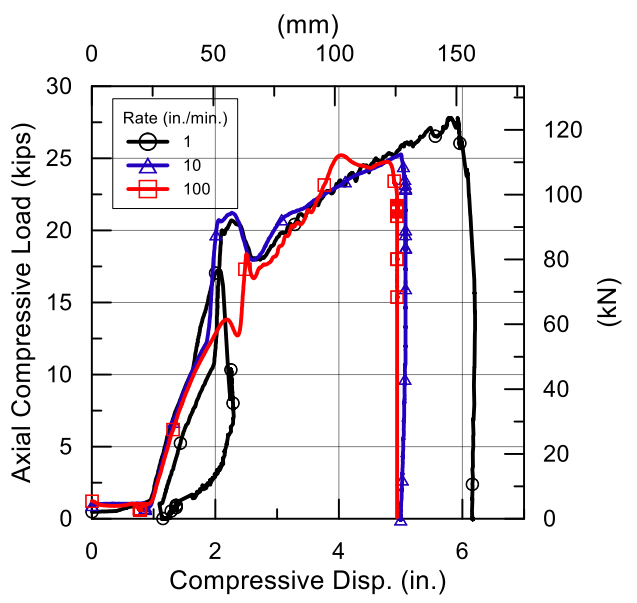


Figure 4.13. Compression Test Load vs. Displacement Comparison

diameter is generated by circumferential wrinkling of its tapered end when thrust through the bell and split backup ring.

4.5. Compression Test Comparison

A comparison of the compressive load vs. axial displacement is provided in Figure 4.13 for the three compression tests. In all tests, the spigot was set initially 1 in. (25 mm) from the back of the bell. The plot shows an almost identical initial stiffness response of all three test specimens as the axial displacement increases between 1 in. (25 mm) to 2 in. (51 mm). The CT1 and CT2 test results are very similar. In both tests, the spigot was pushed into the bell and past the split backup ring, causing a reduction in the spigot diameter through circumferential wrinkling. Both the CT1 and CT2 specimens show a temporary increase in axial load at 2.25 in. (57.2 mm) of displacement. After spigot penetration through the back of the bell and split backup ring, the axial force decreases in the CT1 and CT2 test results before increasing until the end of loading. In contrast, there is no temporary increase in force at 2.25 in. (57.2 mm) of axial displacement in the CT3 test results. The split backup ring moved down the barrel of the pipe with the applied compressive displacement until the nuts on both sides the restraint became engaged, thus holding the restraint in place. The spigot then was able to penetrate through the backup ring at 4 in. (101.6 mm) of displacement.

4.6. Compression Test Summary

Three compression tests were performed on 126 in. (3.2 m) long sections of iPVC pipe with the bell and spigot specimens restrained by a Stargrip® Gen2 joint restraints. A 55-kip (245 kN) actuator with a 6 in. (152 mm) stroke was used to apply compressive loads at three different rates of 1, 10, and 100 in./min. (25, 254, and 2540 mm/min.). All three specimens were set with 1 in. (25 mm) of separation between the back of the bell and spigot as shown in Figure 4.2. In all three tests, the joint was able to accommodate significant deformation without experiencing leakage at the joint. Average internal water pressure for CT1, CT2, and CT3 were 85 psi (586 kPa), 108 psi (744 kPa), and 110 psi (758 kPa), respectively. Even though the internal pressure increased to levels between 85 psi and 110 psi during the tests, the specimen did not leak or rupture at any time. In all three tests, the spigot was pushed past the back of the bell and split backup ring. In CT1 and CT2 the spigot penetrated the back of the bell and split backup ring simultaneously. In CT3 the spigot first penetrated the back of the bell as the split backup ring moved with the applied compressive displacement down the barrel of the bell. This movement of the split backup ring continued until engagement of the restraining mechanism. It is unlikely that this type of backup ring movement would occur if the restraint was confined by soil.

Through a change in rate of loading of over two orders of magnitude, the iPVC pipe with Stargrip® Gen2 joint restraints was able accommodate substantial compressive deformation with no failure or leakage under internal water pressure. For all three rates of loading, there is virtually no difference in the compressive load vs. axial displacement response. The compressive axial stiffness of the joint and restraint is essentially independent of loading rate for the three rates of loading investigated.

Section 5

Four-Point Bending Test

5.1. Introduction

The results of a four-point bending test performed on a 6 in. (150 mm) iPVC pipe with a restrained joint are presented in this section. Figure 5.1 provides a profile view of the test setup. Caps were installed at either end of the test specimen to allow for internal pressurization. The axial load applied from internal pressure at the beginning of the test resulted in 1 in. (25 mm) of joint opening from the fully inserted position of the spigot inside the bell. Once the pipe specimen was pressurized with the attendant joint opening, vertical displacement was applied to the specimen.

5.2. Setup and Instrumentation

Profile views of the test setup are shown in Figures 5.1 and 5.2. An MTS four-post load frame was used to apply the vertical load. The frame had a 6 in. (152 mm) servo-controlled stroke and a 200-kip (890 kN) capacity. Loading points were positioned at 30 in. (0.76 m) on either side of the joint center. Loading supports were positioned 90 in. (2.29 m) north and south of the joint center. Figure 5.3 shows the support saddles that were used at all four loading points. They were designed to minimize local deformation of the pipe as well as provide a bearing surface for the underlying roller.

Table 5.1 is a list of all instruments used during the bending test. A pressure transducer was employed at the north end cap to measure internal water pressure. Four planes of strain gages were installed along the specimen. Nine string potentiometers (string pots) were utilized to measure vertical displacements along the specimen. The gage planes and locations of string pots are shown in Figure 5.1. String pots were attached to the base of the frame and fixed to the invert of the specimen at intervals of 10, 30, 60, and 82 in. (250, 760, 1520, and 2080 mm, respectively) on either side of the specimen centerline. Each string pot is identified by its distance from the centerline. For example, VSP-10 was positioned 10 in. (250 mm) south of the centerline. Two additional string pots were used at the crown and invert of the joint to measure horizontal movement and rotation of the joint during deflection.

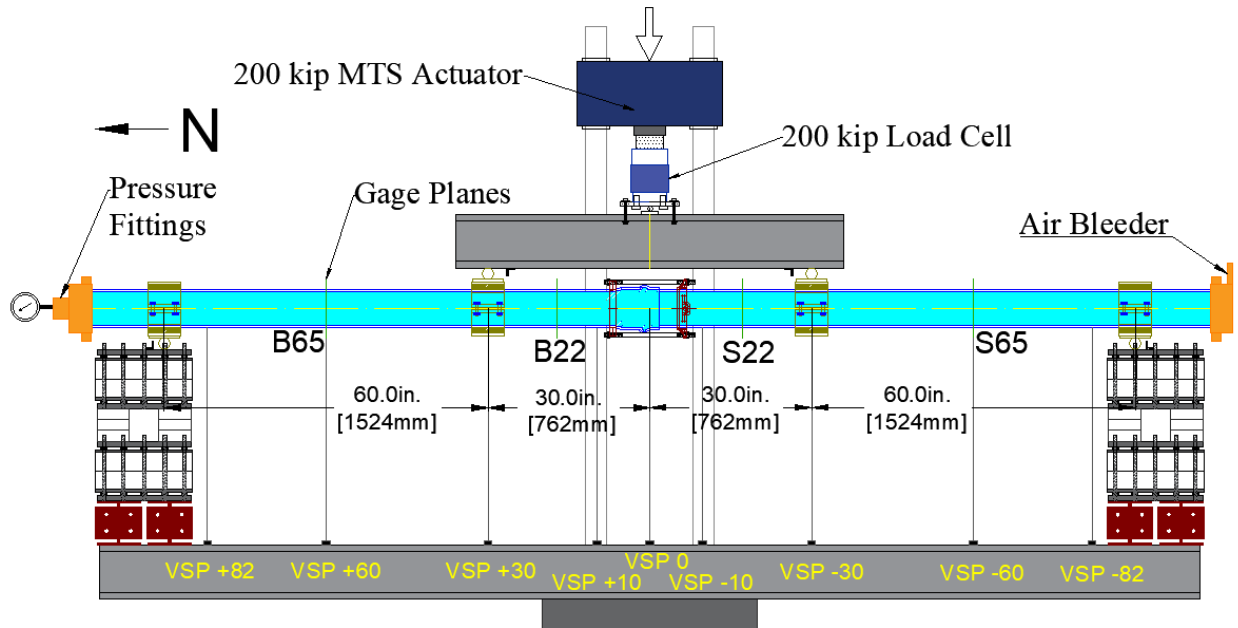


Figure 5.1. Profile View of Bending Test Including Instrumentation Location



Figure 5.2. Photo of Bending Test Setup

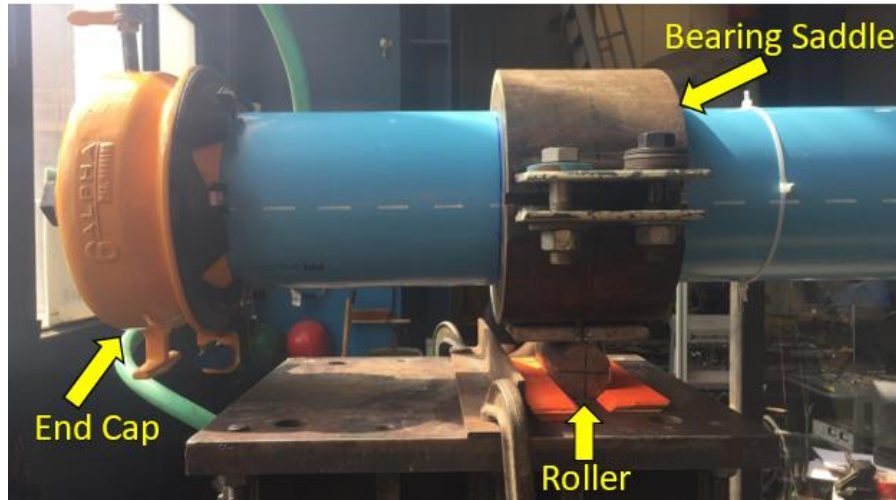


Figure 5.3. South Loading Support with End Cap, Roller and Saddle

5.3. Test Sequence

Once the specimen was instrumented, it was centered in the testing frame. The test specimen was then filled with water, and the testing sequence was initiated by starting the data acquisition system and turning on the load frame hydraulic power. The joint was opened through the axial force applied by internal water pressure to 1 in. (25mm). The internal pressure was applied at approximately 80 psi (550 kPa) throughout testing. A set of initial survey measurements were taken along the specimen's springline to establish its starting position. Supporting jacks at the mid-span of the bell and spigot were then manually lowered so that the pipe deflected under its self-weight. The cross-head and actuator of the frame were lowered until the spreader beam was in contact with the loading points (rollers).

Loading was applied by disengaging the locks on the loading frame and allowing the crosshead and spreader beam to move vertically. This crosshead displacement rate varied from 1.5 to 2.5 in./min. (38 to 63.5 mm/min.). Loading was paused twice at 10 in. (254 mm) and 18.5 in. (470 mm) of vertical displacement to survey vertical movement along the specimen springline. Crosshead displacement continued until approximately 22 in. (559 mm) of vertical displacement. At this time the crosshead of the loading frame was locked into place. Loading at a rate of 1 in./min. (25.4 mm/min.) was continued under servo control using the 6-in. (152-mm) stroke of the MTS actuator.

Table 5.1. Instrumentation PPI Four-Point Bending Test

Location	Instrument Description	Local Instrument Name
65 in. (1650 mm) North of CL	Crown, Axial Strain	SG+65CA
	Crown, Circumferential Strain	SG+65CC
	Invert, Axial Strain	SG+65IA
	Invert, Circumferential Strain	SG+65IC
22 in. (559 mm) North of CL	Crown, Axial Strain	SG+22CA
	Crown, Circumferential Strain	SG+22CC
	Invert, Axial Strain	SG+22IA
	Invert, Circumferential Strain	SG+22IC
	East, Axial Strain	SG+22EA
	East, Circumferential Strain	SG+22EC
	West, Axial Strain	SG+22WA
	West, Circumferential Strain	SG+22WC
22 in. (559 mm) South of CL	Crown, Axial Strain	SG-22CA
	Crown, Circumferential Strain	SG-22CC
	Invert, Axial Strain	SG-22IA
	Invert, Circumferential Strain	SG-22IC
	East, Axial Strain	SG-22EA
	East, Circumferential Strain	SG-22EC
	West, Axial Strain	SG-22WA
	West, Circumferential Strain	SG-22WC
65 in. (1650 mm) South of CL	Crown, Axial Strain	SG-65CA
	Crown, Circumferential Strain	SG-65CC
	Invert, Axial Strain	SG-65IA
	Invert, Circumferential Strain	SG-65IC
82 in. (2080 mm) North of CL	Vertical String Pot	VSP+82
60 in. (1520 mm) North of CL	Vertical String Pot	VSP+60
30 in. (760 mm) North of CL	Vertical String Pot	VSP+30
10 in. (250 mm) North of CL	Vertical String Pot	VSP+10
At CL	Vertical String Pot	VSP0
10 in. (250 mm) South of CL	Vertical String Pot	VSP-10
30 in. (760 mm) South of CL	Vertical String Pot	VSP-30
60 in. (1520 mm) South of CL	Vertical String Pot	VSP-60
82 in. (2080 mm) South of CL	Vertical String Pot	VSP-82
Crown	Horizontal String Pot	HSP_C
Invert	Horizontal String Pot	HSP_I
North End Cap	Pressure Sensor	Pressure Sensor 1
North End Control Valve	Pressure Sensor	Pressure Sensor 2
Above Specimen	200 Kip Load	200Kip_Displacement
Above Specimen	200 Kip Displacement	200Kip_Load

1 in. = 25.4 mm

5.4. Experimental Results

This section presents results from the four-point bending test. Measurements of applied load, vertical displacement, and specimen rotation are described. No leakage of the joint was observed at any time during the test.

5.4.1. Applied Vertical Displacement and Actuator Load

Figure 5.4 and Figure 5.5 show the vertical displacement and applied load respectively, vs. time. The first 2.9 in. (74 mm) of vertical displacement occurred when a pair of supporting jacks were removed from the midspan of both the bell and spigot, allowing the specimen to deflect under its self-weight. As shown in Figure 5.5, applied loading began at approximately 500 seconds by releasing the crosshead. At a vertical displacement of 10 in. (254 mm), corresponding to a time of approximately 700 seconds, the test was paused. This pause allowed for the manual survey of the specimen springline. A small reduction in load occurred during this pause, as shown in Figure 5.5. Loading continued at 1500 seconds to a vertical displacement of 18.5 in. (470 mm). Again, loading was paused for another set of survey measurements. A drop in load occurred during the second pause. It should be noted that at approximately 21 in. (584 mm) of displacement both the north and south support saddles slipped from their supporting rollers. Lateral movement was resisted at the south support while the specimen slipped through the north saddle. Loading was continued until 2900 seconds and a corresponding displacement of 22.2 in. (564 mm). At this time the crosshead of the loading frame was locked into place, and loading was continued at a rate of 1 in./min (25.4 mm/min) by the servo-controlled MTS actuator with 6-in. (152-mm) stroke. Loading was continued until 26.7 in. (678 mm). This was the maximum amount of displacement permissible by the geometry of the loading frame. The specimen was then unloaded and rebounded to a displacement of approximately 12.5 in. (317.5 mm) from its initial starting position. No leakage was observed at any time throughout the test.

Figure 5.6 is a plot of the vertical spring pot (VSP) displacements along the pipe. The figure shows very good agreement between displacements of string pots positioned at equal distances either side of the specimen's centerline. The figure shows the survey measurements that were taken along the springline at 10 in. (254 mm) and 18.5 in. (470 mm) of vertical displacement. These survey measurements are in excellent agreement with the displacement measurements of the string pots.

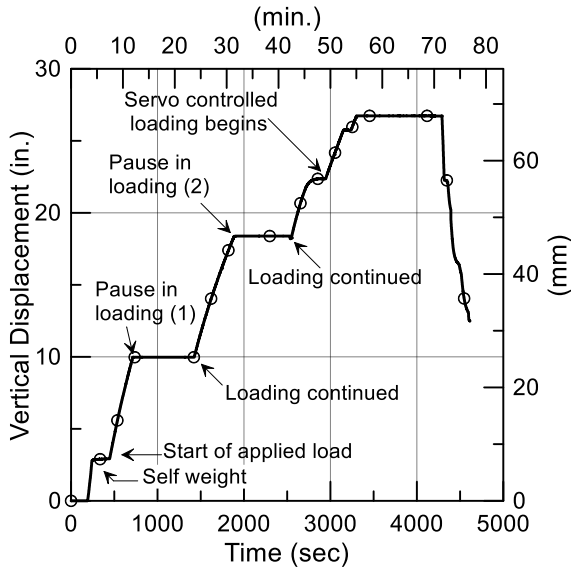


Figure 5.4. Vertical Displacement vs. Time

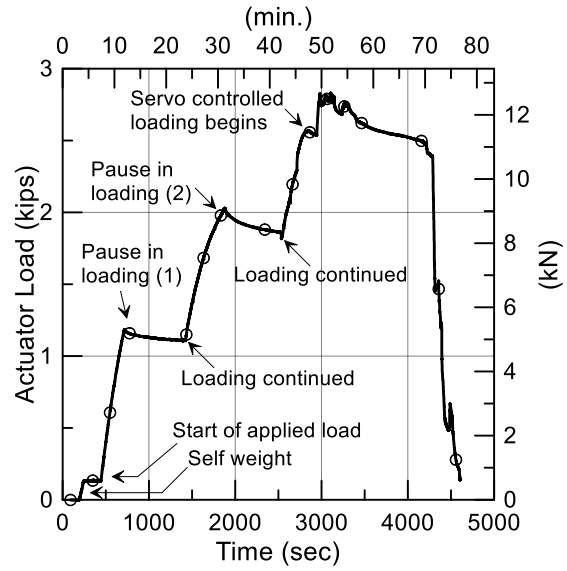


Figure 5.5. Actuator Load vs. Time

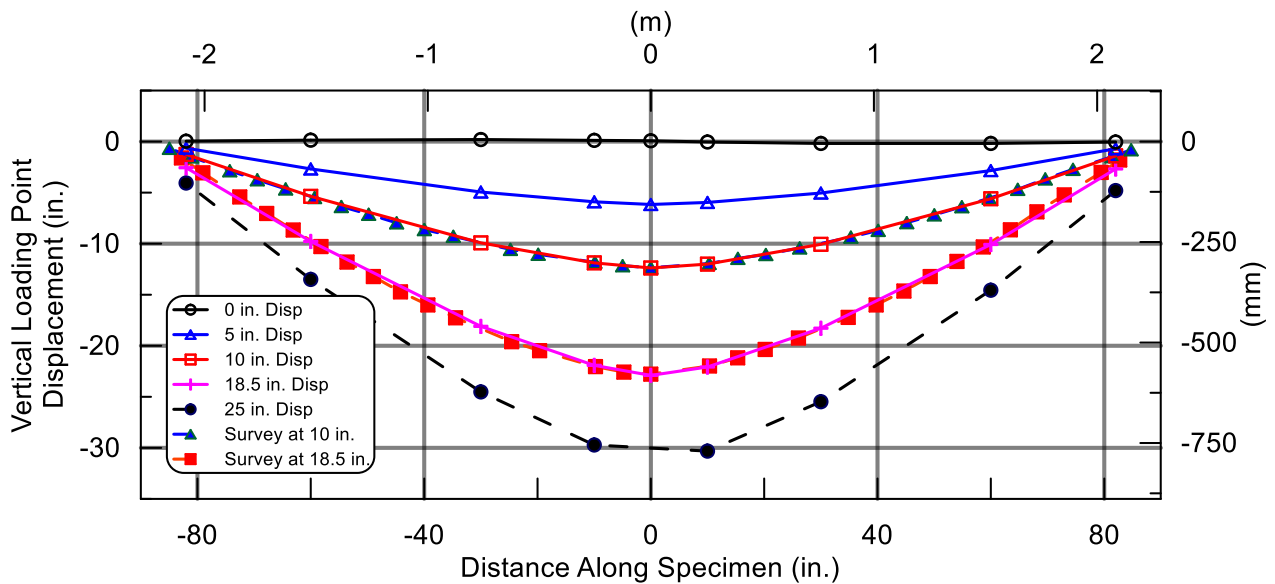


Figure 5.6. Vertical Displacements Along the Pipe Specimen

5.4.2. Bending Test Strains

As shown in Figure 5.1, strain gages were applied at four planes along the length of the test specimen. Strain gages were positioned at the crown and invert of the specimen at the SG+65 and SG-65 locations in both the axial and circumferential directions. These planes were placed approximately half way between loading points and loading supports on either side of the specimen. Figures 5.7 and 5.8 show the axial and circumferential strain gage measurements at

the pipe crown and invert for strain gage planes SG+65 and SG-65, respectively. These figures demonstrate the consistency and symmetry in strain measurements at two planes equidistant from the specimen center. Figures 5.9 and 5.10 show axial and circumferential strain gage measurements at the crown, invert, and springlines for gage planes SG+22 and SG-22, respectively. Gages at plane SG+22 recorded a maximum axial tensile strain of approximately 2.1% at the pipe invert and a maximum compressive strain of -1.9% at the crown. Plane SG-22 recorded similar tensile strains of approximately 2.0% and -1.8% on the invert and crown, respectively.

Figure 5.11 shows plots of measured crown strains at several levels of vertical displacement. Figure 5.12 provides plots of the invert strains at the same levels of displacement. Both figures show consistent patterns of movement both with respect to magnitude and symmetry of displacement. The strains located in the constant moment region of the pipe (between SG-22 and SG+22) increase approximately in equal amounts with each 5-in. (127-mm) increment of vertical displacement. They also increase much more rapidly than those located outside the constant moment region

5.4.3. Restrained Joint Moment-Rotation

Figure 5.13 shows the moment vs. rotation response during the four-point bending test. Rotation of the specimen is calculated as the arcsine of the vertical displacement at the VSP±30 string pot locations divided by the distance from the nearest loading point to the end support. The vertical displacements imposed on the specimen at both VSP-30 and VSP+30 are essentially identical as displayed in Figure 5.6. The linear trend induced by the loading is the same at both sides of the specimen. The relative rotation in Figure 5.13 is calculated as the sum of the vertical string pot rotations calculated using both the VSP+30 and VSP-30 locations along the specimen. The deflection at these two locations represents the rotation of the specimen that occurs at the loading points.

Idealized beam theory is used to calculate the moment that is plotted in Figure 5.13. The equation to calculate this moment is shown in Equation 5.1 with P representing the load applied by the test

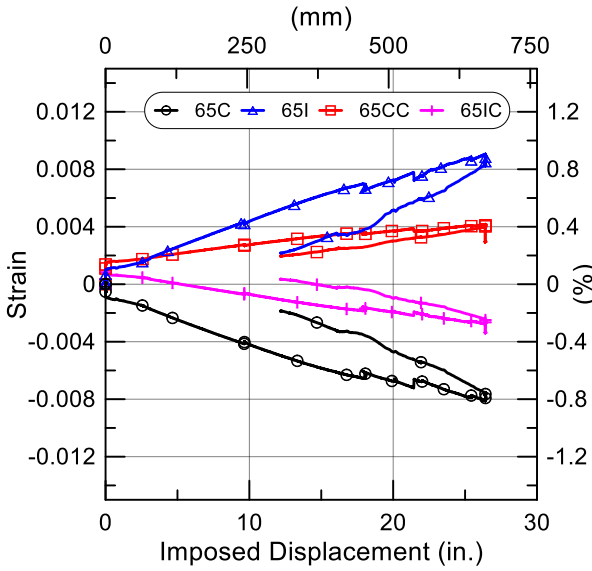


Figure 5.7. Strains Measured at the Crown and Invert of Plane SG+65

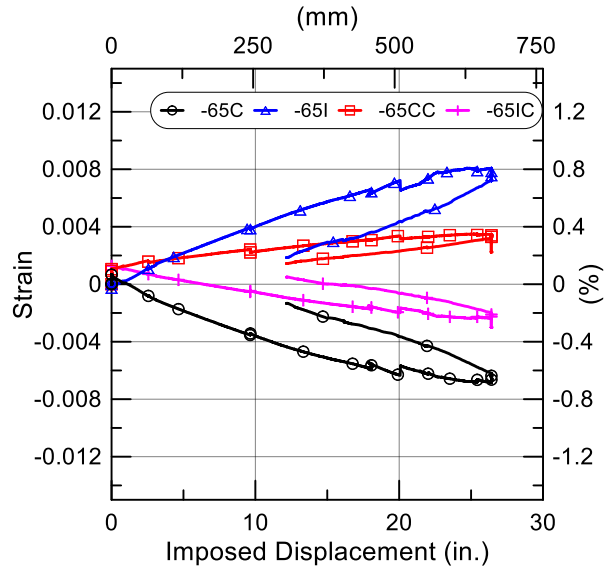


Figure 5.8. Strains Measured at the Crown and Invert of Plane SG-65

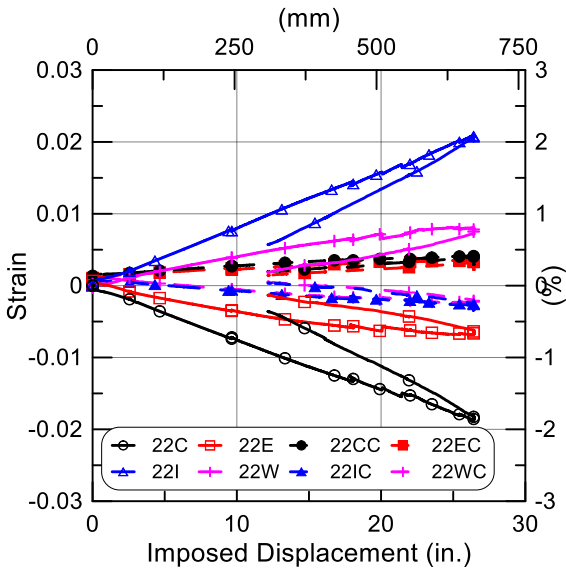


Figure 5.9. Strains Measured at the Crown, Invert, East and West of Plane SG+22

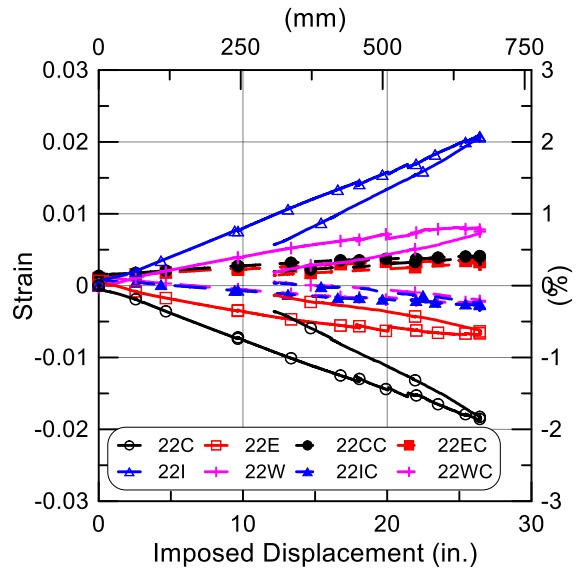


Figure 5.10. Strains Measured at the Crown, Invert, East and West of Plane SG-22

frame, weight of the specimen with water, and the loading saddles. The distance from loading point to the nearest end support, l_s , is equal to 60 in. (1.5 m) as shown in Figure 5.1.

$$M = \frac{Pl_s}{2} \quad (5.1)$$

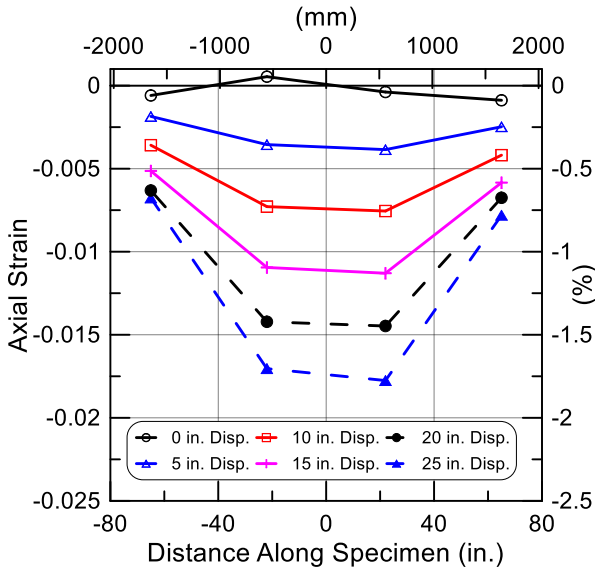


Figure 5.11. Crown Strains at Various Levels of Loading

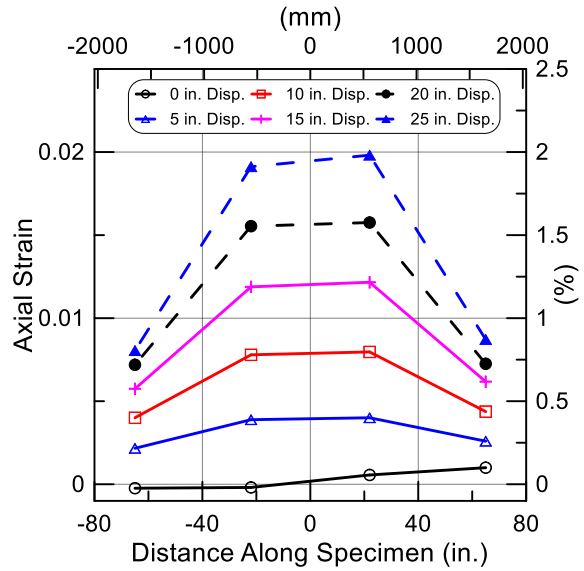


Figure 5.12. Invert Strains at Various Levels of Loading

The moment-rotation relationship in Figure 5.13 increases at mostly linear rate until roughly 42 degrees of rotation. As previously mentioned, the test was paused for survey measurements twice during its execution. Those pauses are shown as a slight decrease in the moment on the plot at about 19 degrees and 35 degrees, respectively. Servo-controlled loading began at 42 degrees of rotation and continued until a maximum 52.2 degrees and corresponding moment of 90.8 kip-in. (10.3 kN-m). At this maximum rotation, the geometric limits of the testing frame were met, and the applied load was released from the specimen.

5.4.4. Specimen Deflection

Figures 5.14a, b, c, and d show photos of the initial position of the specimen, as well as its position at 10 in. (254 mm), 18.5 in. (470 mm), the maximum 26.7 in. (678 mm) of vertical displacement, respectively. This sequence of photos shows graphically the ability of the specimen to accommodate a large amount of deflection without failure or leakage. The maximum deflection occurred at 52.2 degrees of rotation, as shown and defined in Figure 5.14d.

Figure 5.15 shows photos of the specimen restrained joint at the previously mentioned levels of vertical displacement. At the beginning of the test, all threaded rods spanning the joint were experiencing relatively low force due to the internal pressurization. Once load was applied and vertical displacement occurred, outward rotation of the collars caused the threaded rods at the

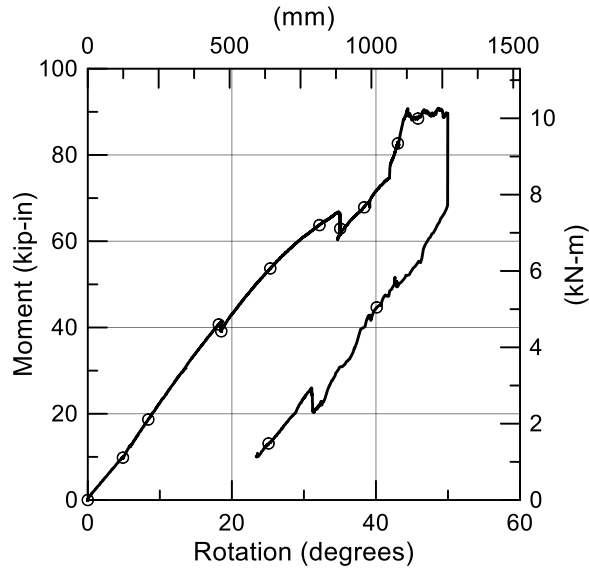
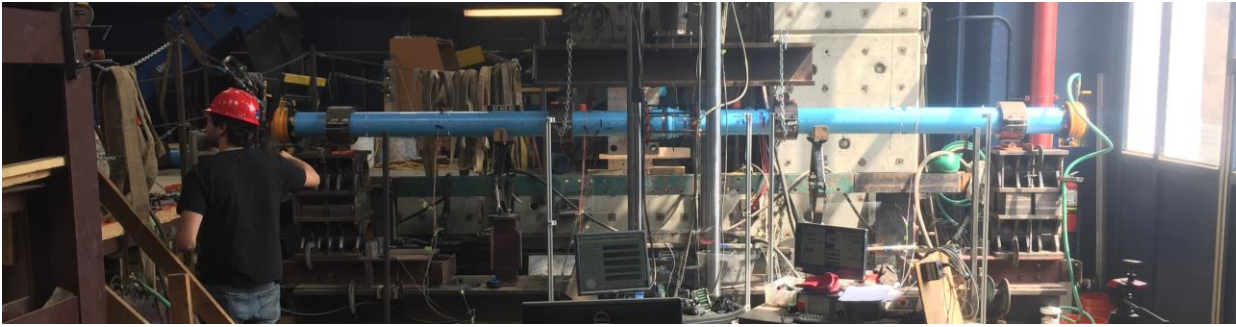


Figure 5.13. Moment vs. Specimen Rotation

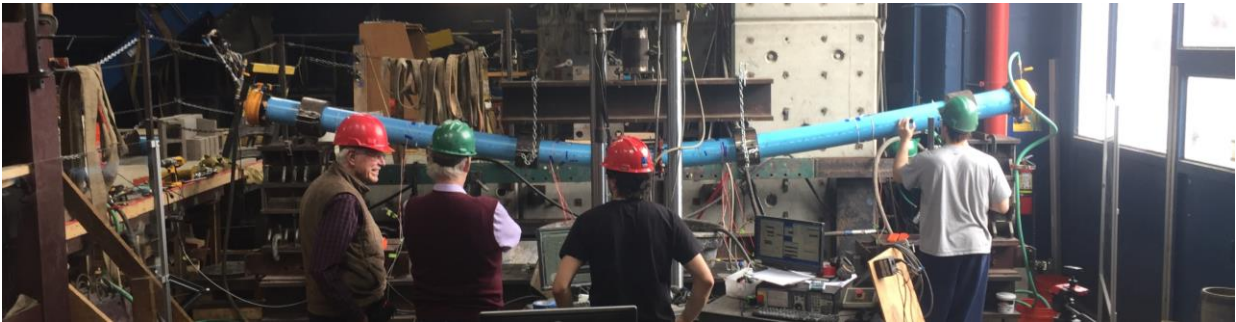
bottom of the restraint to experience tension. Inward rotation of the collars at the top of the restraint relieved the stress in the upper threaded rods. As vertical movement was imposed until maximum deflection, the spigot of the specimen experienced increasing amounts of ovaling, while the crown of the bell flattened to accommodate the applied load. Figure 5.15d shows flattening at the bell crown, local rotation of the bell with respect to the spigot, and inward collar rotation that caused the nuts on the upper threaded rods to lose contact with the collars.

5.5. Four-Point Bending Test Summary

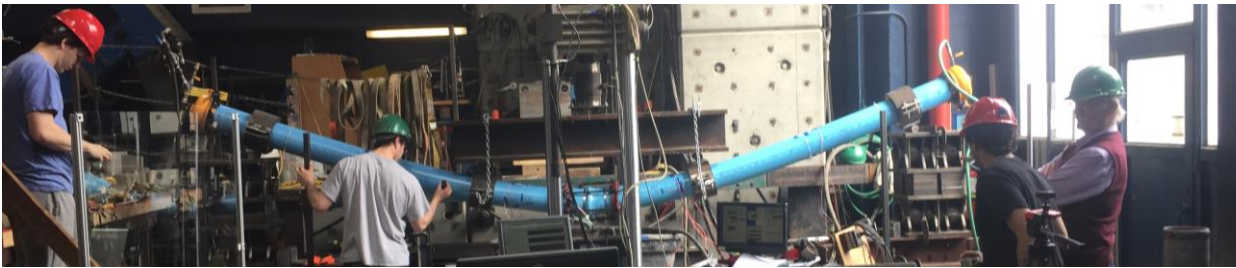
An 18 ft (5.5 m) specimen of iPVC pipe with a restrained bell and spigot joint was tested in four-point bending. The specimen was centered in the loading frame. The pipe was pressurized for the duration of the test at approximately 80 psi (550 kPa). Support and loading points were located 30 in. (0.76 m) and 60 in. (1.52 m) away from the specimen's centerline, respectively. An initial 2.9 in. (74 mm) of vertical displacement was due to the self weight of the pressurized pipe when supporting jacks under the specimen were manually removed. Loading was then applied through the downward movement of the loading frame's crosshead. Loading was continued until 22.2 in. (564 mm) of vertical displacement when servo-controlled loading was applied until the specimen



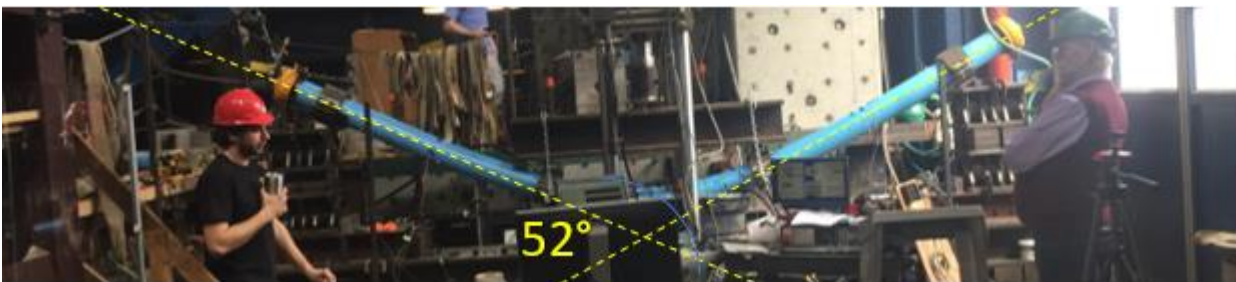
(a) Initial Position



(b) 10 in. (254 mm) of Displacement

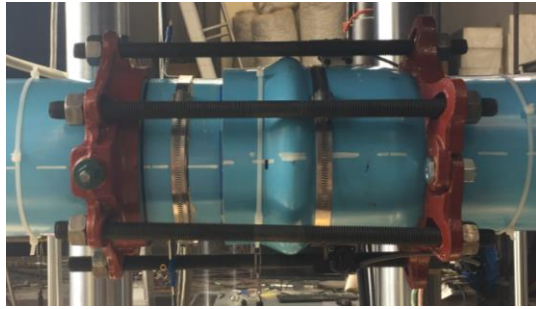


(c) 18.5 in. (470 mm) of Displacement



(d) 26.5 in. (673 mm) of Displacement (Maximum Displacement)

Figure 5.14. Testing Specimen at Four Levels of Displacement



(a) Restrained Joint at Initial Position



(b) Restrained Joint at 10 in. (254 mm.) of Displacement



(c) Restrained Joint at 18.5 in. (470 mm.) of Displacement



(d) Restrained Joint at Maximum Displacement

Figure 5.15. Restraining Joint at Four Levels of Displacement

reached a maximum deflection of 26.7 in. (678 mm). At this point, the geometric limit of the test frame was reached, the test was stopped, and the specimen was unloaded.

A maximum rotation of 52.2 degrees resulted in a max moment of 90.8 kip-in. (10.3 kN-m). The restrained joint of the specimen was able to withstand significant deformation, as shown by the photos and test measurements, without losing internal pressure at any time during the test.

Section 6

Axial Pull Tests

6.1. Introduction

The results of four axial pull tests are presented in this section. The tests were performed to evaluate the axial resistance between a nominal 6-in. (150-mm)-diameter iPVC pipe with a restrained joint and adjacent soil when buried. Four tests were conducted at three different soil burial depths to top of crown, including 30, 45, and 60 in. (760, 1140, and 1520 mm, respectively). All four tests were conducted using Star Pipe Product's Stargrip® Gen2 restraint mechanism as shown in Figure 1.1. This section describes the instrumentation, setup, testing procedure, and experimental results for all four axial pull tests.

6.2. Test Layout and Instrumentation

The four tests were completed using the north end of the Cornell large-scale split basin. A plan view of the test setup is shown in Figure 6.1. Three tests were performed, as shown, with the bell mouth facing north. One test was performed with the bell facing south to investigate the geometric effects of pulling the joint restraint in a different orientation. The total length of the joint specimen buried in soil was 147.5 in. (3750 mm), with a distance of 69.25 in. (1759 mm) from the north restraining collar to the north inside boundary of the split basin. The joint was set to open 1 in. (25.4 mm) before engagement of the joint restraint. This initial setup was achieved through careful measurements of the distances between the nuts on the restraining rods and the restraining collar to ensure uniformity in the axial movement at all six rod locations.

The objective of the tests was to assess the resistance of the joint, pipeline, and restraints to the relative axial movement between the specimen and adjacent soil. The geometry of the pipeline and restraining system, soil strength, and depth all contribute to the axial resistance between pipeline and soil. The tests were performed with no internal water pressure because it does not affect the axial resistance to pullout.

As shown in Figure 6.1, each specimen was gripped at the outside of the split basin with three Stargrip® Gen2 wedge action restraints in series and connected to an MTS servo-controlled hydraulic actuator mounted to the end of a rigid reaction frame. Load was applied through rods connected to the hydraulic actuator that was mounted to the frame. The actuator had a 22-kip (98-

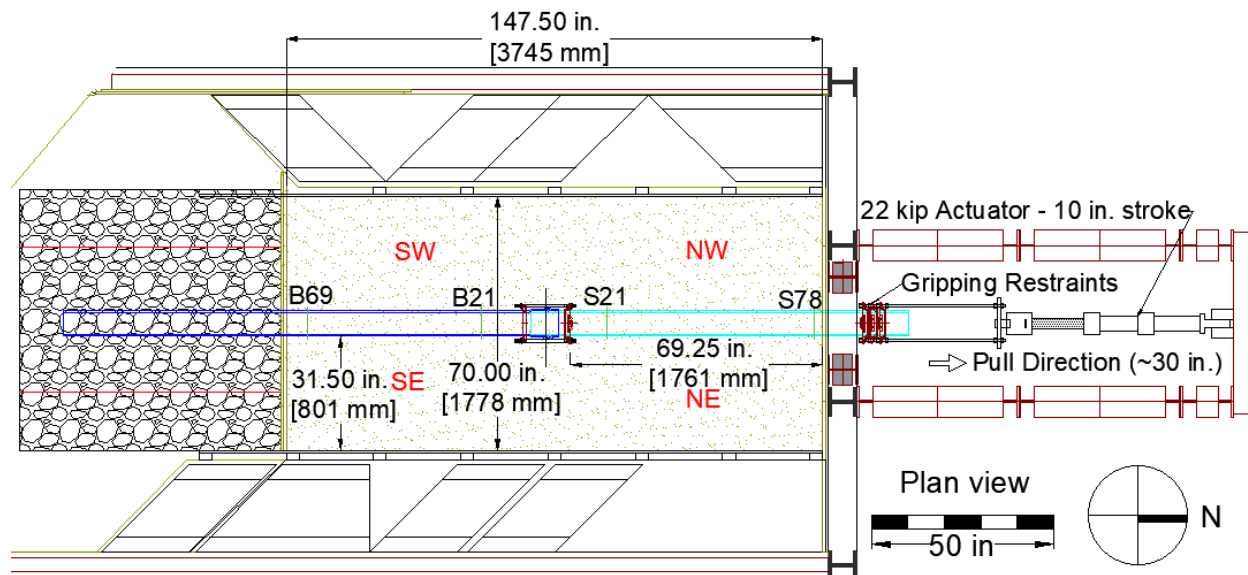


Figure 6.1 Plan View of Axial Pull Test Setup

kN) capacity and 10-in. (254-mm) stroke. Applied load was recorded through a load cell located between the pipe and actuator.

Table 6.1 provides a list of the instrumentation used for all four tests. Four strain gage planes were applied to each testing specimen at ± 21 in. (533.4 mm), +78 in. (1981 mm), and -69 in. (1753 mm) along the specimen's length with respect to the center of the joint. Two planes were located on the spigot (north) pipe and the bell (south) pipe for three of the four axial pull tests. The orientation was rotated by 180 degrees for the third of the four tests so that the bell mouth was facing south.

Data was recorded at a 2-Hz sampling rate throughout the tests. Load was applied at a rate of 1 in./min. (25 mm/min.). After the full 10 in. (254 mm) stroke of the actuator was applied, the system was briefly unloaded, and the actuator was moved south to its original starting position. Load was again applied through 10 in. (254 mm) of stroke. Three cycles of displacement were applied for approximately 30 in. (762 mm) of total axial movement.

Joint opening and pipe displacement were measured using horizontal string pots (HSPs). HSP_North was fixed to the to the north end of the split basin and was used to measure leading edge displacement of the north pipe as it was pulled though the soil. HSP_North_Grip was used to measure relative slip that occurred between the three gripping restraints at the north end of the pipe. HSP_Joint_Open was fixed to the inside of the specimen to monitor joint opening.

Table 6.1. Instrumentation List for iPVC Axial Pull Tests

Location	Instrument	Local Instrument Name
22 Kip. Actuator	Internal Actuator LVDT	MTS 22KIP DISP
South End of Actuator	55 kip. Load Cell	MTS_55KIP_LOAD
North End of Spigot	String Pot	HSP_North
Loading Restraints	String Pot	HSP_North_Grip
South Edge of Spigot	String Pot	HSP_Joint_Open
South End of Bell	String Pot	HSP_South
69 in. South of Bell Face	Crown, Axial Strain	B69C
69 in. South of Bell Face	Invert, Axial Strain	B69I
21 in. South of Bell Face	Crown, Axial Strain	B21C
21 in. South of Bell Face	Crown, Circumferential Strain	B21CC
21 in. South of Bell Face	East Springline, Axial Strain	B21E
21 in. South of Bell Face	West Springline, Axial Strain	B21W
21 in. South of Bell Face	Invert, Axial Strain	B21I
21 in. South of Bell Face	Invert, Circumferential Strain	B21IC
21 in. North of Spigot Face	Crown, Axial Strain	S21C
21 in. North of Spigot Face	Crown, Circumferential Strain	S21CC
21 in. North of Spigot Face	Invert, Axial Strain	S21I
21 in. North of Spigot Face	Invert, Circumferential Strain	S21IC
21 in. North of Spigot Face	East Springline, Axial Strain	S21E
21 in. North of Spigot Face	East, Circumferential Strain	S21EC
21 in. North of Spigot Face	West Springline, Axial Strain	S21W
21 in. North of Spigot Face	West, Circumferential Strain	S21WC
78 in. North of Spigot Face	Crown, Axial Strain	S78C
78 in. North of Spigot Face	Invert, Axial Strain	S78I

(1 in. = 25.4 mm)

HSP_South was mounted at the southern end of the bell and fixed to the floor of the test basin floor to measure trailing edge movement.

6.3. Soil Placement and Compaction

For each test a 13-in. (330-mm)-deep bed of compacted soil was placed on the test basin floor. The soil used at all depths in all tests was a washed, crushed, glacio-fluvial sand produced by RMS

Table 6.2. PT30 Compaction Data

Location	Dry Unit Weights (lb/ft ³)					Moisture Tin Water Content, w (%)				
	Lift 1	Lift 2	Lift 3	Lift 4	Lift 5	Lift 1	Lift 2	Lift 3	Lift 4	Lift 5
NW	109.6	107.5	107.8	107.9	108.2	1.5	4.0	3.1	6.6	5.1
NE	104.7	108.3	107.4	107.6	105.7	6.6	4.3	3.9	5.1	4.9
SW	108.3	105.7	107.9	105.4	105.8	3.3	6.2	5.0	7.7	5.7
SE	110.9	107.5	107.9	106.3	108.6	3.4	3.1	4.6	2.8	3.2
Average	108.4	107.3	107.8	106.8	107.1	3.7	4.4	4.2	5.5	4.7
Stdev	2.7	1.1	0.2	1.2	1.1	2.1	1.3	0.8	2.1	1.1
Global Average	107.5					4.5				
Global Stdev	1.5					1.5				

6.3.2. Axial Pull Test 2 (PT45): 45 in. Burial

Six lifts of soil were placed to reach the desired 45 in. (1143 mm) to top of pipe. Table 6.3 lists dry unit weights and moisture contents as well as averages and standard deviations for each lift.

Table 6.3. PT45 Compaction Data

Location	Dry Unit Weights (lb/ft ³) ^a						Moisture Tin Water Content, w (%)					
	Lift 1	Lift 2	Lift 3	Lift 4	Lift 5	Lift 6	Lift 1	Lift 2	Lift 3	Lift 4	Lift 5	Lift 6
NW	109.7	107.3	105.8	108.9	107.9	106.3	3.8	3.7	4.3	3.2	3.3	3.6
NE	109.4	106.6	108.7	105.8	105.6	106.4	3.3	3.3	3.7	4.1	3.7	4.0
SW	107.9	107.0	105.9	106.1	108.4	108.4	3.9	4.9	3.8	3.5	4.4	4.9
SE	109.1	107.8	107.2	105.7	105.0	107.9	4.1	3.2	3.3	3.7	3.4	3.9
Average	109.0	107.2	106.9	106.6	106.7	107.3	3.8	3.8	3.8	3.6	3.7	4.1
Stdev	0.8	0.5	1.4	1.5	1.7	1.1	0.3	0.8	0.4	0.4	0.5	0.6
Global Average	107.3						3.8					
Global Stdev	1.4						0.5					

6.3.3. Axial Pull Test 3 (PT45b): 45 in. Burial

The orientation of the testing specimen was reversed 180 degrees for the third axial pull test. The bell and spigot pipes were the north and south pipes, respectively. The split backup ring and wedge-action restraint were on the north and south sides of the restraint, respectively.

Six lifts of soil were placed to reach the desired 45 in. (1143 mm) to top of pipe. Table 6.4 lists dry unit weights and moisture contents as well as averages and standard deviations for each lift.

Table 6.4. PT45b Compaction Data

Location	Dry Unit Weights (lb/ft ³) ^a						Moisture Tin Water Content, w (%)					
	Lift 1	Lift 2	Lift 3	Lift 4	Lift 5	Lift 6	Lift 1	Lift 2	Lift 3	Lift 4	Lift 5	Lift 6
NW	107.2	106.5	107.5	104.5	108.2	108.8	5.3	3.9	4.7	6.8	4.8	5.3
NE	106.6	107.4	104.8	104.0	107.8	106.5	4.6	4.7	4.9	4.7	4.3	5.8
SW	107.9	107.5	105.7	106.7	106.3	106.5	4.3	4.6	6.9	5.8	5.0	6.1
SE	108.1	106.6	105.2	104.2	107.3	105.4	4.0	4.5	6.4	6.2	5.3	5.9
Average	107.4	107.0	105.8	104.8	107.4	106.8	4.5	4.4	5.7	5.9	4.9	5.8
Stdev	0.7	0.5	1.2	1.2	0.8	1.4	0.5	0.4	1.1	0.7	0.4	0.3
Global Average	106.6						5.2					
Global Stdev	1.3						0.9					

6.3.4. Axial Pull Test 4 (PT60): 60 in. Burial

Six lifts of soil were placed to reach 45 in. (1143 mm) of burial to top of pipe. Sheets of 0.75-in. (19-mm)-thick plywood were placed on top of this soil, followed by evenly distributed steel weights to simulate an additional 15 in. (380 mm) of soil coverage to obtain vertical stress on the pipe equivalent to 60 in. (1524 mm) of cover. Table 6.5 lists dry unit weights and moisture contents as well as averages and standard deviations for each lift.

Table 6.5. PT60 Compaction Data

Location	Dry Unit Weights (lb/ft ³) ^a						Moisture Tin Water Content, w (%)					
	Lift 1	Lift 2	Lift 3	Lift 4	Lift 5	Lift 6	Lift 1	Lift 2	Lift 3	Lift 4	Lift 5	Lift 6
NW	103.8	106.3	107.3	105.6	109.4	107.3	4.6	4.3	4.5	5.2	4.0	3.5
NE	105.9	108.2	105.8	107.1	107.7	108.0	4.9	3.7	4.1	4.8	4.1	4.0
SW	108.0	109.5	108.9	106.4	107.1	109.5	3.7	5.4	4.3	5.2	3.8	3.5
SE	107.4	109.2	106.8	104.1	105.9	108.5	3.0	4.0	4.2	5.7	4.0	4.3
Avg	106.3	108.3	107.2	105.8	107.5	108.3	4.0	4.3	4.3	5.3	4.0	3.8
Stdev	0.6	1.2	1.1	1.4	0.3	0.8	0.8	0.8	0.3	1.0	1.0	0.1
Global Avg	107.2						4.3					
Global Stdev	1.6						0.7					

6.4. Axial Pull Forces and Displacements

This section summarizes the displacements and axial pull forces that were measured in all four axial pull tests. The test specimen was oriented with the spigot as the northern pipe for Tests 1, 2, and 4 at burial depths to crown of 30, 45, and 60 in. (760, 1140, and 1520 mm), respectively. The wedge action restraint was the leading restraint for these three tests. Test 3 was performed in the opposite orientation. The bell section was the northern pipe, and the corresponding split backup ring was the leading restraint as described previously. The purpose of the reversed orientation was to understand the effects of the reversed locations of the restraining collars relative to the direction of pipe movement.

6.4.1. Interpretation of Measurements

Figure 6.1 shows the locations of the four strain gage planes. Plane S78 provides a measure of load that closely matches that measured by the actuator. As the specimen is pulled through the soil, planes S21 and B21 provide a measure of the axial force at the leading edge and trailing edge of the joint restraint, respectively. The difference in axial load between planes B21 and S21 is the load that is dropped across the restraint. This load drop increases the axial force mobilized in the pipeline, thus reducing the axial ground deformation the pipeline can accommodate before failure.

6.4.2. Axial Pull Test 1 (PT30): 30 in. Burial Results

Figure 6.3a provides a plot of the axial force measured at the load cell vs. the axial displacement of the pipe measured at the leading edge. Figure 6.3b shows the axial loads measured by the two northern strain planes (S78 and S21) and the force measured by the load cell versus the leading-edge displacement of the specimen. As stated previously, after 10 in. (254 mm) of actuator displacement, the test was unloaded, and the actuator was moved to its initial position to repeat the displacement cycle. Three successive cycles of displacement were applied.

There is close agreement between the load versus displacement plot for the load cell force and strain gage load at S78. The axial force measured at strain gage plane S78 is higher than that measured at S21 due to the friction mobilized during pullout between those two locations on the pipe. Thus, the difference in force measured at those two locations represents the frictional force that is developed along the spigot of the test specimen.

The force measured at the trailing edge of the joint from gage plane B21 was relatively low for all pull tests. For each test this load was approximately 0.5 kips (2.2 kN) ranging from 0.45 kips (2 kN) to 0.59 kips (2.62 kN). The force measured at 20 in. (510 mm) of displacement at the S21 gage plane was 5.7 kips (25.4 kN). This force corresponds to 0.3 kips (1.3 kN) measured at plane B21 at the same displacement on the opposite side of the joint. By subtracting these values, one obtains 5.4 kips (24 kN) of axial force dropped across the joint of the specimen which is only 5% lower than the force measured at S21. Therefore, the gage plane positioned directly north of the joint serves as a close approximation of the load dropped across the joint during the test.

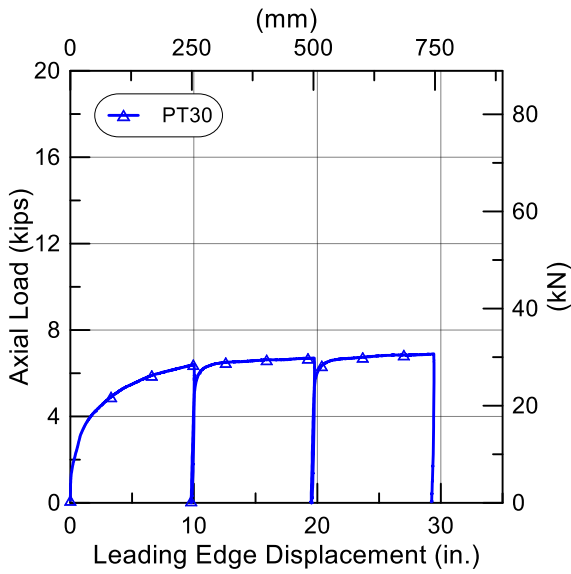
Figure 6.4 is a photo of the surface cracking that was observed after PT30. Such tensile cracking indicates that shear distortion and some volumetric expansion occurred and were transferred to the surface of the soil as the joint restraint was pulled through the soil. The surface cracking in PT30 was the most severe of all four pull tests.

As explained previously, the joint was set to allow 1 in. (25 mm) of joint opening before engagement of the restraint. The string pot measurements indicate that the joint opened a maximum of 0.61 in. (15.5 mm) during the test. Figure 6.5 shows a photo of the wedge action restraint after the test. It shows clearly that sand had lodged between the collar and retaining nuts which prevented the joint from opening the allotted 1 in. (25mm).

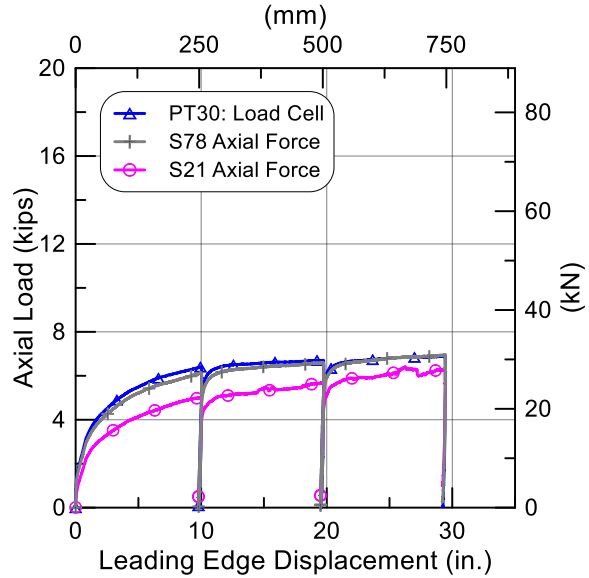
6.4.3. Axial Pull Test 2 (PT45): 45 in. Burial Results

Figure 6.6a shows a plot of the measured load cell force vs. axial displacement of the pipe measured at the leading edge. Figure 6.6b shows the axial loads measured by the load cell and by the strain gages at planes S78 and S21 vs. the leading-edge displacement of the pipe. Three cycles of displacement are plotted in the figure.

Again, there is very close agreement between the load vs. leading edge displacement plots for axial force measurements by the load cell and the northernmost strain gage plane, S78. Because of soil friction mobilized along the pipe, the axial force measured at S21 is lower than that measured at S78. The axial force measured in S21 provides a good estimation for the load dropped across the joint for the same reasons given in the discussion of Figure 6.3.



(a) Actuator Load Measurement



(b) Load Cell and Strain Gage Loads

Figure 6.3. PT30 Axial Load vs. Displacement for Actuator, Load Cell, and Strain Gage Loads

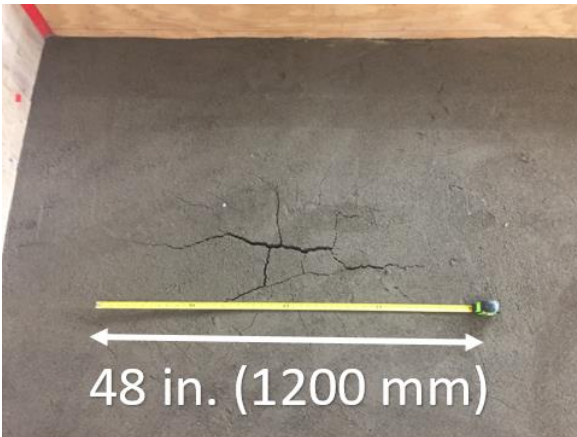


Figure 6.4. Soil Surface Cracking after PT30

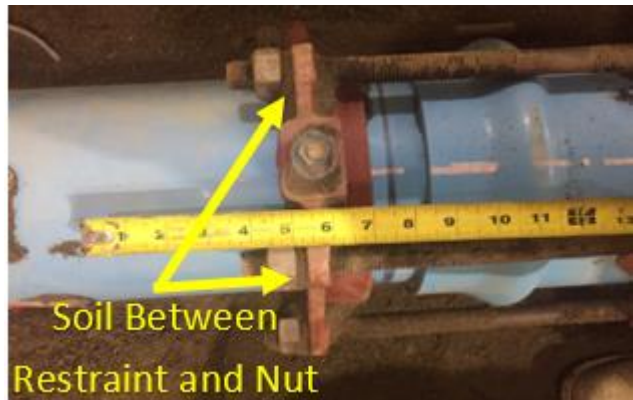
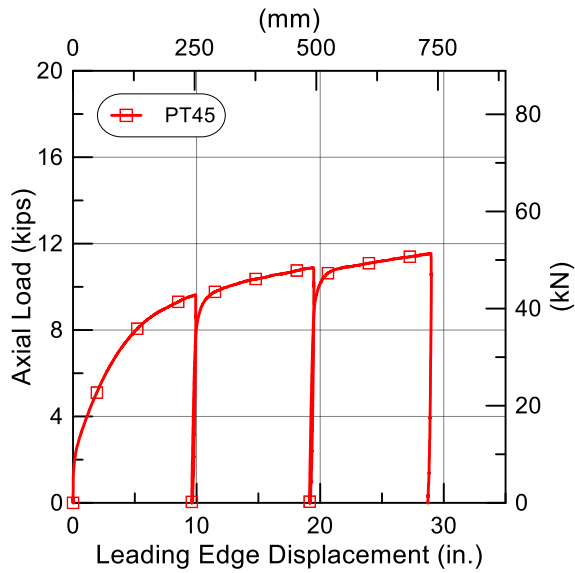
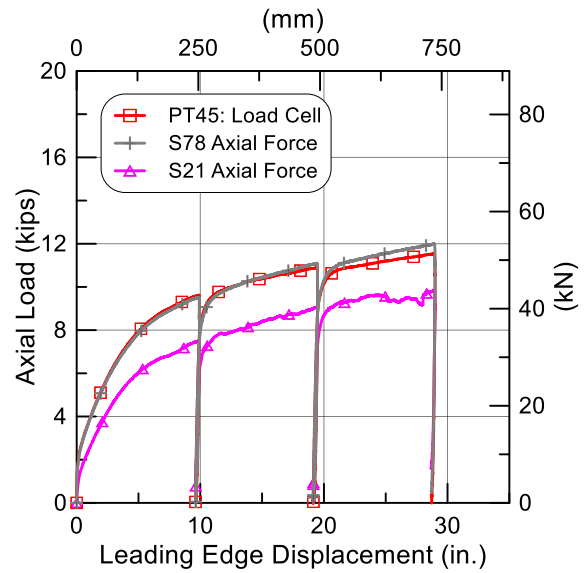


Figure 6.5. Photo of Sand Lodged Between Nuts and Collar of the Joint Restraint

Surface cracks again appeared during the test as shown in Figure 6.7. The cracking was less severe when compared to PT30, and reflects the shear distortion and volumetric expansion that is created as the restraint and pipe are pulled through the soil. The greater depth of soil cover results in less extensive surface cracks.



(a) Actuator Load Measurement



(b) Load Cell and Strain Gage Loads

Figure 6.6. PT45 Axial Load vs. Displacement for Actuator, Load Cell, and Strain Gage Loads

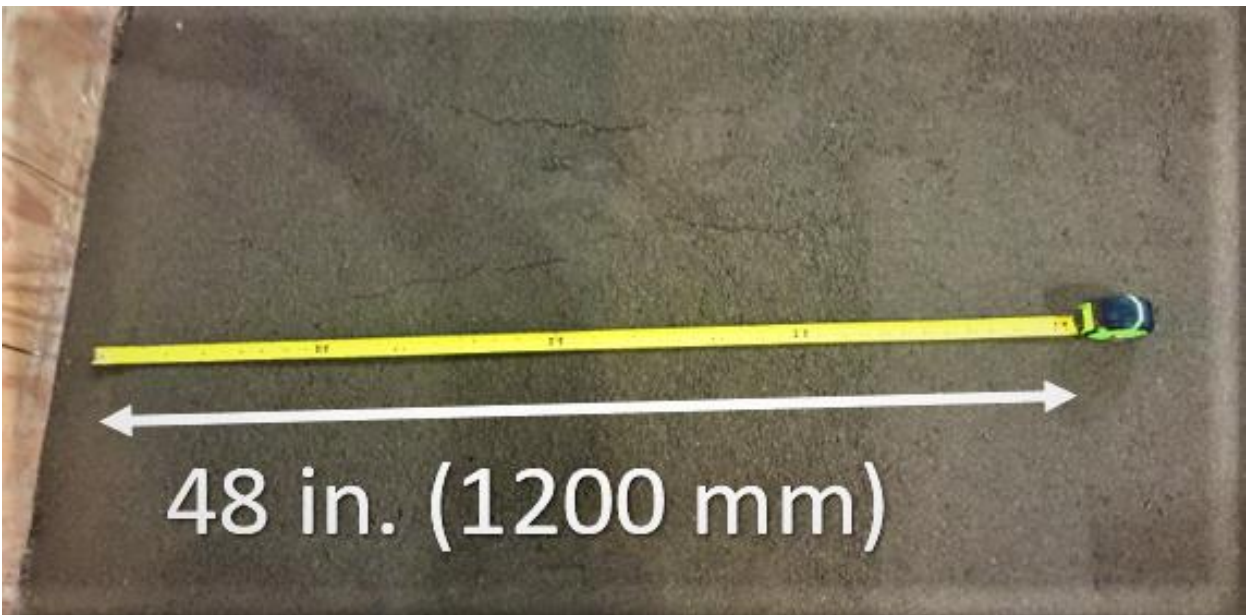


Figure 6.7. Soil Surface Cracking After PT45

The string pot measurements indicate that the joint opened a maximum 0.62 in. (15.8 mm) during the test. The joint was set to allow a maximum opening of 1 in. (25 mm). Like the first pull test, sand was observed again between the restraining collar and nuts, similar to what is shown in Figure 6.5.

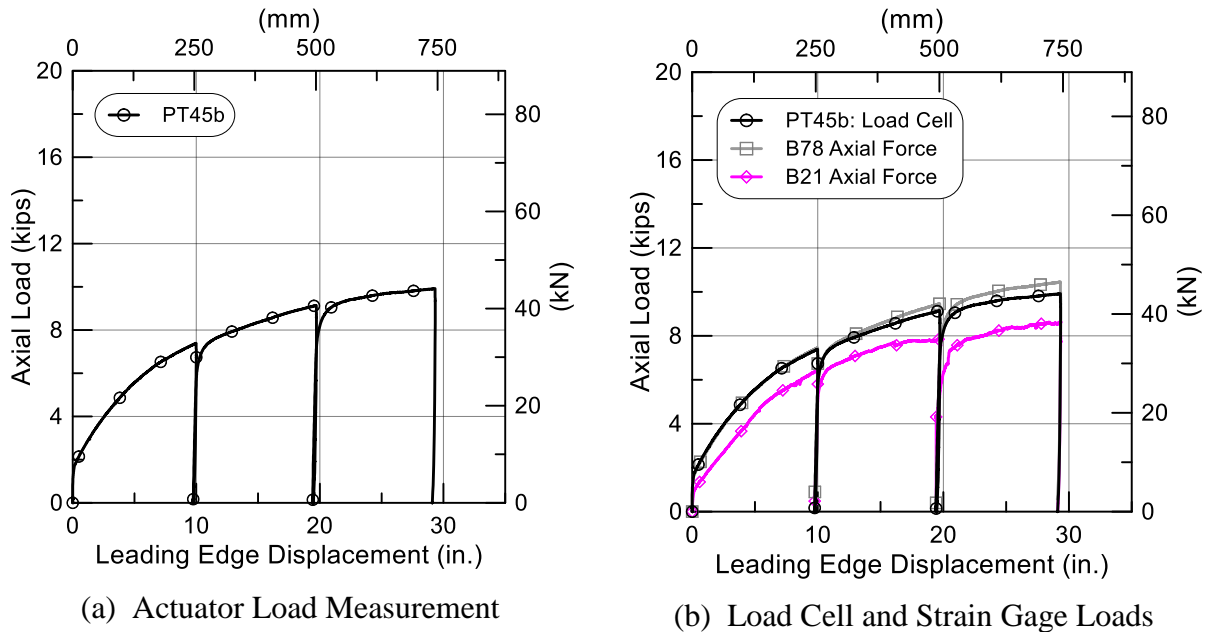


Figure 6.8. PT45b Axial Load vs. Displacement for Actuator, Load Cell, and Strain Gage Loads

6.4.4. Axial Pull Test 3 (PT45b): 45 in. Burial Results

The soil depth for PT45 was the same as for PT45b. The orientation was reversed 180 degrees from that of the other pull tests. The bell pipe was now north of the joint center with the split backup ring positioned on the north side of the joint. Figure 6.8 shows the axial load versus the leading-edge displacement plots that are similar to the plots that have been discussed for PT30 and PT45. The loads measured in PT45b were lower than those measured in PT45 despite being conducted at the same depth of soil cover in similar soil conditions. The lower axial pull force is related to the smaller dimension of the split backup ring which was the northern restraint for PT45b. The forces mobilized in PT45b are about 10% less than those measured in PT45 at the same depth. The surface cracking for PT45b was similar to that observed in PT45.

The string pot measurements indicate that the joint opened a maximum 0.25 in. (6.35mm) during the test. The joint was set to allow a maximum opening of 1 in. (25mm). Like the other pull tests, sand was observed again between the restraining collar and nuts.

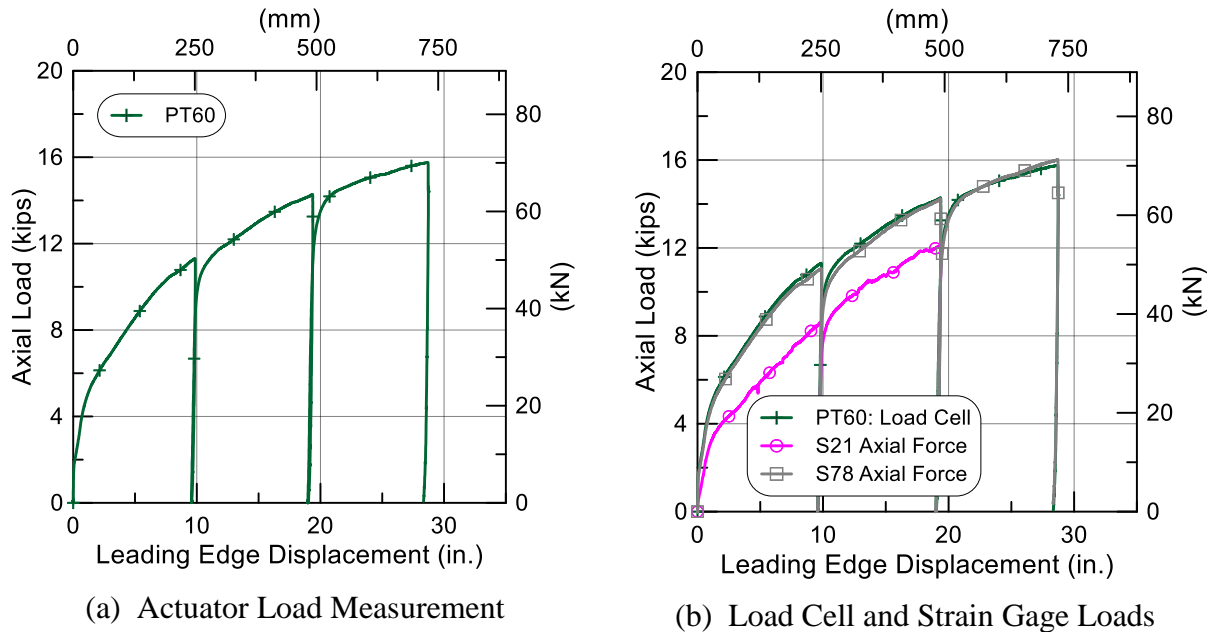


Figure 6.9. PT60 Axial Load vs. Displacement for Actuator, Load Cell, and Strain Gage Loads

6.4.5 Axial Pull Test 4 (PT60): 60 in. Burial Results

For the fourth pull test, plywood sheets were placed on the soil surface and loaded with steel weights to simulate an extra 15 in. (570 mm) of soil cover to yield the vertical stress equivalent to a desired 60-in. (1520-mm) burial depth. The specimen was pulled approximately 30 in. (762 mm) in three separate cycles. The axial load vs. leading edge displacement is shown in Figure 6.9. As expected, the maximum force was measured in PT60. Visual inspection of surface cracks was not possible following PT60 due to the plywood sheets and weights that covered the soil surface.

The string pot measurements indicate that the joint opened a maximum 0.64 in. (16.3 mm) during the test. The joint was set to allow a maximum opening of 1 in. (25.4 mm). Like the other pull tests, sand was observed again between the restraining collar and nuts.

There is close agreement between the axial force measured by the load cell and that measured by strain gages at S78. For the first two cycles of axial displacement, the axial force measured at strain gage location S21 is lower than that measured at S78 due to friction mobilized along the specimen between the two locations. The strain gages at S21 at the beginning of the third pull were damaged by interaction with the soil and, after about 20 in. (508 mm) of displacement, are not shown. As

explained previously, the load measured at S21 provide a close estimate of the load dropped across the joint.

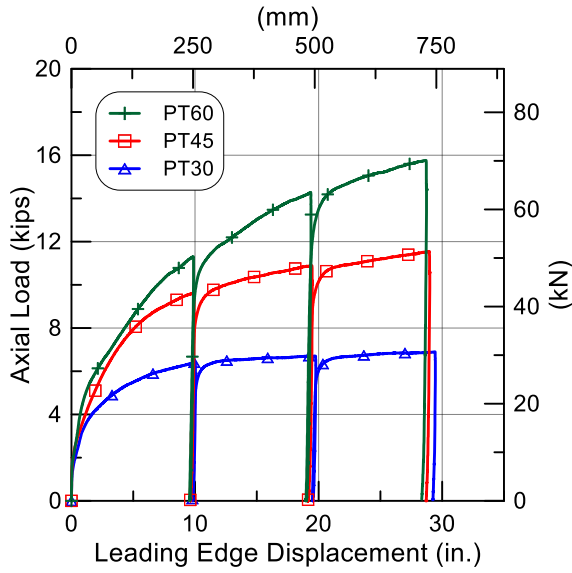
6.5. Comparison of Axial Load vs Displacement Performance

Figure 6.10 provides the axial load vs. displacement for all four axial pull tests. Figure 6.10a and b show the load measured at the actuator and strain gage plane S21, respectively, plotted with respect to leading edge displacement for the three tests with the same pipeline orientation. As previously discussed, the axial load measured at strain gage location S21 (north side of restraint) provides a good estimate of the load dropped across the joint restraint for each test. The load measured at B21 (south side of restraint) was relatively small for each test at approximately 0.5 kips (2.2 kN). Figure 6.10b provides for a direct comparison of the load dropped across each joint vs. leading edge displacement for increasing burial depths.

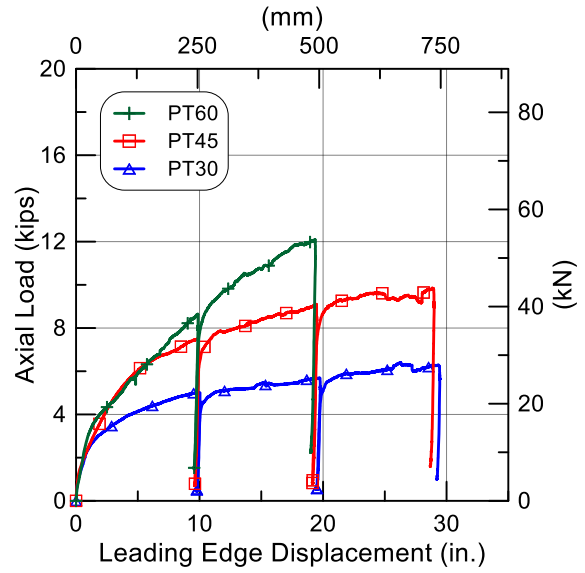
Figure 6.10c and d allow for a comparison of the tests (PT45 and PT45b) performed at the 45-in. (1140-mm) burial depth. The plots show the actuator load and load measured on the north side of the restraint versus leading edge displacement, respectively, for a pipeline joint orientation that was reversed from the one used in PT30, 45, and 60.

These figures allow for comparison of the axial resistance to pull out at two different orientations of the restraining clamps. In PT45 the spigot and wedge action restraint was on the northside of the joint. In PT45b involved the bell and split backup ring was on the northside of the joint. Figure 6.10d shows the load drop across the joints with opposite orientation vs. axial displacement between the restrained joint and soil. This load was calculated using the strain recorded at gage planes S21 (PT45) and B21 (PT45b), respectively. The smaller transverse area of the split backup ring in contact with the soil generates roughly 10% less force than that of the larger wedge action restraint.

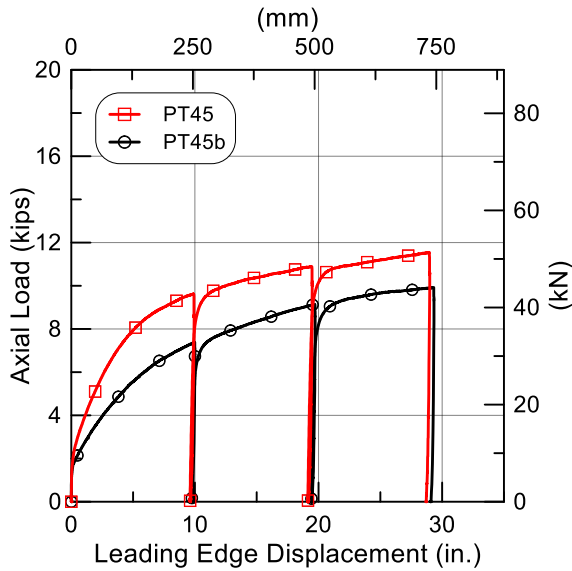
The loads at the strain gage planes just north of the restraints of all four pull tests at 18 in. (460 mm) of axial displacement are plotted in Figure 6.11 vs. depth to the centerline of the pipe. The loads at these locations are approximately the same as the loads dropped across the joint restraints. A linear regression was fit to the data from all tests assuming zero force at zero depth. An $r^2=0.979$ shows that the linear trend is statistically robust relative to the database. The linear trend shows



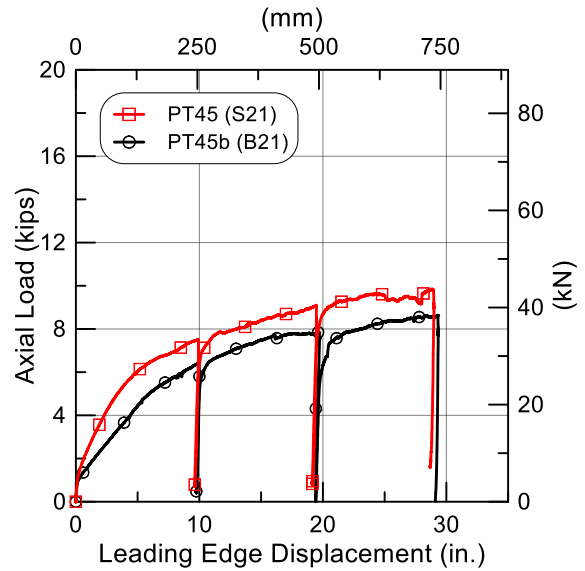
a) Load vs. Leading Edge Displacement for PT30, PT45 and PT60



b) S21 Load vs. Leading Edge Displacement for PT30, PT45 and PT60



c) Load vs. Leading Edge Displacement for PT45 and PT45b



d) S21 and B21 Loads vs. Leading Edge Displacement for PT45 and PT45b

Figure 6.10. Comparison Plots for Axial Pull Tests

that axial load drop is directly proportional to depth for similar soil and provides a basis for predicting the force against vs. displacement of restrained iPVC joints at different burial depths.

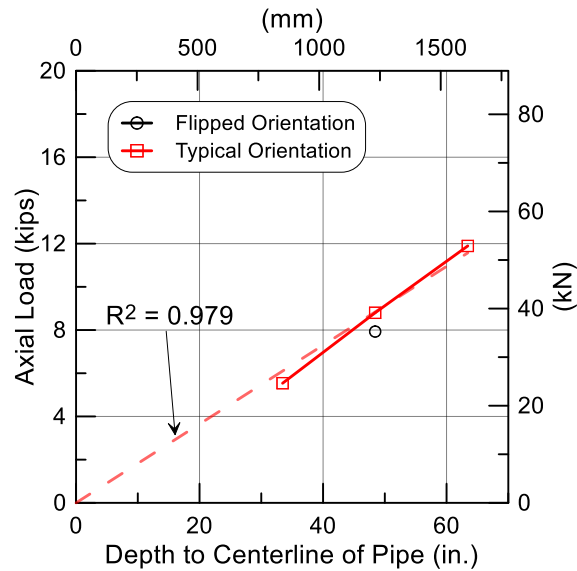


Figure 6.11. Axial Load vs. Depth to Centerline of Pipe

6.6. Axial Pull Tests Summary

Axial pull tests were completed at three different soil depths to pipe crown of 30, 45, and 60 in. (760, 1140, and 1520 mm, respectively). One test was performed at each depth with the spigot and wedge action restraint on the north side of the specimen. One test was performed at the 45 in. (1140 mm) burial depth under a reversed orientation, where the split backup ring and bell were on the north side of the setup. Each pipe specimen was pulled approximately 30 in. (760 mm.) through the soil.

The axial force vs. displacement plots are presented and compared for all the tests. These plots include the force measured by a load cell at the leading edge of movement outside the north side of the test basin, as well as the force measured at the strain gage plane nearest the north side of the joint restraint versus leading edge displacement. The plots that show the load measured at the strain plane nearest the north side of the joint restraint provide a good approximation of the load dropped across the joint during the test. The successively higher loads dropped at increasingly deeper burial depths are shown clearly in the plots. The axial force increases with relative displacement between the pipe and soil. It also increases linearly with soil depth.

In each axial pull test the joint was set to allow 1 in. (25.4 mm) of joint opening before engagement of the restraint. This setting allowed joint opening in soil that varied from about 0.60 in. (15.2 mm) for PT30, PT45 and PT60 to 0.25 in. (6.4 mm) for PT45b, leaving between 0.40 in. (10.2 mm) and 0.75 in. (19.1 mm) of axial slip that could not be realized. Opening less than 1 in. (25.4 mm) was related to sand that lodged between the restraining collar and locking nuts, thereby resisting full axial displacement of the rods through the restraining collar. Similar axial pull tests performed on 6-in. (150-mm) PVC pipe with restrained joints (Wham et al., 2017) resulted in approximately 0.35 in. (8.9 mm) to 0.50 in. (12.7 mm) of axial slip that could not be realized because of sand lodged between the restraining collar and locking nuts.

Section 7

Fault Rupture Simulation

7.1. Introduction

This section presents the results of a full-scale fault rupture test performed on a 6-in. (150-mm)-diameter iPVC with two restrained joints. The test was performed in the large-scale test basin at the Cornell University Large Scale Lifelines Testing Facility on June 19, 2018.

7.2. Experimental Setup

A plan view of the test is shown in Figure 7.1. The layout shows the fault rupture plane's orientation with respect to the test specimen, as well as the approximate location of the four actuators generating basin movement. The intersection angle between the fault and pipe was set at 50°. The pipeline consisted of three sections of iPVC pipe with two restrained joints placed equidistant from the fault. A 20-ft-(6.1-m)-long center section of pipe was placed with its midpoint at the fault. The abrupt ground movement during the test was representative of a left-lateral strike-slip fault rupture as well as the most severe ground deformation that occurs along the margins of liquefaction-induced lateral spreads and landslides. The objective of the test was to evaluate the pipeline's ability to accommodate fault movement through axial extension and deflection of the pipe body and joints.

The pipeline was buried in the large-scale test basin at Cornell University in partially saturated sand, which was compacted to have an average friction angle of 42 degrees, equivalent in strength to that of dense granular backfill. The 6.9-in. (175-mm) outer-diameter pipe was placed on a bed of soil with 13-in. (330-mm) thickness at the bottom of the test basin. The depth of burial to the top of pipe was 32 in. (800 mm), resulting in 52 in. (1320 mm) of total soil depth. During the test, the southern section of the basin remained stationary while the north end was displaced to the north and west by four large-stroke actuators to cause soil rupture and slip at the interface between the two parts of the test basin.

A total pipeline length of 34.4 ft (10.5 m) was buried in soil between wooden retaining walls, which were located near the ends of the pipeline to allow access to instruments and end restraints. The total pipeline length from the north to south walls of the test basin was 40.3 ft (12.3 m). The ends of the pipe were fixed to each end of the split basin.

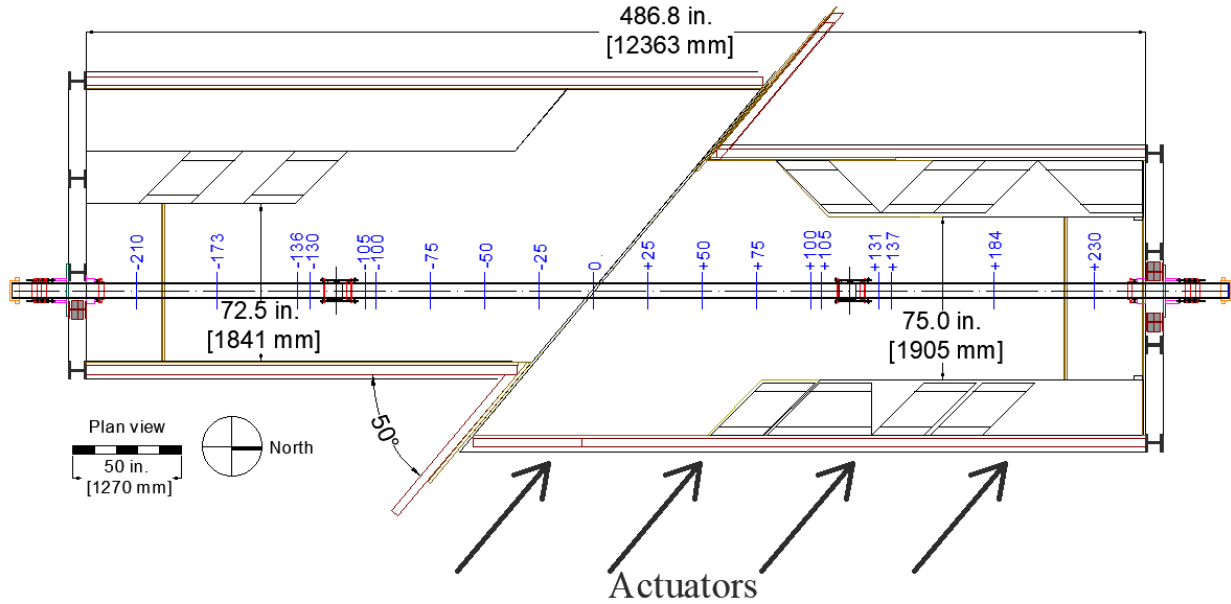


Figure 7.1. Plan View of Split Basin Testing Setup

The pipe was pressurized with water to approximately 80 psi (552 kPa) for the test. The north (movable) portion of the test basin was connected to four MTS hydraulic actuators with load cells controlled by an MTS Flextest GT controller. All actuators were operated in synchronized displacement control. The test configuration allows the actuators to displace the north half of the test basin a maximum of 43.5 in. (1105 mm) with a combined force of 510 kips (2270 kN).

7.2.1. Test Procedure

Once the specimen was instrumented, it was placed in the split basin. When soil placement was completed, and the pipe was filled with water. The test began by starting the data acquisition system followed by the servo-controlled hydraulic system of the MTS actuators. Internal water pressure was applied at approximately 80 psi (552 kPa). Displacement was applied to the northern section of the split basin at a rate of 2 in. (55 mm) per minute until failure of the specimen. Failure was identified as the inability to maintain internal water pressure.

7.2.2. Instrumentation

The test specimen response was monitored by 126 instruments during the test. The instrumentation included strain gages applied at several locations along the pipe, four load cells positioned at either

end of the pipeline, as well as digital pressure transducers to measure internal water pressure of the specimen. Actuator forces and displacements were recorded in addition to measurements of the relative movement between the north and south sections of the test basin.

Strain gages were applied at select locations along the specimen's length. There were 96 strain gages applied to the specimen at 19 different plane locations. Figure 7.1 shows these locations along the specimen. Each strain gage plane is identified by its distance from the fault line. A positive (+) designation indicates a plane on the north half of the specimen, while a negative (-) designation indicates a plane on the southern half of the specimen. All planes are approximately symmetric about the center of the specimen at the fault. Table 7.1 provides a list of each strain gage location along the specimen with its orientation [axial (A) or circumferential (C)] as well as its position [crown (C), invert (I), or east (E) or west (W) springline]. Strain gage plane locations were chosen on the basis of the expected pipeline deformation, which was estimated by finite element simulation in combination with the results of the axial tension and four-point bending test results.

Four calibrated load cells were positioned at each end of the test basin to measure axial load. Table 7.2 provides the locations and the labeling of the load cells. Three string potentiometers (string pots) were installed at each joint to measure pullout displacement and rotation. The string pot measurement system was protected by a joint shield composed of sheet metal that enclosed the joint. Figure 7.2 shows photos of the joint instrumentation and the protective metal enclosure.

7.2.3. Soil Preparation and Compaction Data

The soil used during the iPVC large-scale fault rupture test was the same crushed, washed, glacio-fluvial sand produced by RMS Gravel as discussed in Section 6.2. Figure 6.2 offers the grain size distribution of this material. The target value of moisture content was $w = 4.0\%$, and the dry density target was $\gamma_{dry} = 106 \text{ lb/ft}^3$ (16.7 kN/m^3). These values correspond to an angle of shearing resistance of approximately 42 degrees.

Table 7.1. PPI Split Basin Strain Gage List

Location	Instrument Description	Local Instrument Name
210 in. South of FL*	East, Axial Strain	SG-210EA
	West, Axial Strain	SG-210WA
173 in. South of FL	Crown, Axial Strain	SG-173CA
	Invert, Axial Strain	SG-173A
	East, Axial Strain	SG-173EA
	West, Axial Strain	SG-173WA
136 in. South of FL	Crown, Axial Strain	SG-136CA
	Invert, Axial Strain	SG-136A
	East, Axial Strain	SG-136EA
	West, Axial Strain	SG-136WA
130 in. South of FL	Crown, Axial Strain	SG-130CA
	Invert, Axial Strain	SG-130IA
	East, Axial Strain	SG-130EA
	East, Circumferential Strain	SG-130EC
	West, Axial Strain	SG-130WA
	West, Circumferential Strain	SG-130WC
105 in. South of FL	Crown, Axial Strain	SG-105CA
	Crown, Circumferential Strain	SG-105CC
	Invert, Axial Strain	SG-105IA
	Invert, Circumferential Strain	SG-105IC
	East, Axial Strain	SG-105EA
	East, Circumferential Strain	SG-105EC
	West, Axial Strain	SG-105WA
	West, Circumferential Strain	SG-105WC
100 in. South of FL	Crown, Axial Strain	SG-100CA
	Invert, Axial Strain	SG-100IA
	East, Axial Strain	SG-100EA
	West, Axial Strain	SG-100WA
75 in. South of FL	Crown, Axial Strain	SG-75CA
	Invert, Axial Strain	SG-75IA
	East, Axial Strain	SG-75EA
	West, Axial Strain	SG-75WA
50 in. South of FL	Crown, Axial Strain	SG-50CA
	Invert, Axial Strain	SG-50IA
	East, Axial Strain	SG-50EA
	East, Circumferential Strain	SG-50EC

Table 7.1. PPI Split Basin Strain Gage List (continued)

Location	Instrument Description	Local Instrument Name
50 in. South of FL	West, Axial Strain	SG-50WA
	West, Circumferential Strain	SG-50WC
25 in. South of FL	Crown, Axial Strain	SG-25CA
	Invert, Axial Strain	SG-25IA
	East, Axial Strain	SG-25EA
	East, Circumferential Strain	SG-25EC
	West, Axial Strain	SG-25WA
	West, Circumferential Strain	SG-25WC
At FL	Crown, Axial Strain	SG0CA
	Crown, Circumferential Strain	SG0CC
	Invert, Axial Strain	SG0IA
	Invert, Circumferential Strain	SG0IC
	East, Axial Strain	SG0EA
	East, Circumferential Strain	SG0EC
	West, Axial Strain	SG0WA
	West, Circumferential Strain	SG0WC
25 in. North of FL	Crown, Axial Strain	SG+25CA
	Invert, Axial Strain	SG+25IA
	East, Axial Strain	SG+25EA
	East, Circumferential Strain	SG+25EC
	West, Axial Strain	SG+25WA
	West, Circumferential Strain	SG+25WC
50 in. North of FL	Crown, Axial Strain	SG+50CA
	Invert, Axial Strain	SG+50IA
	East, Axial Strain	SG+50EA
	East, Circumferential Strain	SG+50EC
	West, Axial Strain	SG+50WA
	West, Circumferential Strain	SG+50WC
75 in. North of FL	Crown, Axial Strain	SG+75CA
	Invert, Axial Strain	SG+75IA
	East, Axial Strain	SG+75EA
	West, Axial Strain	SG+75WA
100 in. North of FL	Crown, Axial Strain	SG+100CA
	Invert, Axial Strain	SG+100IA
	East, Axial Strain	SG+100EA
	West, Axial Strain	SG+100WA

Table 7.1 PPI Split Basin Strain Gage List (completed)

Location	Instrument Description	Local Instrument Name
105 in. North of FL	Crown, Axial Strain	SG+105CA
	Crown, Circumferential Strain	SG+105CC
	Invert, Axial Strain	SG+105IA
	Invert, Circumferential Strain	SG+105IC
	East, Axial Strain	SG+105EA
	East, Circumferential Strain	SG+105EC
	West, Axial Strain	SG+105WA
	West, Circumferential Strain	SG+105WC
131 in. North of FL	Crown, Axial Strain	SG+131CA
	Invert, Axial Strain	SG+131IA
	East, Axial Strain	SG+131EA
	East, Circumferential Strain	SG+131EC
	West, Axial Strain	SG+131WA
	West, Circumferential Strain	SG+131WC
137 in. North of FL	Crown, Axial Strain	SG+137CA
	Invert, Axial Strain	SG+137IA
	East, Axial Strain	SG+137EA
	West, Axial Strain	SG+137WA
184 in. North of FL	Crown, Axial Strain	SG+184CA
	Invert, Axial Strain	SG+184IA
	East, Axial Strain	SG+184EA
	West, Axial Strain	SG+184WA
230 in. North of FL	East, Axial Strain	SG+230EA
	West, Axial Strain	SG+230WA

*FL- Fault Location

Table 7.2. PPI Split Basin Load Cell and Pressure Sensor List

End	Side	Instrument Description	Local Instrument Name
South	SE	Load Cell	LC1-6in-1K
	SW	Load Cell	LC2-6in-1K
	NE	Load Cell	LC3-6in-1K
	NW	Load Cell	LC4-6in-1K
		Pressure Sensor	Pressure Sensor 1
North	NE	Load Cell	LC5-6in-1K
	NW	Load Cell	LC6-6in-1K
	SE	Load Cell	LC7-6in-1K
	SW	Load Cell	LC8-6in-1K
		Pressure Sensor	Pressure Sensor 2

Table 7.3. PPI Split Basin Displacement Instrumentation List

Location	Instrument Description	Instrument Name
South Joint Crown	String Pot	SP_S_CROWN
South Joint East	String Pot	SP_S_EAST
South Joint Invert	String Pot	SP_S_INVERT
South Joint West	String Pot	SP_S_WEST
North Joint Crown	String Pot	SP_N_CROWN
North Joint East	String Pot	SP_N_EAST
North Joint Invert	String Pot	SP_N_INVERT
North Joint West	String Pot	SP_N_WEST
South Slip	String Pot	SP_SS
North Slip	String Pot	SP_NS
East Fault	East Fault Displacement	DISP_E_FAULT
West Fault	West Fault Displacement	DISP_W_FAULT

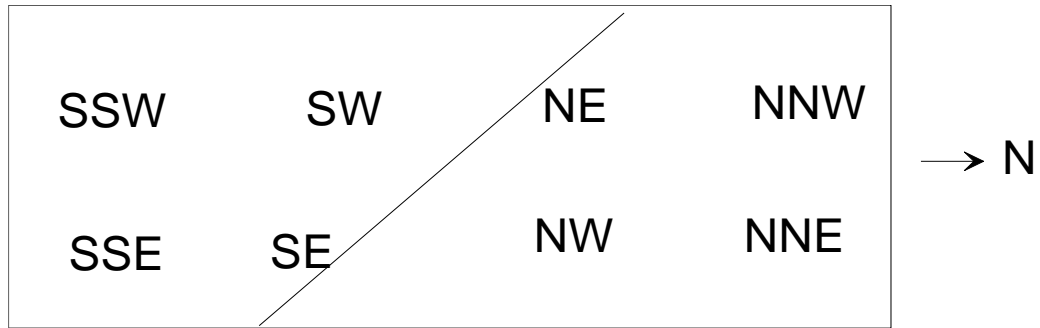


Figure 7.3 Plan View of Compaction Measurement Locations

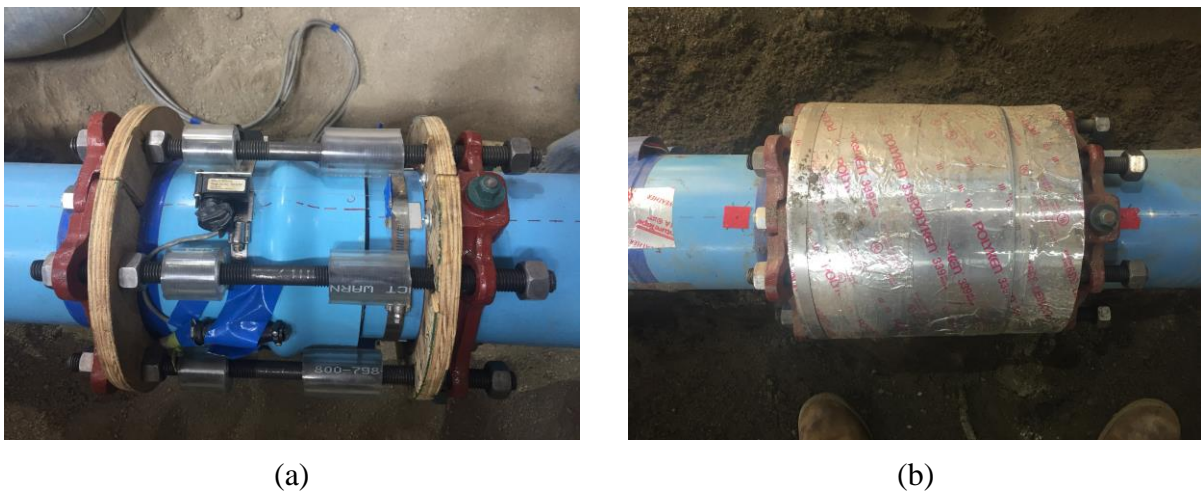


Figure 7.2. Instrumentation at (a) Restrained Joint and (b) Protective Enclosure

Eight measurements of dry unit weight and moisture content were taken for each 8 in. (203 mm) deep compacted soil lift. Figure 7.3 shows the approximate locations of the measurements. There were four measurement positions in the north portion of the test basin and four in the south section for each soil lift. Table 7.4 lists the dry unit weights, and Table 7.5 provides the moisture contents. The global average dry unit weight was 106.5 lb/ft^3 (16.7 kN/m^3) with a standard deviation of 2.1 lb/ft^3 (0.3 kN/ m^3). Table 7.5 provides the moisture content measurements. The global moisture content was 4.3% with a standard deviation of 0.6%.

7.3. Split Basin Test Results

Measurements obtained during the fault rupture test are summarized and described under the subheadings that follow.

Table 7.4. PPI Split Basin Test Soil Dry Unit Weights

	Dry Unit Weights (lb/ft ³)				
Location	Lift 1	Lift 2	Lift 3	Lift 4	Lift 5
NNW	106.4	107.3	108.8	106.8	105.1
NW	105.7	107.2	107.6	105.2	106.2
SSW	109.6	107.5	105.3	105.4	106.6
SW	105.9	110.0	106.9	109.0	106.1
SE	107.0	108.9	107.0	106.0	106.9
SSE	106.0	104.0	107.2	106.3	105.9
NE	107.9	109.6	108.6	110.6	105.8
NNE	100.5	103.0	104.8	104.1	101.0
Average	106.1	107.2	107.0	106.7	105.5
Stdev	2.6	2.5	1.4	2.2	1.9
Global Average					106.5
Global Stdev					2.1

$$1 \text{ (lb/ft}^3\text{)} = 0.1571 \text{ kN/m}^3$$

Table 7.5. PPI Split Basin Test Soil Water Content Data from Moisture Tins

	Moisture Tin Water Content, w (%)				
Location	Lift 1	Lift 2	Lift 3	Lift 4	Lift 5
NNW	4.2	3.4	3.3	4.5	4.4
NW	3.7	4.2	5.0	3.7	5.1
SSW	5.1	4.4	4.1	4.1	4.2
SW	4.2	3.4	4.6	4.2	4.8
SE	3.9	3.3	4.8	4.4	5.4
SSE	5.0	5.3	4.3	4.2	4.5
NE	4.1	4.3	5.3	4.4	5.3
NNE	5.3	4.4	3.7	3.1	4.2
Average	4.44	4.08	4.37	4.08	4.73
Stdev	0.60	0.70	0.66	0.47	0.49
Global Average					4.34
Global Stdev.					0.58

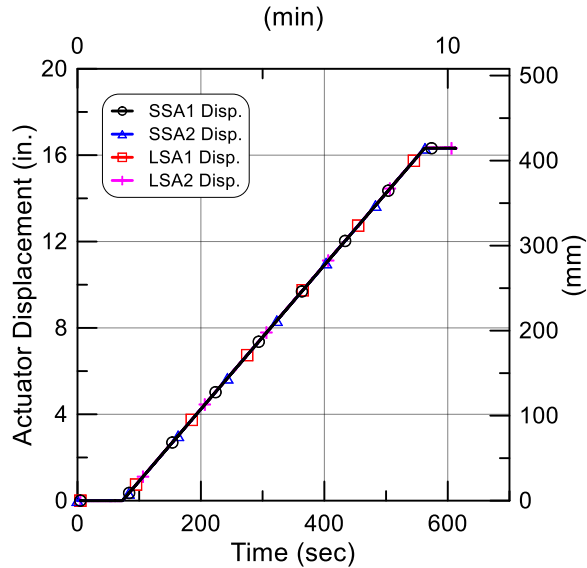


Figure 7.4. Actuator Displacement vs. Time

7.3.1. Test Basin Movements

The split basin setup includes four actuators that displace the north (moveable) section of the box a maximum of 43.5 in. (1.1 m) during the fault rupture test. All four actuators connect to a reaction wall at the northern section of the split basin. Long-stroke actuators 1 (LSA1) and 2 (LSA2) are the two northernmost actuators. Each LSA has a load capacity of 110 kips (489 kN) in compression and 63 kips (280 kN) in tension with a stroke of 6 ft (1.83 m). Short-stroke actuators 1 (SSA1) 2 (SSA2) are the two southernmost actuators. Each SSA has a load capacity of 145 kips (645 kN) in compression and 100 kips (445 kN) in tension with a stroke of 4 ft (1.22 m).

Figure 7.4 shows the displacement of the four actuators, the average of which is the fault displacement, with respect to time. Since the servo-controlled actuators move in unison under displacement control, all recorded displacements are identical.

7.3.2. Internal Water Pressure

The test specimen was pressurized with internal water pressure of approximately 80 psi (552 kPa) through the duration of the test until failure of the pipeline. The internal pressure vs. fault displacement is shown in Figure 7.5. Water was able to flow into the test pipeline during elongation of the pipe caused by fault movement. Relatively small fluctuations in internal pressure occurred during elongation of the pipeline in response to fault rupture. Once pressure was applied at the

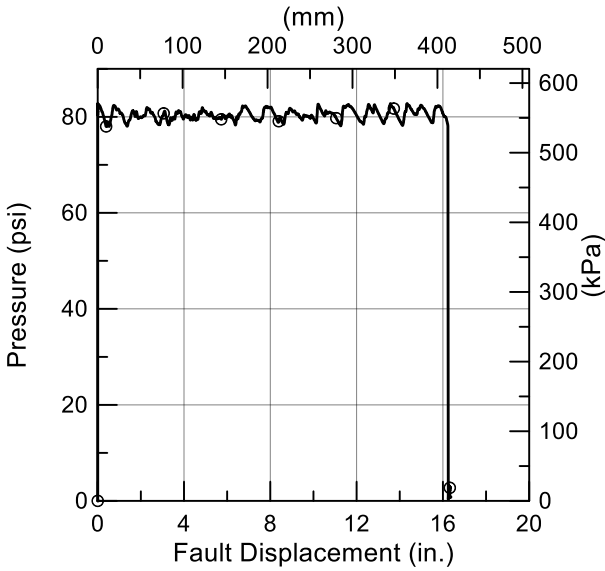


Figure 7.5. Internal Water Pressure vs. Fault Displacement

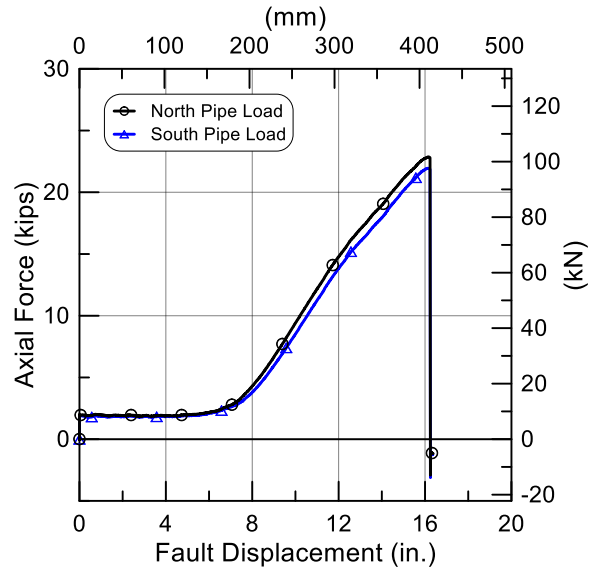


Figure 7.6. North and South Pipe End Loads vs. Fault Displacement

beginning of the test and before failure of the specimen, the internal pressure varied between 78 psi (538 kPa) and 83 psi (572 kPa). Pressure loss occurred at a fault displacement of 16.2 in. (411 mm), corresponding to rupture of the test specimen at the north side of the south joint.

7.3.3. End Loads

The axial end loads were measured with two exterior and two interior load cells at both the north and south ends of the test basin. The sum of the two exterior load cells at each end of the test basin gives the total axial end load. Figure 7.6 shows the total loads at the north and south ends of the test basin vs. fault displacement. There is excellent agreement between them as expected, given the symmetry of this test.

An initial tensile end load of approximately 3 kips (13.3 kN) was present at the beginning of the test due to internal pressurization. This pressurization force was contained at the basin walls and did not impose loading to the buried section of the test specimen. At approximately 6 in. (152 mm) of fault displacement, there was full extension of the north and south joints after which the end loads increase rapidly. This load continued to increase at a constant rate until reaching 22.8 kips (101.4 kN) and 22.1 kips (98.3 kN) measured at the north and south ends of the pipeline, respectively.

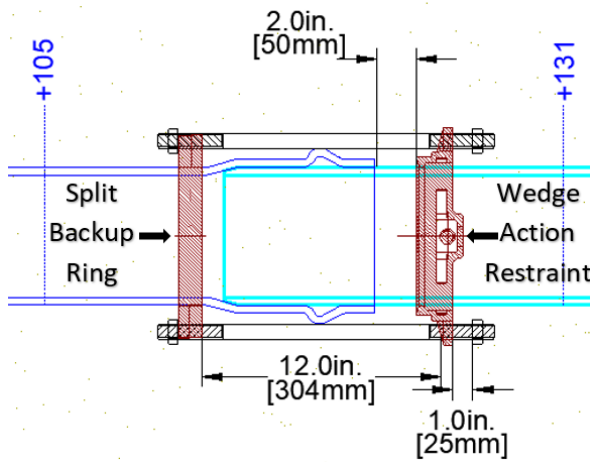


Figure 7.7. Plan View of Restrained Joint

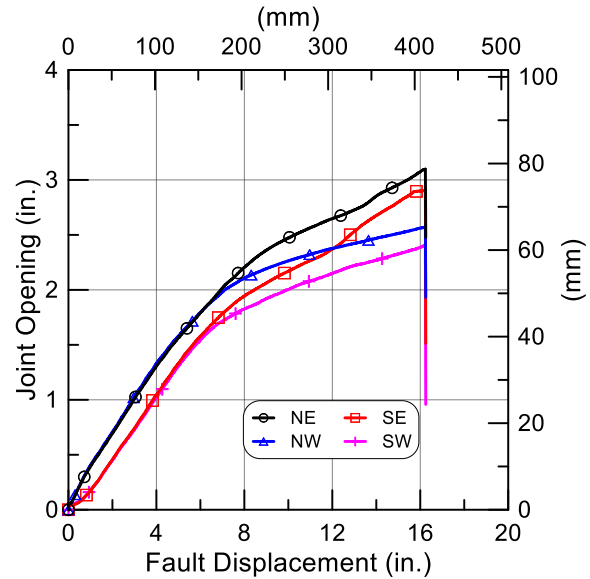


Figure 7.8. Joint Opening vs. Imposed Displacement

7.3.4. Joint Opening

A plan view of the northern restrained joint is shown in Figure 7.7. The image shows the spacing of the restraint mechanism. The spigot of the specimen was fully inserted into the bell of each joint during installation. The wedge-action restraint shown in Figure 1.1 was secured to the spigot at a distance of 2 in. (50 mm) from the face of the bell. The rods were inserted through both the split back-up ring and the wedge-action restraint to allow for 1 in. (25 mm) of space between the nuts and the wedge-action restraint. A plan view of the joint instrumentation and protective shield before burial is shown in Figure 7.2. Four string potentiometers were fixed from the bell to the spigot of the specimen to measure joint and axial displacement induced by fault rupture.

The joint opening measured at the east and west of each joint is shown in Figure 7.8. The north joint opened a maximum of 3.1 in. (78.7 mm) and 2.6 in. (66 mm) on its east and west side at springline, respectively. The south joint opened at springline a maximum of 2.9 in. (73.7 mm) and 2.4 in. (61 mm) on its east and west sides, respectively. The differences in measurement are likely due to the amount of soil that becomes wedged between the nuts and wedge-action restraint as previously explained for Figure 6.5. The southern joint ruptured at an average joint opening of 2.65 in. (67.3 mm), corresponding to an imposed fault displacement of 16.2 in. (411 mm).

7.3.5. Axial Strain and Force Distribution

All axial strains along the specimen's length were averaged and shown in Figure 7.9 at 3-in. (76.2-mm) increments of fault displacement. The strains along the pipeline directly before failure, at 16.2 in. (411.5 mm) of displacement, are also shown in the plot. As shown in Figure 7.1 the centerline of each restrained joint was located symmetrically at a distance of ± 118 in. (3 m.) either side of the fault.

The axial tensile strains increased with increased fault displacement along the entire specimen length. Figure 7.9 shows relatively low amounts of strain at zero displacement. This initial strain results from the Poisson's effect where the internal pressure causes contraction of the pipe in the longitudinal direction. The change in axial strain in the first 6 in. (152.4 mm) of fault displacement is relatively small and uniform. The strain increased at a higher rate per fault displacement after the first 6 in. (152.4 mm) of fault rupture when both joints had pulled tight to engage the restraints. The locations of the restrained joints are labeled in the figure. Drops in strain are apparent across each of the restrained joints, demonstrating the locally high axial force required to develop relative displacement between the restraint and surrounding soil.

The maximum tensile strains in the specimen were experienced at the SG \pm 25 gage planes on either side of the fault just before failure. The maximum strains were 1.01% at SG-25 and 1.02% at SG+25. Axial strains measured nearest the ends of the specimen were 0.61% at both planes SG-210 and SG+230.

At 12 in. (305 mm), 15 in. (381 mm) and 16.2 in. (412 mm) of displacement the axial tensile strain at the fault crossing decreases relative to those at the SG \pm 25 gage planes. This reduction appears to be related to ovaling of the pipe at the fault crossing.

The axial force distribution along the pipeline is shown in Figure 7.10. This force was calculated as $F = \epsilon AE$, where ϵ is the average axial strain at each gage plane location, A is the cross-sectional area of the specimen of 8.28 in.² (5342 mm²), and $E = 450.3$ ksi for the elastic range of the pipe response. To estimate axial loads outside the elastic range, Figure 2.4 was used to determine the secant modulus of the iPVC material at each level of tensile strain exceeding the proportional limit. This strain compatible secant modulus was used in the force equation above to estimate the axial load. There was a steady accumulation of axial load as fault movement increased. The maximum

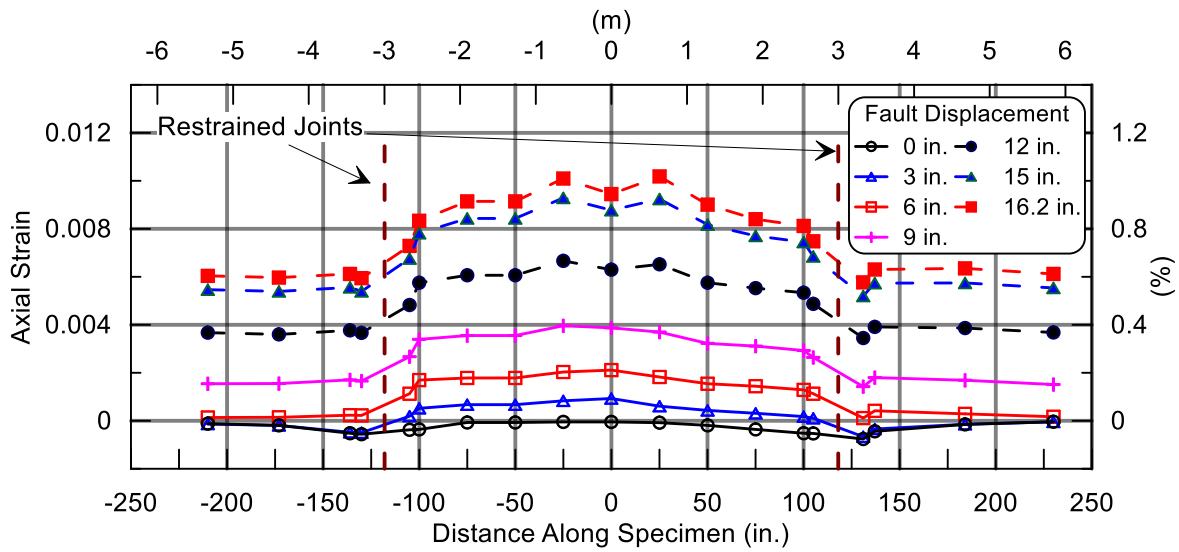


Figure 7.9. Distribution of Average Axial Strain Along the Specimen at Various Amounts of Fault Displacement

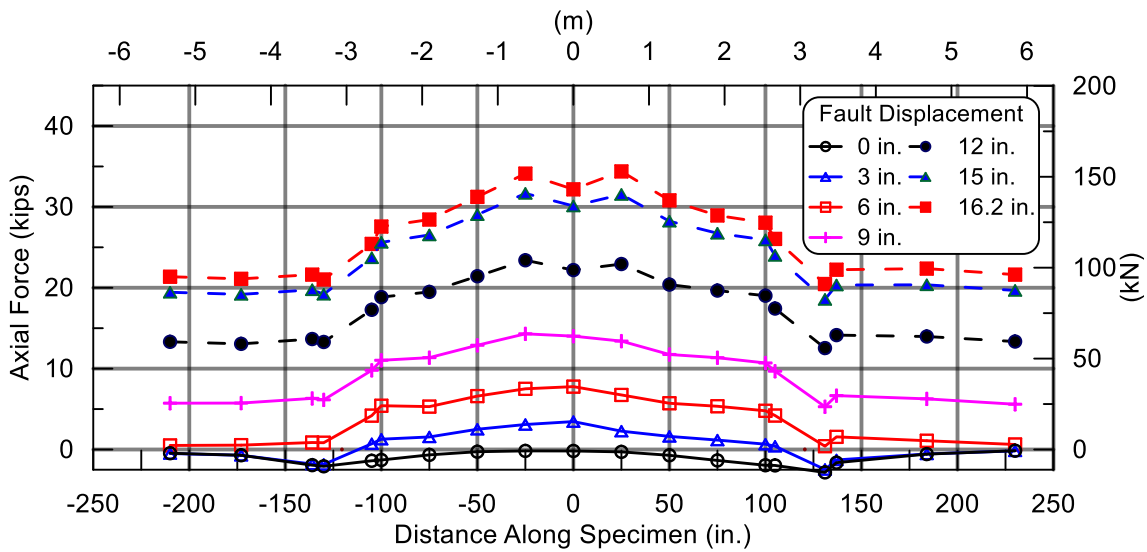


Figure 7.10. Distribution of Average Axial Force Along the Specimen at Various Amounts of Fault Displacement

axial force of 34.2 kips (152 kN) occurred at both the SG-25 and SG+25 gage planes. The axial force distribution follows a trend similar to the axial strain distribution along the pipeline. The average maximum axial load at the north and south joint was 27.1 kips (121 kN) and 26.7 kips (119 kN), respectively, which are consistent with the maximum axial force of 27 kips on average measured in the direct tension tests (see Figure 3.15).

7.3.6. Bending Strain and Moment Distribution

Figure 7.11 presents bending strains along the pipeline for various levels of fault displacement. The bending strain, ϵ_b , is calculated as:

$$\epsilon_b = \frac{\epsilon_W - \epsilon_E}{2} \quad (7.1)$$

Where ϵ_E is the measured strain at the gage mounted in the axial direction on the east springline and ϵ_W is the measured strain at the gage mounted in the axial direction on the west springline. When using this sign convention the direct axial strain on the east side is $\epsilon_{AE} = \epsilon_E + \epsilon_b$, and the direct axial strain on the west side is $\epsilon_{AW} = \epsilon_W - \epsilon_b$.

The bending strains measured along the north and south pipe were very low throughout the test. The bending strains show an antisymmetric response centered about the zero plane at the fault crossing. During the initial 9 in. (229 mm) of fault displacement, there were relatively large increases in the bending strains. Once the joints became fully extended, axial tension dominates the specimen response. The largest bending strains were measured at the SG-25 and SG+25 at 0.85% and 0.89%, respectively.

The experimental bending strain, ϵ_b , was converted to bending moment, M , through the expression:

$$M = \frac{2EI\epsilon_b}{D} \quad (7.2)$$

Where D is the outer diameter of the pipe specimen, I is the moment of inertia, ϵ_b is the bending strain as calculated in Equation 7.1, and $E = 450.3$ ksi for the elastic range of pipe response. To estimate axial loads outside the elastic range, Figure 2.4 was used to determine the secant modulus of the iPVC material at each level of strain exceeding the proportional limit, following an approach similar to that explained for axial load estimated under Section 7.2.5.

Figure 7.12 shows the calculated bending moment distribution along the specimen's length. The bending moment follows a very similar trend as the bending strain shown in Figure 7.11. For higher fault displacements, the imposed strains caused the pipe stresses to exceed the proportional limit, resulting in a lower nonlinear pipe stiffness.

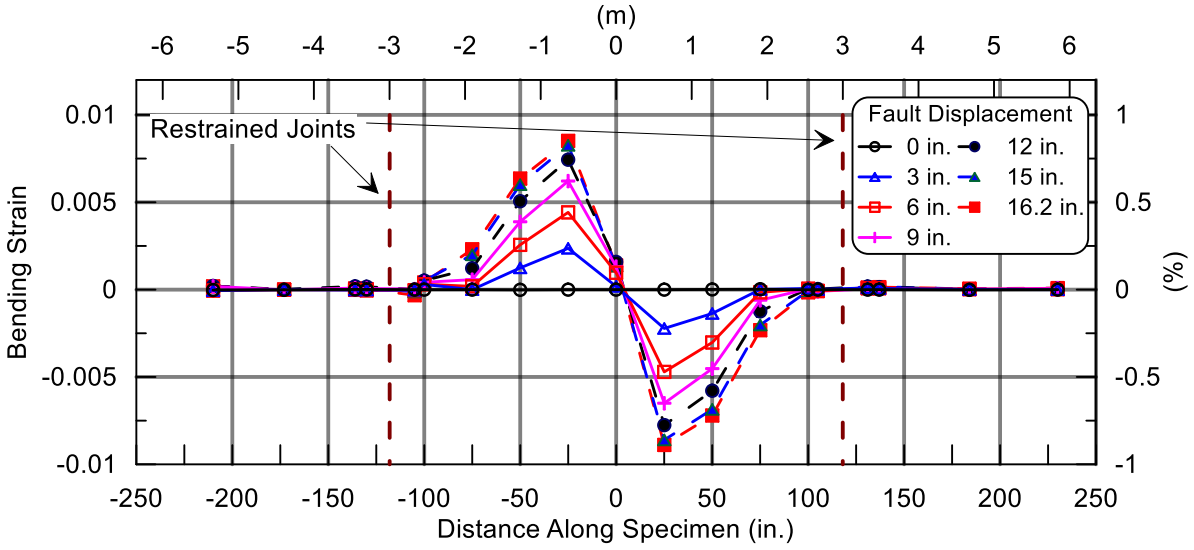


Figure 7.11. Distribution of Bending Strain Along the Specimen at Various Amounts of Fault Displacement

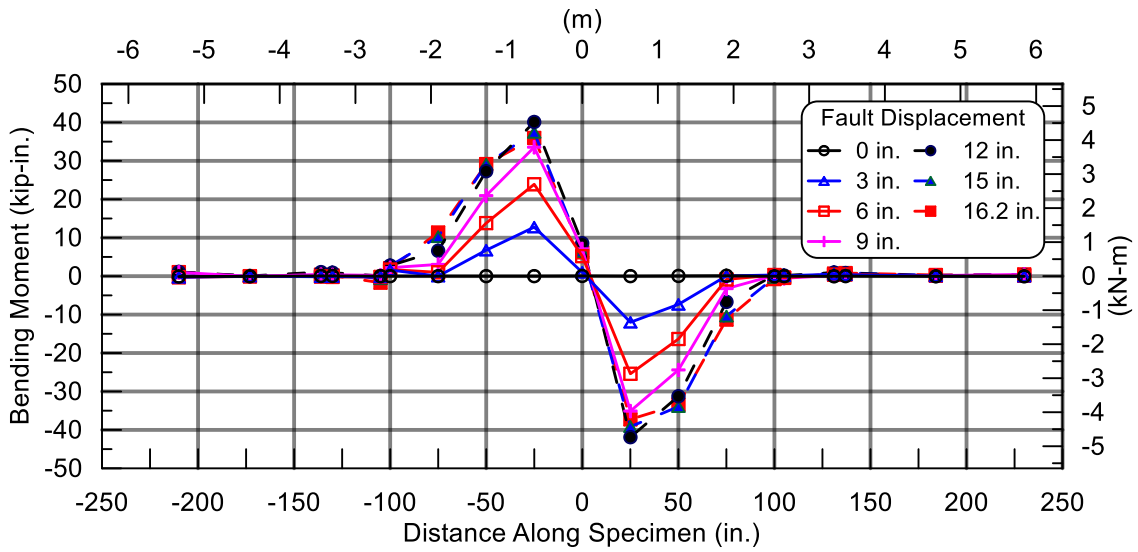


Figure 7.12. Distribution of Bending Moment Along the Specimen at Various Amounts of Fault Displacement

7.4. Post-Test Observations

At 16.2 in. (411.5 mm) of fault displacement, the pipe specimen ruptured just north of the south joint and internal pressure was lost. Figure 7.13 shows the opening of each joint in the fault rupture test as well as the joint opening measured in each tension test (TT1, TT2) versus force applied.

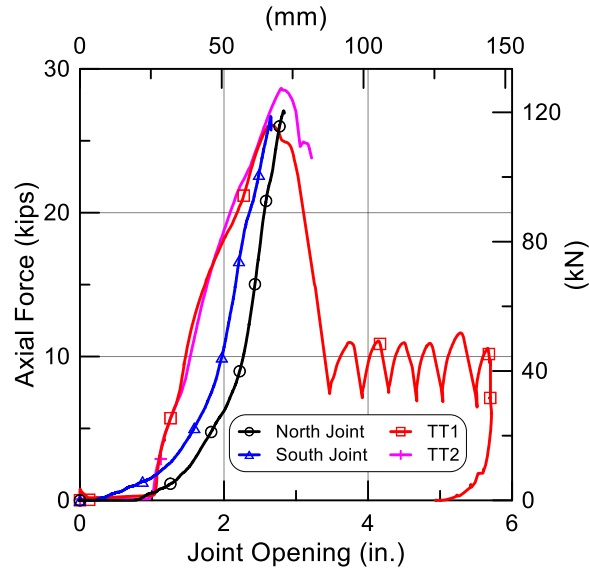


Figure 7.13. Joint Opening Comparison of Fault Rupture and Direct Tension Tests

As previously discussed, the north and south joint of the fault rupture test open an average of 2.83 in. (71.9 mm) and 2.65 in. (67.3 mm), respectively. This amount of joint opening compares well with the joint opening of both tension tests which opened a maximum of 2.65 in. (67.3 mm) and 2.79 in. (70.9 mm), respectively, at their maximum forces. The average maximum axial load at the north and south joint was 27.1 kips (121 kN) and 26.7 kips (119 kN), respectively, which are consistent with the maximum axial force of 27 (120 kN) kips on average measured in the direct tension tests.

Following the test, the entire pipeline was excavated to expose and examine the pipe. Figure 7.14 shows an overhead photo of the pipe and a close-up photo of the failed joint following excavation. North is to the left in both images. Figure 7.15 shows photos looking north of the specimen after excavation. Figure 7.15(b) provides a close-up view of the failed specimen and the circumferential fracture. It is likely that sand became wedged between the restraining nuts and collars of both joints during the fault rupture test. The amount of soil trapped was not possible to quantify and determine due to the rebound of the specimen at failure.

7.5. Summary of Split Basin Test

A 40.4 ft (12.3 m) long 6-in. (150-mm)-diameter iPVC pipeline with two restrained joints positioned 10 ft (3.1 m) on either side of a 50-degree fault rupture plane was tested at the Cornell Large-Scale Testing Facility. The pipeline was instrumented with 96 strain gages installed at 19 locations along the pipeline to measure axial and circumferential strains and to evaluate axial forces and bending moments. Strain gages were positioned at the crown (C), invert (I) east (E) springline, and west (W) springline of the pipe. Four string pots were used at each joint to measure pullout displacement and rotation. Four load cells were placed at each end of the specimen, reacting between the test basin structural frame and pipe end restraints to measure axial force. The pipe was pressurized to approximately 80 psi (552 kPa) throughout the test.

The pipeline was buried in the Cornell large-scale test basin in partially saturated sand that was compacted to have an average friction angle of 42 degrees, equivalent in strength to that of a medium dense to dense granular backfill. The 6.9-in. (175-mm) outer-diameter pipe was placed on a bed of soil with 13-in. (330-mm) thickness at the bottom of the test basin and soil was placed in lifts until the depth of burial to top of pipe was 32 in. (800 mm). During the test, the south part of the basin remained stationary, while the north part was displaced to the north and west by large stroke actuators to cause soil rupture and slip at the interface between the two parts of the test basin.

The north section of the test basin was displaced along a 50 degrees fault at a rate of 2 in. (50 mm) per minute. At 16.2 in. (411.5 mm) of total fault movement pressure loss occurred, corresponding to rupture of the test specimen at the north side of the south joint. This fault offset corresponds to 10.4 in. (264.5 mm) of axial tension of the basin and pipe.

The test measurements confirm that the pipeline was able to accommodate substantial fault movement through joint opening, development of axial strain along the pipe barrel, and bending of the pipe prior to leakage or rupture. The test also confirms pipeline performance when the joint restraint was initially set to allow 1 in. (25.4 mm) of axial slip before tight contact was established between the restraint and iPVC joint.



(a)



(b)

Figure 7.14. Overhead View of the (a) Pipeline and (b) Failed Joint After Excavation Following the Fault Rupture Test



(a)



(b)

Figure 7.15. View Looking North of (a) Failed Pipeline and (b) Close-Up of Ruptured Spigot

Section 8

Summary

This report presents the results from a test program to investigate the performance of nominal 6-in. (150-mm)-diameter iPVC pipe under significant levels of deformation, such as those associated with ground rupture.

8.1. Tension Test Summary

Two direct tension tests, TT1 and TT2, were performed in which the spigot was completely inserted into the bell for each test. Six 0.75-in. (19-mm) threaded rods were inserted through the restraints at either side of the joint. Nuts on the threaded rods were loosened before starting the test to allow approximately 1 in. (50 mm) of pullout before engagement. The pipe was pressurized with water to approximately 80 psi (550 kPa) during the tests.

The TT1 pipe attained a maximum tensile load of 26 kips (116 kN) at a joint opening of 2.65 in. (67 mm). Once this maximum load was achieved, further axial displacement was accompanied by six episodes of abrupt ratcheting movement when pullout of the spigot occurred at approximately 6 in. (150 mm). The TT2 pipe attained a maximum load of 28 kips (125 kN) at 2.79 in. (71 mm) of joint opening, after which the load dropped steeply to 25 kips (111 kN) followed immediately by brittle rupture of the spigot at the joint restraint.

In both tests there was an abrupt increase in load after 1 in. (25 mm) of axial movement when the nuts on the threaded rods made contact with the restraining collars. This contact was followed by 1.65 in. (42 mm) and 1.79 in. (45 mm) of additional movement to a peak load of 26 kips (116 kN) and 28 kips (125 kN), respectively. The sudden drop in load after peak capacity was accompanied either by ratcheting until pullout (TT1) or pipe failure (TT2).

8.2. Compression Test Summary

Three compression tests were performed on 126 in. (3.2 m) long sections of iPVC pipe with the bell and spigot specimens restrained by a Stargrip® Gen2 joint restraints. A 55-kip (245 kN) actuator with a 6 in. (152 mm) stroke was used to apply compressive loads at three different rates of 1, 10, and 100 in./min. (25, 254, and 2540 mm/min.), respectively. All three specimens were set with 1 in. (25 mm) of separation between the back of the bell and spigot as shown in Figure 4.2. In all three tests, the joint was able to accommodate significant deformation without experiencing

leakage at the joint. Average internal water pressure for CT1, CT2, and CT3 were 85 psi (586 kPa), 108 psi (744 kPa), and 110 psi (758 kPa), respectively. Even though the internal pressure increased to levels between 85 psi and 110 psi during the tests, the specimen did not leak or rupture at any time. In all three tests, the spigot was pushed past the back of the bell and split backup ring. In CT1 and CT2 the spigot penetrated the back of the bell and split backup ring simultaneously. In CT3 the spigot first penetrated the back of the bell as the split backup ring moved with the applied compressive displacement down the barrel of the bell. This movement of the split backup ring continued until engagement of the restraining mechanism. It is unlikely that this type of backup ring movement would occur if the restraint was confined by soil.

Through a change in rate of loading of over two orders of magnitude, the iPVC pipe with Stargrip® Gen2 joint restraints was able accommodate substantial compressive deformation with no failure or leakage under internal water pressure. For all three rates of loading, there is virtually no difference in the compressive load vs. axial displacement response. The compressive axial stiffness of the joint and restraint is essentially independent of loading rate for the three rates of loading investigated.

8.3. Four-point Bending Test Summary

An 18ft.-(5.5-m)-specimen of iPVC pipe with a restrained bell and spigot joint was tested in four-point bending. The specimen was centered in the loading frame. The pipe was pressurized for the duration of the test at approximately 80 psi (550 kPa). Support and loading points were located 30 in. (0.76 m) and 60 in. (1.52 m) away from the specimen's centerline, respectively. An initial 2.9 in. (74 mm) of vertical displacement was due to the self-weight of the pressurized pipe when supporting jacks under the specimen were manually removed. Loading was then applied through the downward movement of the loading frame's crosshead. Loading was continued until 22.2 in. (564 mm) of vertical displacement when servo-controlled loading was applied until the specimen reached a maximum deflection of 26.7 in. (678 mm). At this point, the geometric limit of the test frame was reached, the test was stopped, and the specimen was unloaded.

A maximum rotation of 52.2 degrees resulted in a max moment of 90.8 kip-in. (10.3 kN-m). The restrained joint of the specimen was able to withstand significant deformation, as shown by the photos and test measurements, without losing internal pressure at any time during the test.

8.4. Axial Pull Tests Summary

Axial pull tests were completed at three different soil depths to pipe crown of 30, 45, and 60 in. (760, 1140, and 1520 mm), respectively. One test was performed at each depth with the spigot and wedge action restraint on the north side of the specimen. One test was performed at the 45 in. (1140 mm) burial depth under a reversed orientation, where the split backup ring and bell were on the north side of the setup. Each pipe specimen was pulled approximately 30 in. (760 mm.) through the soil.

The axial force vs. displacement plots are presented and compared for all tests. These plots include the force measured by a load cell at the leading edge of movement outside the north side of the test basin, as well as the force measured at the strain gage plane nearest the north side of the joint restraint versus leading edge displacement. The plots that show the load measured at the strain plane nearest the north side of the joint restraint provide a good approximation of the load dropped across the joint during the test. The successively higher loads dropped at increasingly deeper burial depths are shown clearly in the plots. The axial force increases with relative displacement between the pipe and soil. It also increases linearly with soil depth.

In each axial pull test the joint was set to allow 1 in. (25.4 mm) of joint opening before engagement of the restraint. This setting allowed joint opening in soil that varied from about 0.60 in. (15.2 mm) for PT30, PT45 and PT60 to 0.25 in. (6.4 mm) for PT45b, leaving between 0.40 in. (10.2 mm) and 0.75 in. (19.1 mm) of axial slip that could not be realized. Opening less than 1 in. (25.4 mm) was related to sand that lodged between the restraining collar and locking nuts, thereby resisting full axial displacement of the rods through the restraining collar. Similar axial pull tests performed on 6-in. (150-mm) PVC pipe with restrained joints (Wham et al., 2017) resulted in approximately 0.35 in. (8.9 mm) to 0.50 in. (12.7 mm) of axial slip that could not be realized because of sand lodged between the restraining collar and locking nuts.

8.5. Summary of Large-Scale Fault Rupture Effects

A 40.4 ft (12.3 m) long 6-in. (150-mm)-diameter iPVC pipeline with two restrained joints positioned 10 ft (3.1 m) on either side of a 50-degree fault rupture plane was tested at the Cornell Large-Scale Testing Facility. The pipeline was instrumented with 96 strain gages installed at 19 locations along the pipeline to measure axial and circumferential strains and to evaluate axial

forces and bending moments. Strain gages were positioned at the crown (C), invert (I) east (E) springline, and west (W) springline of the pipe. Four string pots were used at each joint to measure pullout displacement and rotation. Four load cells were placed at each end of the specimen, reacting between the test basin structural frame and pipe end restraints to measure axial force. The pipe was pressurized to approximately 80 psi (552 kPa) throughout the test.

The pipeline was buried in the Cornell large-scale test basin in partially saturated sand that was compacted to have an average friction angle of 42 degrees, equivalent in strength to that of a medium dense to dense granular backfill. The 6.9-in. (175-mm) outer-diameter pipe was placed on a bed of soil with 13-in. (330-mm) thickness at the bottom of the test basin and soil was placed in lifts until the depth of burial to top of pipe was 32 in. (800 mm). During the test, the south part of the basin remained stationary, while the north part was displaced to the north and west by large stroke actuators to cause soil rupture and slip at the interface between the two parts of the test basin.

The north section of the test basin was displaced along a 50 degree fault at a rate of 2 in. (50 mm) per minute. At 16.2 in. (411.5 mm) of total fault movement pressure loss occurred, corresponding to rupture of the test specimen at the north side of the south joint. This fault offset corresponds to 10.4 in. (264.5 mm) of axial tension of the basin and pipe.

The test measurements confirm that the pipeline was able to accommodate substantial fault movement through joint opening, development of axial strain along the pipe barrel, and bending of the pipe prior to leakage or rupture. The test also confirms the performance of the joint when the joint restraint was initially set to allow 1 in. (25.4 mm) of axial slip before tight contact was established between the restraint and iPVC joint.

8.6. Significance of Test Results

Large-scale tests at Cornell demonstrate the ability of the iPVC pipe with restrained joints to accommodate significant fault movement through axial tension, bending, and compression of the joints and pipe barrel. Fault rupture simulated in the large-scale test is also representative of the most severe ground deformation that occurs along the margins of liquefaction-induced lateral spreads and landslides.

The amount of ground movement that can be accommodated with the iPVC restrained joint pipeline system will depend on several factors, including the depth of burial and the number and spacing of joints relative to the location of abrupt ground movement. The pipeline used in the large-scale split-basin test was able to accommodate 10.4 in. (264 mm) of axial extension, corresponding to a 1.9% elongation of the pipeline. Such capacity is large enough to accommodate the great majority (approximately 95%) of liquefaction-induced ground strains measured by high resolution LiDAR after each of four major earthquakes during the recent Canterbury Earthquake Sequence (CES) in Christchurch, NZ (Bouziou, et al., 2015; O'Rourke, et al., 2014). To put the CES ground strains in perspective, liquefaction-induced ground deformation measured in Christchurch exceed those documented in San Francisco during the 1989 Loma Prieta earthquake (e.g., O'Rourke and Pease, 1997; Pease and O'Rourke, 1997) and in the San Fernando Valley during the 1994 Northridge earthquake (e.g., O'Rourke, 1998). They are comparable to the levels of most severe liquefaction-induced ground deformation documented for the 1906 San Francisco earthquake, which caused extensive damage to the San Francisco water distribution system (e.g., O'Rourke and Pease, 1997; O'Rourke, et al., 2006).

References

- ASTM International (2014). "Standard Test Method for Tensile Properties of Plastics", *ASTM Standards*. D638-14, pp. 1-17.
- AWWA (2007). "Polyvinyl Chloride (PVC) Pressure Pipe and Fabricated Fittings, 4 in. through 12 in. (100 mm through 300 mm), for Water Transmission and Distribution", *AWWA Standard*, ANSI/AWWA C900-07, pp. 1 - 44.
- Bouziou, D., T. D. O'Rourke, M. Cubrinovski, and D. Henderson (2015) "Evaluation of Ground Deformations during the 2010-2011 Canterbury Earthquake Sequence", *Proceedings*, 6th Intl. Conf. on Earthquake Geotech. Engr., Christchurch, NZ, 8p.
- Hughes, D., Venkatesh, Lee A. H-J, Paradkar, A.B., Najafi, M. (2016) "Development, Evaluation, and Installation of New Improved PVC (iPVC) Pipe for Water Applications" *Proceedings*, 2016 ASCE Pipelines Conference, Kansas City, MO, ASCE, Reston, VA, July, pp. 1046-1060.
- Star Pipe Products (2018). "Joint Restraint Products, Mechanical Joint Wedge Action Restraint for AWWA C900/C909 and IPS PVC Pipe Patent Pending," Star Pipe Products, Houston, TX, <http://www.starpipeproducts.com/pdf/joint%20resraint/catalog/Series4000G2.pdf>, Last accessed September 16, 2018.
- O'Rourke, T. D. (1998) "An Overview of Geotechnical and Lifeline Earthquake Engineering", *Geotechnical Special Publication No. 75*, ASCE, Reston, VA, Proceedings of Geotechnical Earthquake Engineering and Soil Dynamics Conference, Seattle, WA, Aug. 1998, Vol. 2, pp.1392-1426.
- O'Rourke, T. D. and J. W. Pease (1997) "Mapping Liquefiable Layer Thickness for Seismic Hazard Assessment", *Journal of Geotechnical Engineering*, ASCE, New York, NY, Vol. 123, No.1, January, pp. 46-56.
- O'Rourke, T. D., A. Bonneau, J. Pease, P. Shi, and Y. Wang (2006) "Liquefaction Ground Failures in San Francisco", *Earthquake Spectra*, EERI, Oakland, CA, Special 1906 San Francisco Earthquake, Vol. 22, No. 52, Apr., pp. 691-6112.
- O'Rourke, T. D., Jeon, S-S., Toprak, S., Cubrinovski, M., Hughes, M., van Ballegooy, S., and Bouziou, D. (2014) "Earthquake Response of Underground Pipeline Networks in Christchurch, NZ", *Earthquake Spectra*, EERI, Vol. 30, No.1, pp. 183-204.
- Pease, J. W. and T. D. O'Rourke (1997) "Seismic Response of Liquefaction Sites", *Journal of Geotechnical Engineering*, ASCE, New York, NY, Vol. 123, No. 1, January, pp. 37-45.
- Wham, B.P., Berger, B., O'Rourke, T.D., Payiya-Ekkasut, C, Stewart, H.E. (2017) *Performance Evaluation of Bionax SR PVCO Pipeline with Extended Bell Joints under Earthquake-Induced Ground Deformation*. Geotechnical Lifelines Large-Scale Testing Facility. <https://lifelines.cee.cornell.edu/projects/> Last accessed September 18, 2018.